



University
of Glasgow

Johnstone, John Russell (2010) *The photon beam asymmetry for KY production from the bound proton in deuterium*. PhD thesis.

<http://theses.gla.ac.uk/1616/>

Copyright and moral rights for this thesis are retained by the author

A copy can be downloaded for personal non-commercial research or study, without prior permission or charge

This thesis cannot be reproduced or quoted extensively from without first obtaining permission in writing from the Author

The content must not be changed in any way or sold commercially in any format or medium without the formal permission of the Author

When referring to this work, full bibliographic details including the author, title, awarding institution and date of the thesis must be given

The Photon Beam Asymmetry for KY
Production from the Bound Proton in Deuterium

J Russell Johnstone

Presented as a Thesis for the Degree of Doctor of Philosophy

Nuclear Physics Group
Department of Physics and Astronomy
University of Glasgow

© J. R. Johnstone 2009

Abstract

This thesis presents measurements of the photon asymmetry polarisation observable for the $\gamma d \rightarrow K^+\Lambda$ and $\gamma d \rightarrow K^+\Sigma^0$ reactions from the bound proton in deuterium. The data were collected in the summer of 2007 at the Thomas Jefferson National Accelerator Facility in Newport-News, Virginia, using a linearly polarised photon beam in the energy range 1.3 to 2.3 GeV.

The aim of the experiment was to investigate the validity of the quasifree approximation of a bound nucleon in deuterium. This analysis focusses on the proton and by directly comparing results from this analysis to those from previous similar analyses on the free proton, this issue is addressed. Ultimately, this will allow reliable results to be extracted from analyses of channels on the bound neutron in deuterium.

The photon asymmetry is found to be positive for the entire kinematic range for both channels with indications of some structure above centre-of-mass energies of 1.8 GeV. The $K^+\Lambda$ results are compared to measurements from the free proton produced with similar kinematics. Also included in the comparison are model predictions from the Kaon-MAID isobaric model which includes the established $^{****}S_{11}(1650)$, $^{***}P_{11}(1710)$ and $^{****}P_{13}(1720)$ resonances and uses various Born terms to describe the background. Comparison to the free proton results gave good agreement with the majority of the quasifree measurements being comparable to those from the free proton. There was however seen to be some indication of a systematic overestimation of the results in one kinematic region. The model gives reasonable agreement with the data, with some evidence for a role to be played by the missing $D_{13}(1900)$ resonance. For the $K^+\Sigma^0$ results, the same comparison was made with free proton results and the Kaon-MAID model, this time with the inclusion of the $^{**}S_{31}(1900)$ and $^{****}P_{31}(1910)$ resonances. No missing states were considered in this calculation and the agreement with the results was not as good as that of the $K^+\Lambda$ channel. Comparison to measurements from the free proton produced similarly good results as were found with the $K^+\Lambda$ results but this time with no obvious indication of any systematic discrepancy.

Overall, the agreement between the quasifree and the free predictions was found to be quite good and will lend weight to future analyses from the bound neutron in deuterium by allowing a quasifree approximation to be assumed *prima facie*.

Declaration

The data presented in this thesis were obtained as part of the g13 collaboration at the Thomas Jefferson National Accelerator Facility, Virginia, USA, and the Nuclear Physics Experiment Group, The University of Glasgow. I participated fully in the preparation and execution of the experiment. The analysis of the experimental data is my own work. This thesis was composed by myself.

J. Russell Johnstone

November 2009

Acknowledgements

This analysis, and ultimately, thesis would not have been possible without the assistance and support from a vast number of people. Unfortunately, this one brief section is too short to do them all justice so I will begin by giving a special thankyou to anyone whose name I have not mentioned. Those who should be singled out by name include Prof. Guenther Rosner as head of the University of Glasgow's NPE research group for giving me the opportunity to begin my post-graduate research career and to carry it on to PhD level. Next are my two supervisors, Dr. David Ireland and Dr. Ken Livingston for their continued advice and suggestions at all stages of my PhD work. Especially so for the time taken to critically pore over every iteration of the resulting thesis, though sometimes I felt my pictures would never be big enough. At least it got there in the end.

Jefferson Lab included its own unique team of individuals who contributed in their own way to the body of work presented here. These people include Joe Santoro, Pawel Nadel-Turonski, Eugene Pasyuk and the engineering team at the EEL building. Without those individuals from the EEL building, I wouldn't be the expert in coil winding that I am today. Joe should be singled out here for his companionship to people from the Glasgow group. Your friendship helped make my time at JLab much more bearable and enjoyable experience, it's only a shame your presence is no longer available to induct future generations of Glasgow students to the special Newport-News way of life. I hope things are going well for yourself and Julie in NYC.

When not enjoying the delights of the Nawab and Plaza Azteca(-deceased) in Newport-News, my time in Glasgow was spent enjoying the company of fellow physicists. Most notably amongst these were the fellow 'official' office dwellers, both past and present: Bryan McKinnon; Craig Paterson; Neil Hassall; Parada Hutaurok; Stuart Fegan and Joe Mancell. The 'unofficial' office of the NPE group changes with the seasons; in cold weather it is the Three Judges and during warmer times it is Cottiers. Those to share the 'unofficial' office were David Hamilton, Neil Thompson, Andrew Osborne, Richard Codling, Jamie Robinson, David Mahon, David Howdle, Euan Cowie, Gary Smith, Gordon Hill, Eilidh McNicoll, Jonathan Burns, Seian Al Jebali, Jennifer Bowles and Rachel Montgomery. A big thankyou to everyone for keeping me away from anything physics related. Special thanks should be extended to Bryan McKinnon and David Hamilton for help with all aspects of the analysis, thesis and subsequent job hunt.

Finally, a thankyou to all my friends and family for maintaining a nearly

physics-related-discussion free environment to enjoy and for feigning interest whenever the subject of my work came up.

“[...eritis sicut dii scientes bonum et malum...]”

Genesis 3:5, *Latin Vulgate Bible*.

“A little learning is a dangerous thing;

Drink deep, or taste not the Pierian spring:

There shallow draughts intoxicate the brain,

And drinking largely sobers us again.”

Alexander Pope, *Essay on Criticism* (1711).

Contents

| | | |
|----------|---|-----------|
| 1 | Introduction | 1 |
| 1.0.1 | Symmetric Quark Models | 2 |
| 1.0.2 | Missing Resonances | 4 |
| 1.1 | The Λ and Σ^0 Hyperons | 6 |
| 1.2 | Summary | 9 |
| 2 | Background | 11 |
| 2.1 | Baryon Spectroscopy | 12 |
| 2.2 | Polarisation Observables in Hyperon Photoproduction | 13 |
| 2.2.1 | Formalism | 13 |
| 2.2.2 | Extraction of Observables | 15 |
| 2.3 | Theoretical Models | 16 |
| 2.3.1 | Isobar Models | 16 |
| 2.3.2 | Coupled-Channel Analyses | 18 |
| 2.3.3 | Regge Models | 20 |
| 2.4 | Previous Measurements | 23 |
| 2.4.1 | Photon Asymmetries on the free proton | 23 |
| 2.4.2 | Quasifree Proton | 26 |
| 2.4.3 | Quasifree neutron | 28 |
| 2.4.4 | Quasifree kaon photoproduction on nuclei | 30 |
| 2.5 | Summary | 36 |
| 3 | Experimental Setup | 40 |
| 3.1 | JLab, Hall-B | 40 |
| 3.2 | Coherent Bremsstrahlung Facility | 42 |
| 3.3 | G13 target | 50 |
| 3.4 | The CEBAF Large Acceptance Spectrometer (CLAS) | 50 |
| 3.4.1 | Superconducting Torus Magnet | 52 |
| 3.4.2 | Start Counter | 53 |

| | | |
|----------|--|-----------|
| 3.4.3 | Drift Chambers | 54 |
| 3.4.4 | Time of Flight Scintillation Counters | 56 |
| 3.4.5 | Electromagnetic Calorimeter | 58 |
| 3.4.6 | Beam Position Monitors | 59 |
| 3.5 | Trigger and Data Acquisition System | 59 |
| 3.5.1 | Data Acquisition | 60 |
| 4 | Data Processing and Calibrations | 63 |
| 4.1 | Run Conditions and Data | 63 |
| 4.2 | CLAS Data Output | 64 |
| 4.3 | Data Reconstruction / <i>Cooking</i> | 65 |
| 4.3.1 | Quality Monitoring | 65 |
| 4.4 | Subsystem Calibrations | 67 |
| 4.4.1 | Start Counter Calibration | 67 |
| 4.4.2 | Photon Tagger Calibration / Beam RF | 68 |
| 4.4.3 | Time of Flight Calibration | 76 |
| 4.4.4 | Drift Chamber Calibration | 78 |
| 4.4.5 | Electromagnetic Calorimeter Calibration | 79 |
| 4.5 | Photon Polarisation | 79 |
| 4.6 | Summary | 82 |
| 5 | Data Analysis | 83 |
| 5.1 | Particle Identification and Event Selection | 83 |
| 5.1.1 | TOF Mass Cuts | 83 |
| 5.1.2 | Photon Selection | 85 |
| 5.1.3 | Mis-identification of mesons | 86 |
| 5.1.4 | Hadron - Photon Vertex Timing Cuts | 87 |
| 5.1.5 | Hadron - Hadron Vertex Timing Cuts | 88 |
| 5.1.6 | Invariant Mass Cut | 92 |
| 5.1.7 | Energy Loss / ELOSS | 92 |
| 5.1.8 | Fiducial Cuts | 93 |
| 5.2 | Analysis of $\gamma d \rightarrow K^+ p \pi^- (n)$ | 95 |
| 5.2.1 | Λ and Σ Separation | 95 |
| 5.2.2 | Momentum Cut | 98 |
| 5.2.3 | Hyperon Yield Extraction | 99 |
| 5.3 | Beam Asymmetry | 102 |
| 5.3.1 | Bin Selection | 102 |
| 5.3.2 | Extraction of Σ | 105 |

| | | |
|----------|--|------------|
| 5.4 | Summary | 106 |
| 6 | Results and Discussion | 110 |
| 6.1 | Comparison with free proton | 110 |
| 6.1.1 | Photon asymmetry results for $K^+\Lambda$ | 115 |
| 6.1.2 | Photon asymmetry results for $K^+\Sigma^0$ | 116 |
| 6.2 | Predictions for the neutron channel | 117 |
| 6.3 | Conclusions | 117 |

List of Figures

| | | |
|------|---|----|
| 1.1 | Photoproduction cross-section on the proton. | 3 |
| 1.2 | Quark model representations. | 6 |
| 1.3 | Mass predictions from a relativised quark model. | 8 |
| 2.1 | $\gamma d \longrightarrow K^+\Lambda(n)$ rescattering graphs. | 13 |
| 2.2 | Nucleon momentum distribution in deuterium. | 14 |
| 2.3 | Feynman diagrams for $\gamma p \longrightarrow KY$ reactions. | 18 |
| 2.4 | SAPHIR $K^+\Lambda$ total cross section from the proton. | 19 |
| 2.5 | Mart and Bennhold photon asymmetry calculations. | 20 |
| 2.6 | Julia-Diaz $K^+\Lambda$ model calculations compared to data. | 21 |
| 2.7 | The different energy scales used in the RPR approach. | 23 |
| 2.8 | RPR Λ beam asymmetry calculations compared to LEPS data. . . | 24 |
| 2.9 | $K^+\Lambda$ free proton beam asymmetries from CLAS and GRAAL. . . | 26 |
| 2.10 | $K^+\Lambda$ free proton beam asymmetries from CLAS and LEPS. . . . | 27 |
| 2.11 | $K^+\Sigma^0$ free proton beam asymmetries from CLAS and GRAAL. . . | 28 |
| 2.12 | $K^+\Sigma^0$ free proton beam asymmetries from CLAS and LEPS. . . . | 29 |
| 2.13 | GRAAL 2005 η beam asymmetry measurements. | 30 |
| 2.14 | GRAAL η from free and quasi-free proton beam asymmetry comparison. | 31 |
| 2.15 | LEPS quasifree neutron beam asymmetries. | 32 |
| 2.16 | Quasifree kaon photoproduction on nuclei model beam asymmetry calculations for KY | 33 |
| 2.17 | Effects of final-state interactions under quasifree kinematics. . . . | 38 |
| 2.18 | Effects of final-state interactions under open kinematics. | 39 |
| 3.1 | CEBAF overview, with components. | 41 |
| 3.2 | Hall-B layout. | 42 |
| 3.3 | Incoherent Bremsstrahlung spectrum. | 44 |
| 3.4 | Hall-B beamline layout. | 45 |
| 3.5 | The Hall-B diamond goniometer. | 45 |

| | | |
|------|--|-----|
| 3.6 | Schematic representation of the goniometer's degrees of freedom. | 46 |
| 3.7 | Tagger magnet with T and E-counters. | 47 |
| 3.8 | Tagger hodoscope section. | 49 |
| 3.9 | The active collimator. | 50 |
| 3.10 | G13 target cell. | 50 |
| 3.11 | The CLAS detector in Hall B. | 51 |
| 3.12 | CLAS cross-section. | 52 |
| 3.13 | CLAS torus coils. | 53 |
| 3.14 | CLAS start counter. | 54 |
| 3.15 | CLAS drift chambers. | 56 |
| 3.16 | CLAS time of flight paddle. | 57 |
| 3.17 | CLAS electromagnetic calorimeter section. | 59 |
| 3.18 | Reconstructed hadronic event in CED. | 61 |
| 4.1 | CSQL monitoring plot of number of kaons per event. | 66 |
| 4.2 | Start counter calibration plots. | 69 |
| 4.3 | Tagger hodoscope. | 70 |
| 4.4 | Tagger calibration plots. | 71 |
| 4.5 | Enhancement plot. | 80 |
| 4.7 | Variation of the coherent edge position. | 81 |
| 4.6 | Tagger spectra compared with ANB calculation for one coherent peak setting. | 81 |
| 5.1 | Time-of-flight mass plot. | 84 |
| 5.2 | Missing mass squared cuts for mis-identified particles. | 87 |
| 5.3 | Proton-photon vertex timing cuts. | 89 |
| 5.4 | Kaon-photon vertex timing cuts. | 90 |
| 5.5 | Hadron-hadron vertex timing cuts. | 91 |
| 5.6 | Invariant mass cut. | 92 |
| 5.7 | Energy loss plots. | 94 |
| 5.8 | Fiducial cut plots. | 95 |
| 5.9 | Hyperon separation plots. | 97 |
| 5.10 | Hyperon separation plots. | 98 |
| 5.11 | Spectator missing momentum plots. | 99 |
| 5.12 | Hyperon fitting routine output. | 101 |
| 5.13 | Bin selection. | 103 |
| 5.14 | Asymmetry construction. | 104 |
| 5.15 | $\cos 2\phi$ fit of the asymmetry for $E_\gamma = 1.9$ GeV for the $K^+\Lambda$ channel. | 107 |

| | | |
|------|---|-----|
| 5.16 | $\cos 2\phi$ fit of the asymmetry for $E_\gamma = 1.9$ GeV for the $K^+\Sigma^0$ channel. | 108 |
| 5.17 | Photon asymmetries for $E_\gamma = 1.9$ GeV as a function of $\cos\theta_{cm}^{K^+}$ for the $K^+\Lambda$ channel. | 109 |
| 5.18 | Photon asymmetries for $E_\gamma = 1.9$ GeV as a function of $\cos\theta_{cm}^{K^+}$ for the $K^+\Sigma^0$ channel. | 109 |
| 6.1 | $K\Lambda$ free and quasifree beam asymmetries vs. $\cos\theta$ compared to Kaon-MAID. | 111 |
| 6.2 | $K\Lambda$ free and quasifree beam asymmetries vs. E_γ compared to Kaon-MAID. | 112 |
| 6.3 | $K\Sigma^0$ free and quasifree beam asymmetries vs. $\cos\theta$ compared to Kaon-MAID. | 113 |
| 6.4 | $K\Sigma^0$ free and quasifree beam asymmetries vs. E_γ compared to Kaon-MAID. | 114 |
| 6.5 | Beam asymmetry predictions from the free neutron. | 118 |

List of Tables

| | | |
|-----|---|-----|
| 1.2 | PDG star ratings for measured and missing baryon resonances [1]. | 7 |
| 1.3 | Main properties of the Λ and Σ^0 hyperons from the PDG [1]. | 9 |
| 2.1 | Polarisation observables and transversity representations. | 15 |
| 4.1 | G13 running conditions. | 63 |
| 4.2 | G13 beam settings and triggers. | 64 |
| 5.1 | Analysis cuts. | 101 |
| 6.1 | Beam asymmetry difference, $\Delta\Sigma$, for quasifree and free proton, $K\Lambda$ channel. | 112 |
| 6.2 | Beam asymmetry difference, $\Delta\Sigma$, for quasifree and free proton, $K\Sigma$ channel. | 113 |

Chapter 1

Introduction

The purpose of the analysis described here was to perform a beam asymmetry measurement for $\gamma d \rightarrow K^+\Lambda$ and $\gamma d \rightarrow K^+\Sigma^0$ on the proton bound in a deuterium nucleus. By then comparing the results to similar measurements on the free proton, a conclusion can be reached as to whether measurements made on the bound neutron can be assumed to be comparable to the free case. With this comparison, it is possible to test the quasifree approximation of a bound nucleon in deuterium. This analysis was undertaken as part of a broader program of experiments and associated analyses investigating the nucleon excitation spectrum.

The photoabsorption spectrum of the nucleon consists of many resonances which are broad and overlapping. This is clearly seen in figure 1.1, which shows the total photoproduction cross-section on the proton in $E_\gamma = 0.2 \sim 2.0\text{GeV}$. Also shown are the cross-sections for the most significant contributing reaction channels. Several resonances are clearly visible (e.g. $\Delta(1232)$), and quark models such as those of Capstick and Roberts, Faiman and Hendry, and Forsyth and Cutkosky [2–4] have been very successful in predicting their energies and quantum numbers. Such models, however, also predict several resonances which have not yet been observed; the so-called *missing resonances*. The goal of the N^* program at Jefferson Lab is to make a systematic search for *missing resonances*, and to determine whether they are unobserved due to experimental considerations, or erroneously predicted by theoreticians.

The recent availability of highly polarised beams and targets at Jefferson Laboratory, combined with the $\sim 4\pi$ CLAS (CEBAF Large Acceptance Spectrometer) detector offers the opportunity to search for missing resonances by measuring polarisation observables for reactions which have low cross-sections and result in multi-particle final states. In particular, for strange channels, there is the pos-

sibility to measure the polarisation of the recoiling hyperon and hence a range of single and double polarisation observables. With the combination of polarised beam and target, and recoil polarisation the ultimate aim of experiments is to make the first *complete measurement* in pseudo-scalar meson photoproduction, leading to a model independent extraction of the production amplitudes. This should offer a unique opportunity for theorists to determine the contribution of nucleon resonances in KY photonproduction.

Several single and double polarisation observables have already been measured with CLAS for $K\Lambda$ and $K\Sigma^0$ reactions on the proton with circularly and linearly polarised beams [5–7]. The first data using a longitudinally polarised, frozen-spin target was taken in 2007/08, and the second phase, with the target transversely polarised is scheduled for March 2010. These will produce the first complete measurement for $K\Lambda$ and $K\Sigma^0$ on the proton. The next challenge is to measure similar reactions on the neutron. This was the aim of the g13 experiment¹, where liquid deuterium was used as the best available approximation to a free neutron target. It is essential in this experiment to determine if the quasi-free approximation is valid, and the method employed here is to measure the photon asymmetry, Σ , for the $K\Lambda$ and $K\Sigma^0$ production on the bound proton from the deuteron and compare with the free proton results measured from the g8 data [7]. These measurements are presented in this thesis.

1.0.1 Symmetric Quark Models

In QCD symmetric quark models offer the possibility to classify hadrons in terms of their valence quarks. The quantum numbers associated with these quarks identify the hadrons in terms of quark flavour, J^{PC} , with J being the angular momentum, P the intrinsic parity and C the charge conjugation. By introducing the concept of strangeness, Gell-Mann [8] and others allowed the baryon spectrum to be unfolded in the symmetry of the $SU(3)$ quark model. Once quark spin and orbital angular momentum excitations were introduced, a rich spectrum of nucleon resonances based on $SU(6) \otimes O(3)$ symmetric quark models were then allowed.

Faiman and Hendry [3] carried out the first attempts at unfolding the baryon spectrum from a quark model by developing a quark shell model based on harmonic-oscillator forces. The model evolved from the basic concepts of a particle moving

¹Experiment nomenclature at JLab assigns experiments involving real photons the letter “g” and the number represents the order in which the experiment was *approved*, but **not** in which it actually ran. Therefore, g13 was the 13th approved real photon experiment at JLab.

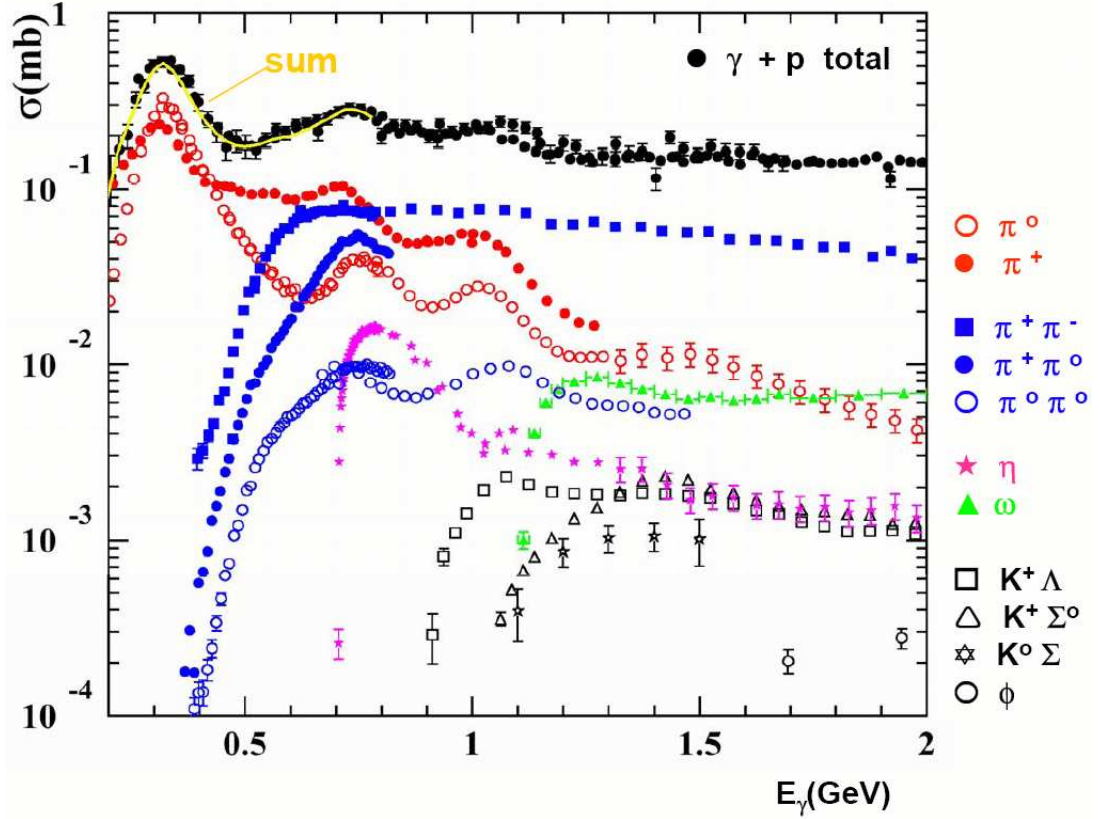


Figure 1.1: Photoproduction cross-section on the proton for the energy range $E_\gamma = 0.2 \sim 2.0 \text{ GeV}$. The total cross-section exhibits four resonance regions. The lowest region is associated with the $\Delta(1232)$ excitation. Both $K^+\Lambda$ and $K^+\Sigma^0$ channel cross-sections are shown also, highlighting the fact that they are almost two orders of magnitude lower than that of single pion production.

within a three dimensional harmonic-oscillator potential. It was then possible, with this model, to predict a baryon spectrum that agreed with the known contemporary data. Forsyth and Cutkosky [4] then developed a QCD improved quark shell model to fit the masses and elastic widths of the $S = 0$ baryons. This model was based on a decay operator with the form $S \cdot (g_1 P_q + g_2 P_{-q})$, with P_q and P_{-q} being the quark and antiquark momenta respectively and S is their combined spin. This model also included various baryon resonances, many of which were found to be in agreement with the data of the time. More work by Koniuk and Isgur [9] created a model based on elementary-meson emission and it allowed for predictions of non-strange baryon decays up to the $N = 2$ band in both $K^+\Lambda$ and $K^+\Sigma^0$ photoproduction. For a reaction in this model, a meson is treated as a pointlike particle which couples directly to the quarks in the initial baryon. Models like these, and variants of them, are capable of predicting a large spectrum of non-strange baryon states that should couple strongly to strange decay channels. By comparing what states are then found experimentally and how well their extracted properties, such as widths, agree with model calculations, will be a test of how accurately the models describe the data.

1.0.2 Missing Resonances

The main conflict for the field of baryon spectroscopy is that $SU(6) \otimes O(3)$ symmetric quark models predict far more resonances than have been observed in experiment. Table 1.2 shows the PDG [1] star rating for measured and missing baryon resonances using the QCD improved model of Cutkosky [4], the more stars associated with a resonance the greater the certainty of its existence. Only those resonances considered to be established (overall three or four stars) appear in the PDG's overall Baryon Summary Table, and a resonance is only considered to be established if it has been seen in at least two independent analyses of elastic scattering. A large number of the predicted states in table 1.2 have either one or zero star ratings implying little or no experimental evidence of their existence. There are currently two competing hypotheses as to why these resonances have not yet been determined experimentally. The first possibility is that the quark models to date have some inherent flaw and require some update or modification. Diquark models [10] are founded on the assumption that two of the quarks are bound in a tightly coupled state within the nucleon. This situation is thought to happen if the colours and spins of the two quarks are anti-symmetric, resulting in an attractive force between the pair. If two quarks combine in this fashion, it results in a low energy configuration that decreases the number of internal degrees

of freedom of the nucleon. This produces a lower level density of possible baryon resonances and a large number of the missing states can therefore be removed from the model predictions. The concept of the diquark model is illustrated in figure 1.2.

The second possibility arises because the contemporary measurements may not have been particularly sensitive to the missing states. This is because the majority of the existing data comes from pion production experiments involving πN final states. Recent quark model calculations by Capstick and Roberts [2] predict that some of these missing resonances may couple strongly to strange baryon final states from photoproduction experiments. Their model describes the baryon decays in a relativised scheme. The calculation accounts for the finite size of the final meson as well as including the excited strange baryons $\Lambda(1405)$, $\Lambda(1520)$ and $\Sigma(1385)$ and K^* excited meson states. The model predicts a series of negative and positive parity states up to the $N = 3$ band. The model predictions for the $K^+\Lambda$ and the $K^+\Sigma^0$ channels are shown in figure 1.3. The signs and magnitudes for the predicted amplitudes for both channels were found to agree well with experimentally established states. Capstick and Roberts predicted that for the $K^+\Lambda$ channel there should be several negative parity states in the $N = 3$ band and that they should be evident in experiment. Specifically, they predict that the two star $N(2080)D_{13}$ state should be clearly seen with a precise measurement of $\gamma P \rightarrow K^+\Lambda$. They also predict the existence of the poorly established $N(2090)S_{11}$. Regarding the $K^+\Sigma^0$ reaction, Capstick and Roberts' calculations suggest a large contribution comes from the $\Delta(1910)P_{31}$, for which the PDG only currently gives an upper limit [1]. Despite the amplitudes for the $K^+\Sigma^0$ channel being much less certain than those for the $K^+\Lambda$ the existence of some $N = 2$ missing states can also be predicted.

By using a linearly polarised photon beam one can access the single polarisation observables of the photon asymmetry, Σ , the hyperon recoil polarisation, P , the target asymmetry, T and the double polarisation observables O_x and O_z . Similarly, by using a circularly polarised photon beam we have access to the double, circular polarisation observables C_x and C_z . Measurements such as these are expected to be extremely sensitive to the predicted $D_{13}(1960)$ missing resonance [11], and when combined with previous measurements should provide a comprehensive analysis. Future analyses also intend to make use of a polarised target [12]. Together, all the work mentioned in the above paragraph should help to build a model-independent understanding of the baryon resonance spectrum and aid in the determination of resonant states, whether so-called 'missing' or

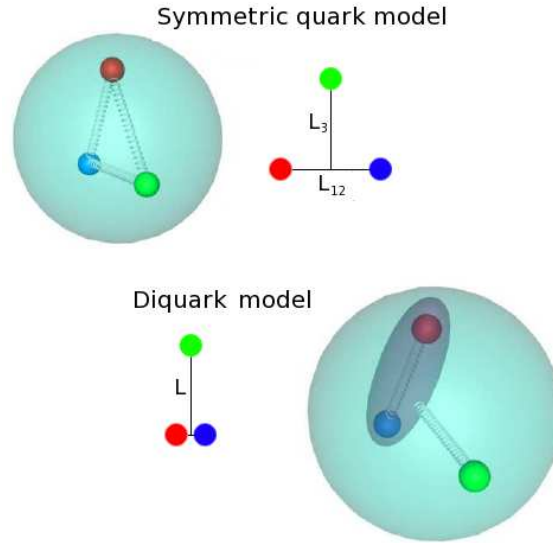


Figure 1.2: Representation of two different types of quark model. Top shows the constituent quark model and below is the diquark model.

not.

1.1 The Λ and Σ^0 Hyperons

Both the Λ and the Σ particles are part of a larger family of particles known as the hyperons, denoted by Y . Hyperons themselves are fermions, in that they all have half-integer spins and obey Fermi-Dirac statistics. They are composed of three light quarks, at least one of which is a strange quark, which makes them strange baryons. Both contain the same uds valence quark content, but in the Λ the ud quarks are in a spin singlet state, whilst in the Σ^0 they are in a spin triplet state. Each one has spin $\frac{1}{2}$ and is from the same baryon octet as the proton and neutron. The mass of the Λ is $1115.68 \text{ MeV}/c^2$ and its mean lifetime is $2.6 \times 10^{-10} \text{ s}$, whereas the Σ^0 has a mass of $1192.64 \text{ MeV}/c^2$ and a mean lifetime of $7.47 \times 10^{-20} \text{ s}$. One other major difference between these two hyperons is that the Λ has isospin 0 and the Σ has isospin 1. When considering the field of baryon spectroscopy, this is a vital concept as it implies that final states involving $K\Sigma^0$ may include the excitation of both N^* and Δ states whereas those involving $K\Lambda$ final states can only include intermediate $\frac{1}{2}N^*$ states. An important property of $K\Lambda$ photoproduction, this isospin selectivity makes the reaction simpler to describe with no Δ states contributing to it. A table listing the main properties of the Λ and Σ^0 hyperons is given in table 1.3.

Given the short lifetimes of both hyperons, one apparent consequence is that they will not travel far enough to be detected by the CLAS spectrometer. Given this fact, the particles must be reconstructed from their respective decay products. For the Λ , 63.9% of the time it decays through the mode

$$\Lambda \longrightarrow p\pi^- \quad (1.1)$$

| N^* | Status | $SU(6) \otimes O(3)$ | Parity | Δ^* | Status | $SU(6) \otimes O(3)$ |
|-----------------|--------|----------------------|--------|-----------------|--------|----------------------|
| P_{11} (938) | **** | $(56, 0^+)$ | + | P_{33} (1232) | **** | $(56, 0^+)$ |
| S_{11} (1535) | **** | $(70, 1^-)$ | - | | | |
| S_{11} (1650) | **** | $(70, 1^-)$ | - | S_{31} (1620) | **** | $(70, 1^-)$ |
| D_{13} (1520) | **** | $(70, 1^-)$ | - | D_{33} (1700) | **** | $(70, 1^-)$ |
| D_{13} (1700) | *** | $(70, 1^-)$ | - | | | |
| D_{15} (1675) | **** | $(70, 1^-)$ | - | | | |
| P_{11} (1520) | **** | $(56, 0^+)$ | + | | | |
| P_{11} (1710) | *** | $(70, 0^+)$ | + | P_{31} (1875) | **** | $(56, 2^+)$ |
| P_{11} (1880) | | $(70, 2^+)$ | + | P_{31} (1835) | | $(70, 0^+)$ |
| P_{11} (1975) | | $(20, 1^+)$ | + | | | |
| P_{13} (1720) | **** | $(56, 2^+)$ | + | | | |
| P_{13} (1870) | * | $(70, 0^+)$ | + | P_{33} (1600) | *** | $(56, 0^+)$ |
| P_{13} (1910) | | $(70, 2^+)$ | + | P_{33} (1920) | *** | $(56, 2^+)$ |
| P_{13} (1950) | | $(70, 2^+)$ | + | P_{33} (1985) | | $(70, 2^+)$ |
| P_{13} (2030) | | $(20, 1^+)$ | + | | | |
| F_{15} (1680) | **** | $(56, 2^+)$ | + | F_{35} (1905) | **** | $(56, 2^+)$ |
| F_{15} (2000) | ** | $(70, 2^+)$ | + | F_{35} (2000) | ** | $(70, 2^+)$ |
| F_{15} (1995) | | $(70, 2^+)$ | + | | | |
| F_{17} (1990) | ** | $(70, 2^+)$ | + | F_{37} (1950) | **** | $(56, 2^+)$ |

Table 1.2: PDG star ratings for measured and missing baryon resonances [1].

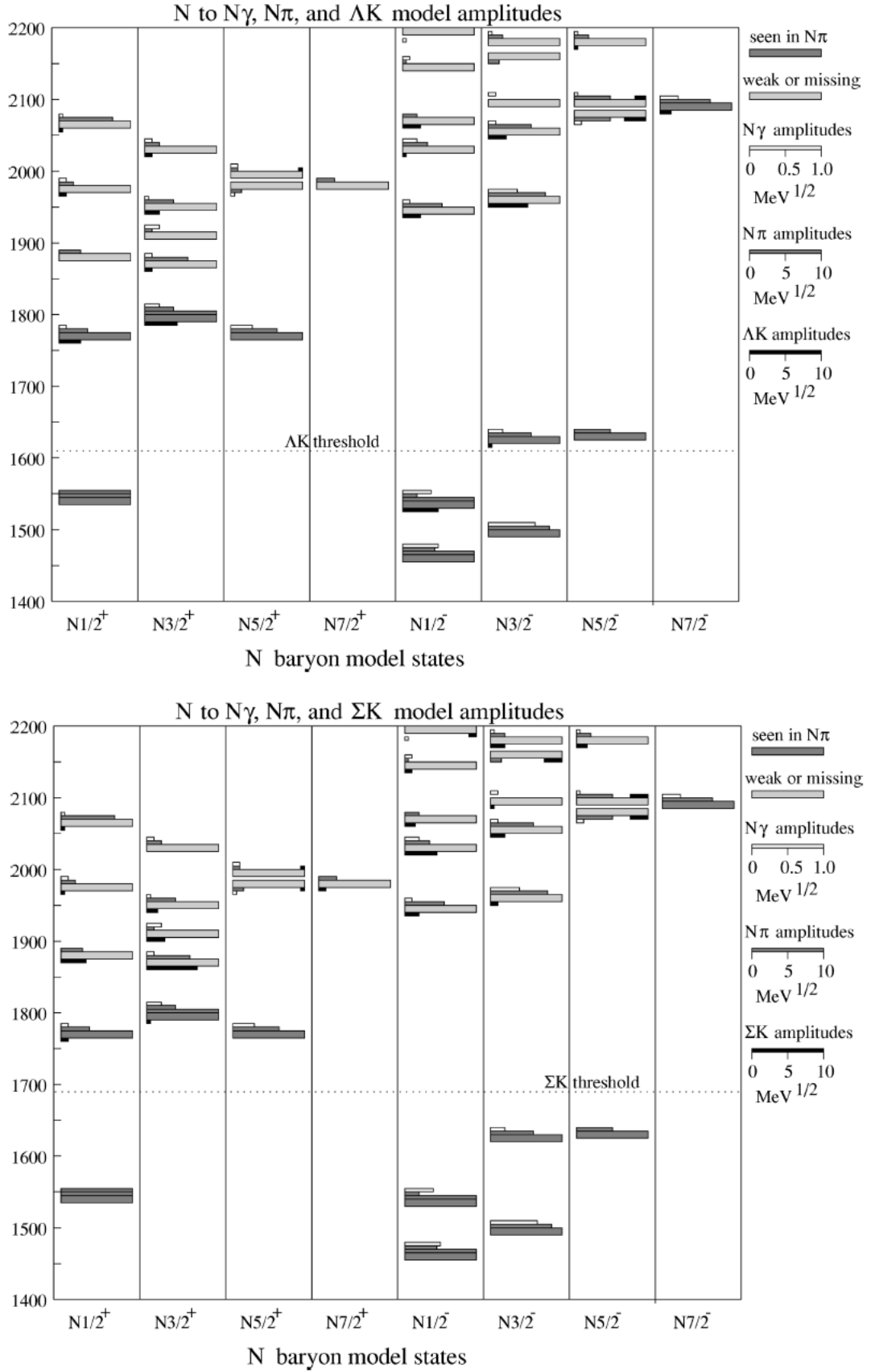


Figure 1.3: Mass predictions for $N\gamma$, $N\pi$ and ΛK (top) and ΣK (bottom) states from Capstick and Roberts' [2] relativised quark model. Heavy bars indicate well established states from partial wave analyses and light bars indicate poorly established or missing states. Y-axis scale is in MeV.

| | Λ | Σ^0 |
|----------------------------|-----------------------|-----------------------|
| Rest Mass (<i>GeV</i>) | 1.116 | 1.192 |
| Quark Content | <i>uds</i> | <i>uds</i> |
| Isospin | 0 | 1 |
| Spin | $\frac{1}{2}$ | $\frac{1}{2}$ |
| Parity | + | + |
| Mean Lifetime (<i>s</i>) | 2.6×10^{-10} | 7.4×10^{-20} |

Table 1.3: Main properties of the Λ and Σ^0 hyperons from the PDG [1].

the hyperon's polarisation. This unique property comes from the interference of the parity violating S and the parity conserving P wave amplitudes. For the Λ a polarisation component, $P_{\Lambda i}$, can be defined, where $i \in \{x, y, z\}$ is a given axis in space. The angular intensity distribution of the proton, $I(\cos \theta_{\Lambda}^p)$ as a function of the proton polar angle in the hyperon rest frame, θ_{Λ}^p is given by the following:

$$I(\cos \theta_{\Lambda}^p) = \frac{1}{2}(1 + \alpha P_{\Lambda} \cos \theta_{\Lambda}^p), \quad (1.4)$$

where α is the self-analysing power of the hyperon (the weak decay asymmetry parameter) which has been measured to be 0.642 [1]. As a result of this relation, the Λ polarisation can be extracted from the proton angular distribution without having to use a polarimeter device.

1.2 Summary

At the energies of the boundary between nuclear and particle physics, QCD becomes non-perturbative and continues to present a major obstacle to any further understanding of nucleon structure and interaction using this method. The field of baryon spectroscopy however, presents us with an ideal way to investigate the underlying physics and internal mechanics of a nucleon via its excited states. So far, the majority of the theoretical work done for the baryon resonance spectrum has come from quark model calculations, since chiral perturbation theory is not amenable to N^* physics, and lattice QCD is still developing. The biggest issue comes from the fact that quark models predict more resonances than have so far been observed experimentally. Most of our current understanding of the baryon resonance spectrum has come from pion/nucleon interactions such as $\pi N \rightarrow \pi N$, $\gamma N \rightarrow \pi N$ [13], however, there are quark model calculations that predict some of these missing resonances could couple strongly to $K^+\Lambda$ and $K^+\Sigma^0$ final states [2]. At centre-of-mass (CM) energies below about 1.7 GeV, the

single pion production channel dominates both pion and photoabsorption cross-sections. As the CM energy increases towards 2.0 GeV, two and three pion decay channels start to dominate and it is within this range that the partial widths and masses are not well determined.

This analysis used a linearly polarised photon beam to measure the beam asymmetry, Σ , polarisation observable in strangeness photoproduction. One of several polarisation observables which are expected to be very sensitive to resonance contributions. The results were then compared to similar measurements from the free proton in order to test the validity of the quasifree approximation of the bound nucleon in deuterium.

The results of this analysis which compares data on the free and quasifree proton provides a rigorous basis for further analyses involving strangeness production on the quasifree neutron. Results which show a clear relationship between the quasifree and elementary proton data will validate analyses on the $\gamma n \rightarrow KY$ channels, where elementary reactions are not possible. Such an analysis on the g13 dataset is already underway, but is not the focus of this thesis.

Chapter 2

Background

This chapter outlines the motivation for the extraction and analysis of the beam asymmetry (Σ) polarisation observable from the $K^+\Lambda$ and $K^+\Sigma^0$ photoproduction channels. Some of the phenomenological models used in the non-perturbative energy region of QCD are investigated and a selection of tree-level isobar, coupled-channel and Regge models are looked at, with their relative achievements and constraints in describing the baryon resonance spectrum being highlighted. Particular focus is given to the different theoretical schemes used, alongside different predictions for the various polarisation observables. Naturally, most attention is given to the beam asymmetry and the final results compared to model calculations. The resonance states predicted to strongly couple to the $K^+\Lambda$ and the $K^+\Sigma^0$ channels by these models are then highlighted.

The present world database for polarisation observables in $K^+\Lambda$ and $K^+\Sigma^0$ is also studied. Data from this is then compared to model predictions to provide an overview of contemporary theoretical understanding of hyperon photoproduction. Ultimately, the aim of this analysis is to compare its results of beam asymmetry measurements in kaon photoproduction from a quasifree proton in deuterium to those of a free proton. When considering the mechanics of production from a quasifree proton then rescattering effects in the final state interaction must be taken into account. The dominant processes in kaon photoproduction of kaons from the deuteron are shown in figure 2.1. Full expressions for the corresponding amplitudes are given in reference [14]. As an example here we consider only the $\gamma d \rightarrow K^+\Lambda(n)$ reaction, this being one of the relevant channels in this analysis. Graph I in figure 2.1 represents the quasifree production of the K^+ on the proton, with the neutron being a spectator in this reaction. This process dominates at low values of spectator neutron momentum p_n . The spectator neutron momentum distribution within the deuteron which is parameterised according to the Ar-

gonne potential [15] can be seen in figure 2.2. Kaon-nucleon and lambda-nucleon (graphs II and III, respectively) rescatterings become dominant above $p_n \sim 300$ MeV/c. The physical interpretation is as follows: The Λ , or the K , is produced on a nucleon at rest and rescatters on the second nucleon, also at rest in the deuteron, which then recoils with the observed momentum p_n . Here, the rescattering amplitude is well defined and relies on the low-momentum components of the deuteron wave function. This is an ideal place to study the interactions with nucleons with short-lived particles (such as the various hyperons) or to look for narrow resonant states (*e.g.*, in the K^+n channel). Graph IV represents the case where the kaon is produced by the rescattering of an intermediate pion, though this process was not included in any models used in the experimental proposal for this analysis. Experimentally, however, it can be studied using the same approach as graphs II and III.

When the results of this analysis are finally compared to those measured previously on the free proton, it is not expected that there will be much disparity observed between the two sets of results. This is a theory borne out by work done on models by groups such as those described in reference [16], an idea that is expanded on in detail in section 2.4.4.

2.1 Baryon Spectroscopy

Meson photoproduction is an important topic in the field of baryon spectroscopy as it allows the determination of the parameters of known resonances alongside helping the discovery of new baryon states, should they exist. Currently, hadronic physics has been forced to rely upon phenomenological quark models in order to make predictions about the baryon spectrum, due to the under development of lattice QCD and the non-perturbative nature of QCD at low momenta and energies. These phenomenological models, while they may differ in structure, all basically utilise the same technique of simplifying the complex quark-gluon soup of QCD into a system of constituent quarks interacting in some inter-quark potential. Various excited states of the nucleon can be predicted by these quark models when the rules of the standard model are applied. By restricting ourselves to combinations of the three lightest quarks one can use the standard model to make predictions about the ground state spectrum for baryons and mesons. It is then possible to excite these ground states into various higher energy resonance states. These resonance states are represented by the L_{2I2J} notation where L is the orbital angular momentum in spectroscopic notation, I is the isospin and J

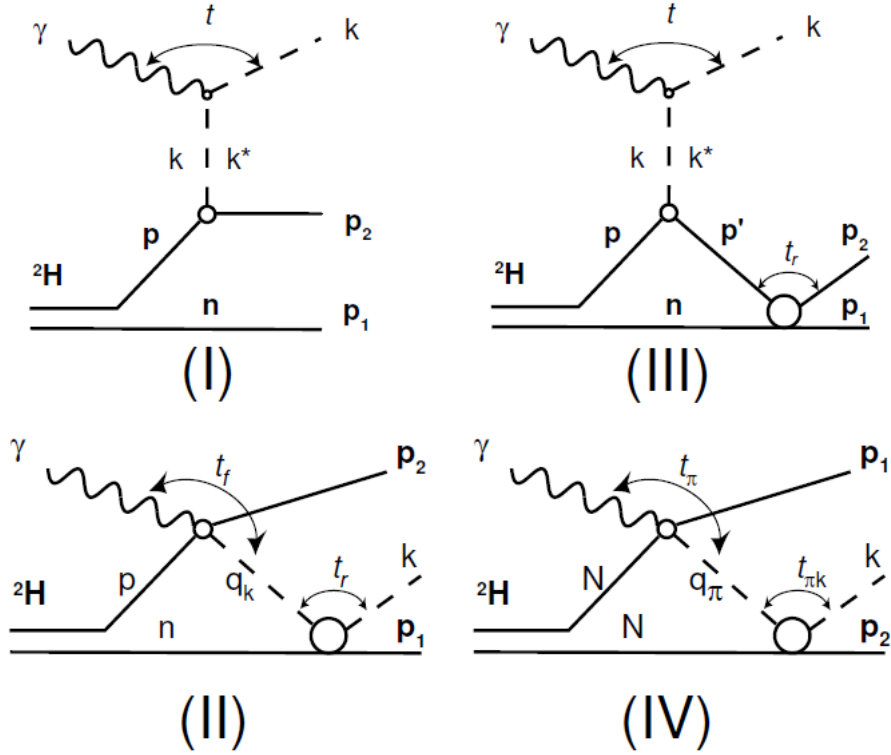


Figure 2.1: The relevant graphs in the $\gamma d \rightarrow K^+ \Lambda(n)$ reaction. I: Quasifree kaon photoproduction; II: Kaon-nucleon rescattering; III: Lambda-nucleon rescattering and IV: Intermediate state reactions. Figure from reference [17].

is the total angular momentum of the resonance.

2.2 Polarisation Observables in Hyperon Photo-production

2.2.1 Formalism

The g13 experiment is part of the N^* program at JLab. It is an ongoing program of study to gain a clearer understanding of the structure of the nucleon, along with quark and hadronic interactions at low energy and momenta, the range of non-perturbative QCD. The focus of the N^* program is to develop an improved understanding nucleon structure and interactions in the low energy and momenta range of QCD by studying its excited states. The spectrum of excited states of a system of bound particles opens a window to the underlying interaction. Likewise, in nuclear spectroscopy, where the excited state spectrum indicates the quantum many-body configurations of nucleons and mesons interacting via the strong force, so too in baryon spectroscopy we are able to gather information on the interactions

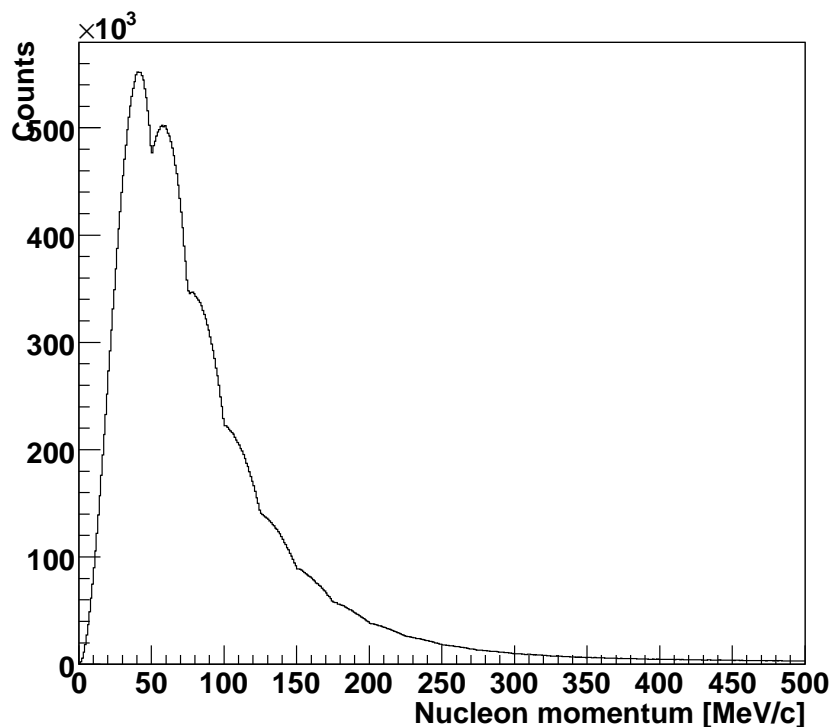


Figure 2.2: The Argonne potential describes the nucleon momentum distribution within the deuterium nucleus. This plot shows the momentum distribution that arises from the Argonne potential.

of quarks and gluons in excited states by studying these so-called resonances. Historically, polarisation observables have been demonstrated to be an ideal probe when investigating hadronic processes. When considering reactions that involve the photoproduction of pseudoscalar mesons these observables are of particular interest, as suitable combinations of observables allow for model independent analyses. Once an appropriate expression for the scattering amplitudes of kaon photoproduction has been found, one that is sensitive to the contributions of each state and channel [18], they are then expressed as a combination of four amplitudes [19]. These are then written as functions of energy and scattering angle [20], though to assist in the study of polarisation observables it is usually convenient to change to a transversity amplitude representation [20].

Barker and Donnachie [21] used a formalism that allows the transversity amplitudes to be expressed in terms of s-channel helicity flips N , S_1 , S_2 and D . In this representation N is a no-flip amplitude, S_1 and S_2 are single-flip amplitudes and D is a double flip amplitude. The amplitudes are now written:

$$b_1 = \frac{1}{2}[(S_1 + S_2) + i(N - D)], \quad b_2 = \frac{1}{2}[(S_1 + S_2) - i(N - D)],$$

$$b_3 = \frac{1}{2}[(S_1 - S_2) - i(N + D)], \quad b_4 = \frac{1}{2}[(S_1 - S_2) + i(N + D)]. \quad (2.1)$$

These four complex amplitudes can completely describe the photoproduction process. By taking bilinear combinations of them one can define 16 polarisation observables [21]. The 16 polarisation observables can be divided into two groups: single and double polarisation observables. Unlike electroproduction, there are no triple polarisation observables, involving beam, target and recoil polarisation, to worry about in kaon photoproduction. It should be pointed out that the Σ hyperon (strange baryon) and the Σ polarisation observable are two unique and unrelated entities and care should be taken not to confuse them when discussing the process of strange decays in Kaon photoproduction and the manipulation of polarisation observables. The cross-section and beam asymmetry polarisation observables are shown in table 2.1 alongside their associated transversity amplitudes.

| Symbol | Transversity representation |
|-----------------------------|---|
| $\frac{d\sigma}{dt}$ | $ b_1 ^2 + b_2 ^2 + b_3 ^2 + b_4 ^2$ |
| $\Sigma \frac{d\sigma}{dt}$ | $ b_1 ^2 + b_2 ^2 - b_3 ^2 - b_4 ^2$ |

Table 2.1: The differential cross-section and beam asymmetry polarisation observables alongside their associated transversity representations.

Polarisation observables are sensitive to the predictions by the various models and by measuring them we can place constraints on the models and test their validity. Starting from a simple model that includes all the known resonances one can then add further resonances to the model and compare how well their addition brings the model to describing the data. This analysis aims to measure the beam asymmetry single polarisation observable Σ . Once the results of this analysis have been compared to those of the free proton an assessment can then be made of the validity of the quasifree approximation of the bound nucleon in deuterium and thus whether analyses on the quasifree neutron can be reliably compared to the “free” neutron.

2.2.2 Extraction of Observables

The differential cross-section is related to the beam asymmetry via the following relation:

$$\frac{d\sigma}{d\Omega} = \sigma_0 \{1 - P_{lin}\Sigma \cos 2\phi\}, \quad (2.2)$$

where, $\frac{d\sigma}{d\Omega}$ is the differential cross-section, σ_0 is the unpolarised cross-section, P_{lin} is the degree of linear polarisation of the photon beam and ϕ is the azimuthal angle of the detected meson in the centre-of-mass frame.

In order to measure the asymmetry without measuring both cross-sections, it is possible to reconstruct the unpolarised input by using different polarisation vectors. Two polarisation planes with an angular difference of 90° provides a phase difference of 180° in the $\cos 2\phi$ distribution, thus a cross-section can be defined for both planes:

$$\sigma_1 = \sigma_0 \{1 - P_{lin}\Sigma \cos 2\phi\}, \quad (2.3)$$

$$\sigma_2 = \sigma_0 \{1 + P_{lin}\Sigma \cos 2\phi\}, \quad (2.4)$$

where σ_1 and σ_2 are the cross-sections at the two different plane settings. Equivalence of these equations allows the rearrangement for Σ :

$$\frac{\sigma_1(\phi) - \sigma_2(\phi)}{\sigma_1(\phi) + \sigma_2(\phi)} = P_{lin}\Sigma \cos 2\phi \quad (2.5)$$

2.3 Theoretical Models

2.3.1 Isobar Models

Isobar frameworks at the order of the tree-level have been developed by numerous groups in order to try and unfold the nucleon resonance excitation spectrum [22–24]. Pioneered by Thom [25], the aim of these models is to describe the hadronic reaction by evaluating various tree-level Feynman diagrams for both resonant and non-resonant exchange of mesons and baryons. Here, every reaction particle can be considered as an effective field with properties such as photocoupling amplitudes, mass and strong decay widths. While a tree-level approach may not account for channel coupling effects and final state interactions, it does reduce the complexity of the interaction and give a reliable first order understanding of the resonance parameters. In a typical tree-level approach, the Feynman diagrams contributing to the $\gamma p \rightarrow K^+ \Lambda$ reaction are shown in figure 2.3, diagrams (a) to (g). Diagrams (a) to (d) represent the Born terms while (e) to (g) represent resonant contributions in the t, u and s-channels respectively. Diagram (h) is only

used when considering the $K^+\Sigma^0$ final state as contribution from the Δ states also have to be included.

The prescription of Mart and Bennhold [11] was one of the first isobar models to show evidence for a potential missing resonance in strangeness photoproduction. Their model investigated $K^+\Lambda$ photoproduction, as its isospin structure only allows the excitation of N^* states, whereas the $K^+\Sigma^0$ channel also allows Δ states to contribute, therefore making it more complicated to describe. They were guided in their analysis by the coupled-channels approach of Feuster and Mosel [26] which gave an indication that the three core resonant states $S_{11}(1650)$, $P_{11}(1710)$ and $P_{13}(1720)$ should be predominant in the $K^+\Lambda$ channel. The model described the background using the standard Born terms along with $K^*(892)$ and $K_1(1270)$ vector meson poles in the t-channel. Hadronic form factors were included using the gauge method developed by Habberzettl [27]. Background and resonance sectors were suppressed by using separate cutoff masses of 800 and 1890 MeV respectively .

The development of this model was an attempt to reproduce the cross-section results of the SAPHIR collaboration [28], as shown in figure 2.4. The model appears to describe the overall shape of the data well but does not accurately reproduce the feature seen at around $W=1900$ MeV. To be able to incorporate this structure they used the constituent quark model of Capstick and Roberts [2] to lead the development of their own model. The prescription of Capstick and Roberts [2] predicts the existence of various new states around 1900 MeV. Of these, the $D_{13}(1960)$, was predicted to have a significant decay width into, and photocoupling to, the $K^+\Lambda$ channel. This missing resonance state was then included in the model calculations and the results agreed well with the cross-section measurements, shown in figure 2.4. When this result is considered in concert with the good agreement between the extracted partial widths for the core resonances with the quark model predictions, it lends some credence to the belief that the structure in the SAPHIR cross section data does correspond to the $D_{13}(1960)$. Their calculations also predict large differences between models that include and exclude the $D_{13}(1960)$ resonance for the photon asymmetries as shown in figure 2.5. Specifically, Mart and Bennhold conclude that a measurement of the photon asymmetry would be an ideal way of examining the role of the $D_{13}(1960)$ missing resonance in kaon photoproduction.

Further investigation of the SAPHIR data by Saghai et al [29] showed that the cross-section results could be reproduced equally well while still excluding a $D_{13}(1960)$ resonance. This model adjusts the background by including two

hyperonic resonances, $P_{01}(1810)$ and $P_{03}(1890)$, to accurately reproduce the fitted data. This approach highlights the risk taken in using limited observables when drawing conclusions about the possible existence or non-existence of predicted missing resonances in an isobar approach.

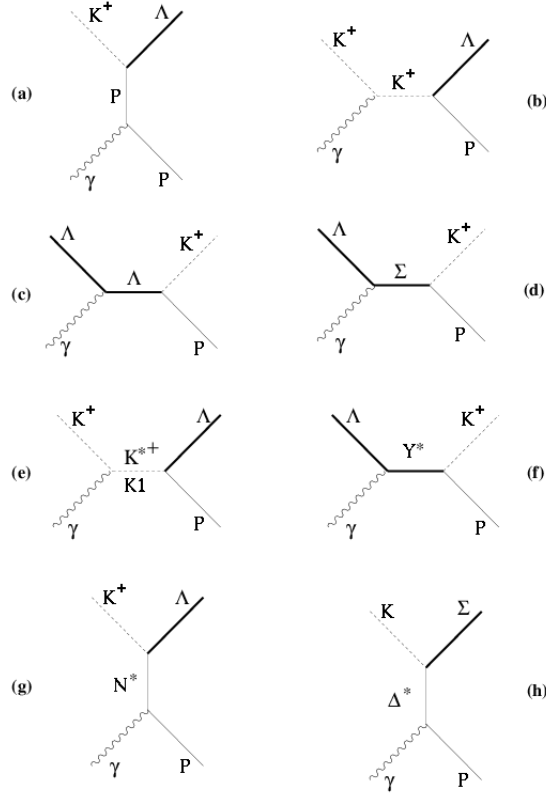


Figure 2.3: Feynman diagrams for the $\gamma p \rightarrow K^+ \Lambda$ reaction, diagrams (a) to (g) and for the $\gamma p \rightarrow K^+ \Sigma^0$ reaction diagram (h) is included. Diagrams (a) to (d) represent the Born terms and (e), (f) and (g) represent the resonant contributions from the t, u and s-channels respectively. Diagrams from [12].

2.3.2 Coupled-Channel Analyses

One major drawback of tree-level isobar models lies in their inability to account for multi-step, coupled-channel effects arising from intermediate states along with final state interactions. It is the currently held belief that the multi-step sequence $\gamma N \rightarrow \pi N \rightarrow KY$ should have a large effect in kaon photoproduction because of the $\gamma N \rightarrow \pi N$ amplitudes being significantly larger than the direct production process. Several groups have constructed models in an attempt to account for these coupled-channel effects [26, 31–33] including approaches based upon $SU(3)$ chiral dynamics [34] and a K-matrix interpretation [26].

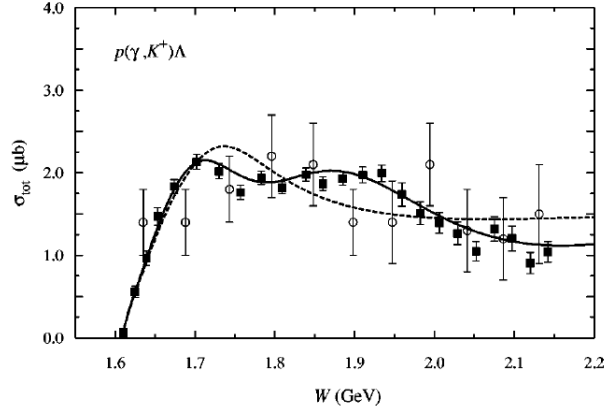


Figure 2.4: Total cross section from $K^+\Lambda$ production on the proton, shown with calculations from the Mart and Bennhold model [11]. Dashed line indicates calculation without $D_{13}(1960)$ resonance and the solid line indicates the calculation with this resonance included. Data from SAPHIR, new (1998) [28] shown by solid squares and old (1969) [30] by open circles.

Chiang et al [35] developed a coupled-channel model which investigated the $\gamma p \rightarrow K^+\Lambda$ channel by fixing the number of leading order tree-diagrams to be considered using the isobar model developed by Williams, Ji and Contach [24]. The approach they used had the $\gamma N \rightarrow \pi N$ and $\pi N \rightarrow KY$ amplitudes defined using the results from the VPI partial wave analysis [36]. To reduce the number of free parameters in the calculation they developed an approach similar to that used in some isobar models, where the coupling constants are fixed from either PDG values or $SU(3)$ flavour symmetry. Chiang's model did not attempt to accurately reproduce known kaon photoproduction data, but instead aimed to highlight the importance of coupled-channel effects. Ultimately, Chiang concluded that πN channels provide $\sim 20\%$ contribution via the coupled-channel mechanism, demonstrating a clear need for these effects to be accounted for in kaon photoproduction calculations. Usov and Scholten [37] further confirmed this hypothesis by their K-matrix approach which showed channel coupling effects to be large and should not be ignored.

A dynamic coupled-channel formalism was also developed by Julia-Diaz for the processes $\gamma N \rightarrow \pi N \rightarrow KY$ and $\gamma N \rightarrow \pi N$, to provide a comprehensive description of the $\gamma p \rightarrow K^+\Lambda$ reaction. A chiral constituent quark model formed the foundation of this model, one that properly incorporated off-shell effects. Non-resonant interaction within the $KY \oplus \pi N$ subspace was determined using an approach utilising unitary transformations. In their model, simplification of the photoproduction amplitude calculations were made by casting the coupled channels in such a way that the $\gamma N \rightarrow \pi N$ am-

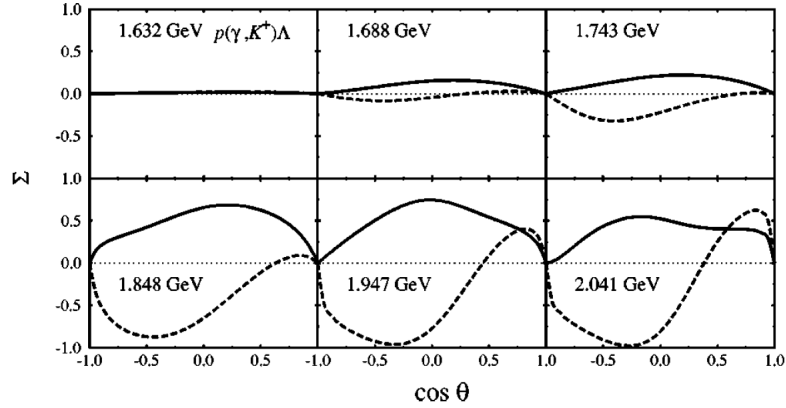


Figure 2.5: Mart and Bennhold calculations [11] for the photon asymmetry. Dashed line represents calculations without a $D_{13}(1960)$ resonance whilst the solid line has the $D_{13}(1960)$ included. These calculations predict that the photon asymmetry should be very sensitive to the inclusion of a missing $D_{13}(1960)$ resonance.

plitudes were explicitly input. As a result, solely parameters associated with the KY channels need to be determined. This is achieved by fitting to all the existing data for the coupled channels. There was found, generally, to be good agreement between the model calculations and the data.

Model calculations compared to available cross section data from both SAPHIR and CLAS are shown in figure 2.6. Two model prescriptions were used in the calculations, one using fits to all SAPHIR and the most recent CLAS data (the M1 model), and the other using simultaneous fits to all available cross section and polarisation data. Studying the fit results of both models showed the SAPHIR cross section data had a greater compatibility with the polarisation measurements than the CLAS results. Overall, it was found that the main known resonances contributing to the $\gamma p \rightarrow K^+ \Lambda$ reaction were the $S_{11}(1535)$, $S_{13}(1900)$ and the $D_{13}(1520)$ with smaller contributions coming from the $F_{15}(1680)$ and the $F_{15}(2000)$. Investigation was also carried out into previously unknown states and strong evidence was found for the inclusion of a D_{13} resonance at 1954 MeV and some weak evidence for a possible S_{11} state at 1.804 GeV. Observations were also made for non-negligible effects from a P_{13} state at 1.893 GeV.

2.3.3 Regge Models

By extending angular momentum into the complex plane, Regge models have been shown to provide an accurate description of high energy particle physics data. The theory evolved from the need to account for poles in a partial wave

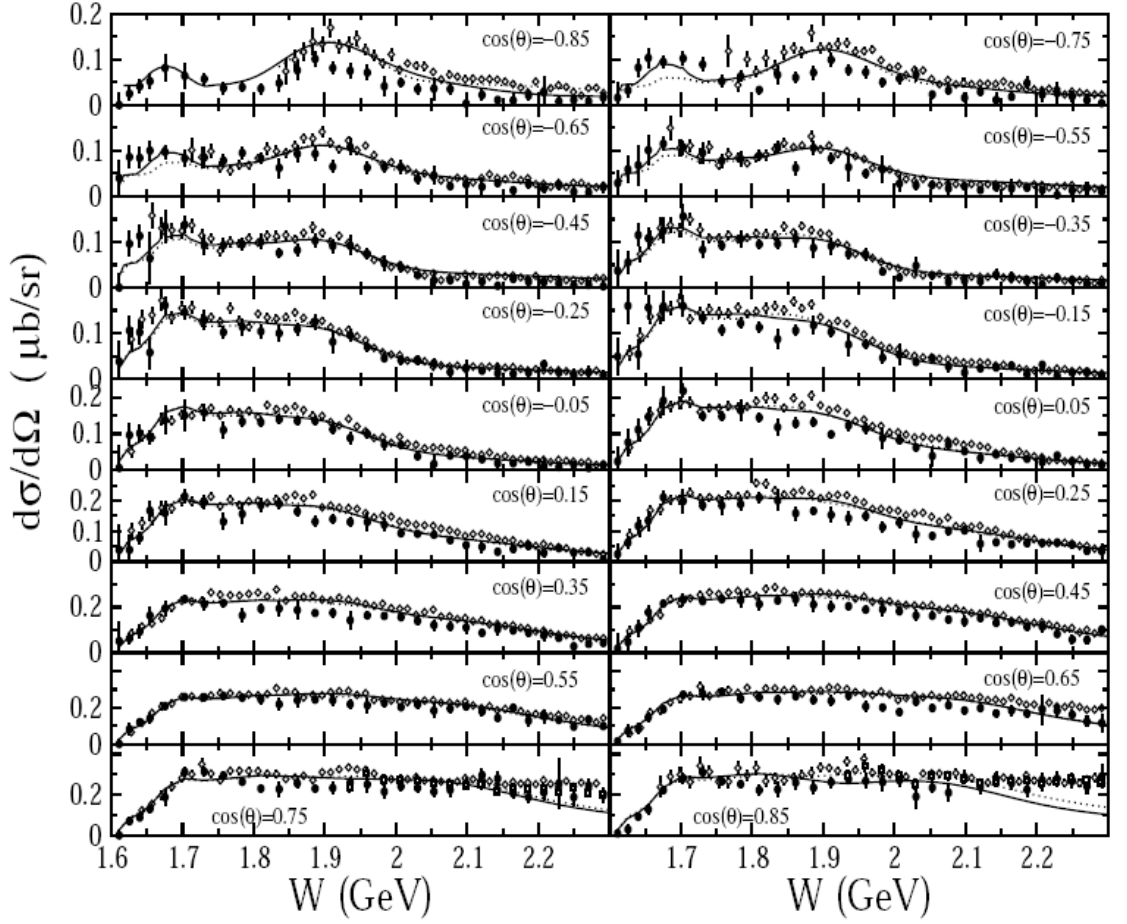


Figure 2.6: M1 (dotted curve) and M2 (solid curve) coupled-channels calculations from Julia-Diaz [38] for the reaction cross section of $\gamma p \rightarrow K^+ \Lambda$. Calculations are compared to CLAS (open diamonds) [39], SAPHIR (full circles) [40] and LEPS (open squares) [41] results.

decomposition. In this formalism, particles that have the same internal quantum numbers but different spins are grouped into what are called Regge trajectories. It is then proposed that at sufficiently high energies, where individual resonances can no longer be clearly identified, the photoproduction process is then described by exchanging whole Regge trajectories, as opposed to individual particles. It is expected that the range of validity for these models occurs at high energies and forward angles but some recent studies have indicated that meson production in the resonance region could be reasonably well described by the Regge approach.

One recent way of reproducing the cross section and polarisation measurement values from hadronic reactions is with a “Regge-plus-resonance” (RPR) technique developed by Corthals, Ryckebusch and Van Cauern [42]. Their approach uses

Regge trajectory exchange in the t-channel to describe the $K + Y$ background. After this, the model predictions are evolved into the resonance region by adding s-channel resonances to describe the existing data. By construction, these resonances must disappear at higher energies, therefore the background can be constrained to high energy data. The advantage of this over isobar schemes is that only the resonance couplings are left as free parameters in the resonance region. The need for strong hadronic form factors for the background terms is also reduced by using Regge propagators and this, in turn, removes the gauge invariance issues that are so problematic in a purely isobaric approach. Figure 2.7 shows a representation of this approach where the photoproduction cross sections for hyperons is shown against the different energy regions for both resonance and Regge effects.

In the model by Corthals et al, K and K^* Regge exchange were used to describe the background and core resonances were incorporated to extrapolate the intermediate energy scheme. The effects of including a two star $P_{13}(1900)$ state and contributions from both the $D_{13}(1900)$ and $P_{11}(1900)$ missing resonances were investigated. Model calculations for different RPR regimes compared to beam asymmetry data are illustrated in figure 2.8. These results, in conjunction with previous cross section measurements give some evidence for the inclusion of the two star $P_{13}(1900)$ state. Regarding the previously unobserved states, the model calculations indicate the $P_{11}(1900)$ to be the more likely choice for a possible missing resonance as opposed to the $D_{13}(1900)$. However, the authors of reference [42] stated that they would be reluctant to claim strong evidence for the existence of either state from their results. Specifically, they highlight that a model utilising solely the core set of resonances can just as validly describe the reaction dynamics. From this they draw the conclusion that features seen in resonance spectra could be explained by fine tuning the background, rather than being indications of a missing state.

For the Σ hyperons, an RPR approach was developed whereby the reactions $p(\gamma, K^+)\Sigma^0$ and $p(\gamma, K^0)\Sigma^+$ could be treated in common isospin-related description [43, 44]. This was possible because the Σ^0 and Σ^+ hyperons belong to an isotriplet and the strong coupling strengths are related via $SU(2)$ Clebsch-Gordan coefficients. An important role for the two-star $P_{13}(1900)$ along with the standard N^* core resonances is suggested by the results of reference [43].

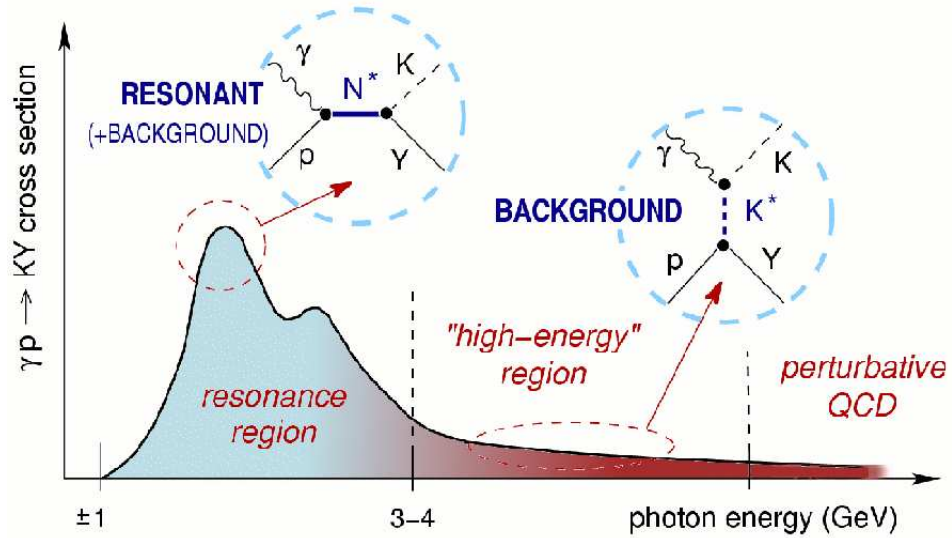


Figure 2.7: Representation of the different energy scales used in the Regge-plus-resonance approach. The higher energy region, above 3 GeV, models the background via the exchange of various Regge trajectories, whilst in the lower energy region s -channel resonances become more important. Figure taken from reference [44].

2.4 Previous Measurements

There are currently very few measurements or theoretical predictions for polarisation observables on the deuteron. Given the complexities highlighted in the previous chapter (1) it has been sensible to first establish model predictions and measurements for the simpler case of an unbound proton, from a hydrogen target. After this theorists and experimentalists can move forward onto the case of the bound proton in deuterium. As such, g13 is one of the first experiments to advance the field in this direction. In the following sections where measurements or predictions for the deuteron have been made, they are highlighted and compared with the more abundant proton data.

2.4.1 Photon Asymmetries on the free proton

Extensive measurements have now been made at GRAAL [45–48], LEPS [41, 49] and CLAS [7, 50, 51] on $K\Lambda$ and $K\Sigma^0$ channels. These results are summarised in figures 2.10 and 2.12.

At JLab, the most recent measurements were undertaken during an experiment known as g8b [52]. Here they used a hydrogen target and measured the beam asymmetry using a beam of linearly polarised photons in a similar energy

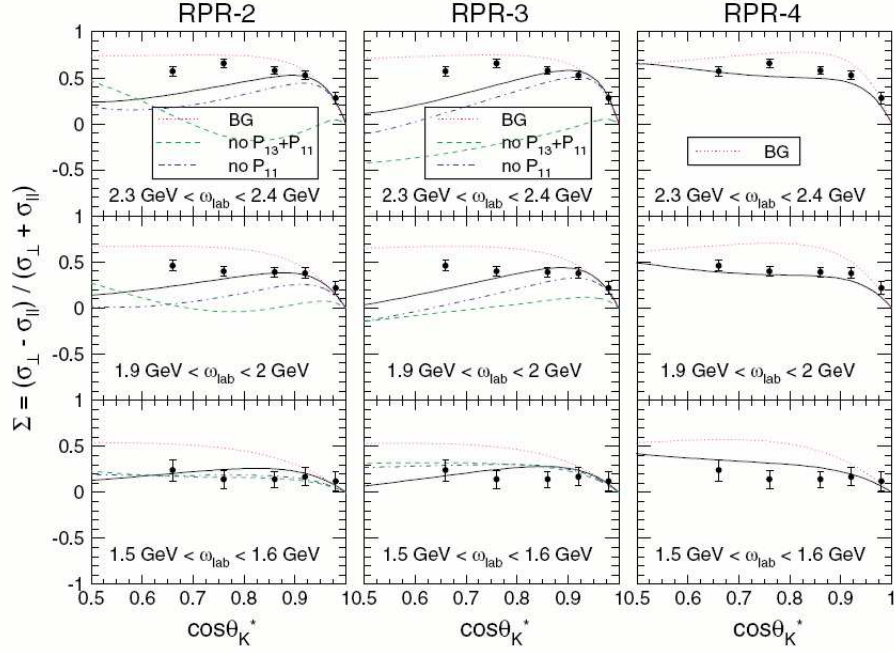


Figure 2.8: RPR model calculations [42] of the photon asymmetry for the $K\Lambda$ channel plotted against LEPS data [41]. Models RPR-2 and RPR-3 include the 2 star $P_{13}(1900)$ and the missing $P_{11}(1900)$, whilst model RPR-4 includes only the known core resonances.

range as that used in the current analysis ($g8b$, $E_\gamma = 1.3 - 2.1$ GeV in 200 MeV steps; $G13$, $E_\gamma = 1.3 - 2.3$ GeV in 200 MeV steps). Ultimately, the results of this analysis are compared to those beam asymmetry measurements made during $g8b$ and the validity of the quasifree approximation of the bound nucleon in deuterium determined. The $g8b$ experiment took data between the 20th June and 1st September 2005 at JLab.

By using a backward-Compton scattering facility the LEPS group produced a photon beam with a high degree of linear polarisation. The asymmetry measurement was made possible by taking one half of the data with horizontally polarised photons and one half with vertically polarised photons. Two drift chambers and a silicon-strip vertex detector allowed precision measurements of the K^+ momentum in order to assist in particle identification. In order to have a reliable start signal, a plastic scintillator trigger was used, placed behind the target cell, with another 40 scintillators placed behind the tracking detectors providing a stop signal.

The GRAAL collaboration in Grenoble, France used the European Synchrotron Radiation Facility (ESRF) to produce tagged, polarised photons via Compton scattering laser photons off of electrons circulating in the storage ring. For the

purposes of the hyperon experiment, UV lines were produced by an Argon laser at 333, 351 and 364 nm that went on to give photon energies of 1.40, 1.47 and 1.53 GeV respectively. Both neutral and charged particles were detected by the 4π LA γ RANGE detector. Charged particle tracking information was collected by using a set of MultiWire Proportional Chambers (MWPCs). Particle identification was provided by a plastic scintillator barrel in conjunction with a double plastic scintillator hodoscope which gave time-of-flight measurements. An in-depth treatment of the experimental setup is given in reference [45].

$K^+\Lambda$ channel

The first noticeable feature of the JLab results for the $K^+\Lambda$ channel is that they are positive over the full kinematic range of the analysis. Up to photon energies of about 1.375 GeV the asymmetry remains largely flat, whereafter it begins to display a slight peak at backwards angles, approaching a maximum of 1 at 1.675 GeV. As the photon energy increases, a second structure begins to emerge at $\cos\theta_{cm}^{K^+} = 0$, at a photon energy of around 1.775 GeV. Also, as the photon energy goes above 1.875 GeV, the peak at backward angles begins to drop off.

The JLab results were compared in figures 2.9 and 2.12 to previous measurements from GRAAL and LEPS respectively. The GRAAL data was all at photon energies below 1.5 GeV and covered nearly the full angular range. Overall, the agreement was very good with the GRAAL data, with the JLab analysis having nearly three times as many energy points per bin with smaller error bars, allowing for finer structural resolution. This proved useful at backward angles where a slight peak begins to appear at energies above 1.325 GeV that was not apparent in the GRAAL data. The LEPS data covered forward angles and energies above 1.5 GeV. Due to differences between the two datasets the JLab data was rebinned with coarser binning to allow a proper comparison. Again, the overall comparison was found to be good, with the LEPS data producing some slightly lower results. Systematic effects in one of the analyses was put forward as a suggestion for the small difference between the analyses.

$K^+\Sigma$ channel

The beam asymmetry results for the $K^+\Sigma^0$ channel is reasonably flat for photon energies below 1.625 GeV with a peak forming at backward angles above 1.675 GeV and a forward angle peak forming around 1.825 GeV. Just like the results for the $K^+\Lambda$ channel, the results are positive for nearly the entire kinematic range, with only some error bars moving into negative values at higher energies.

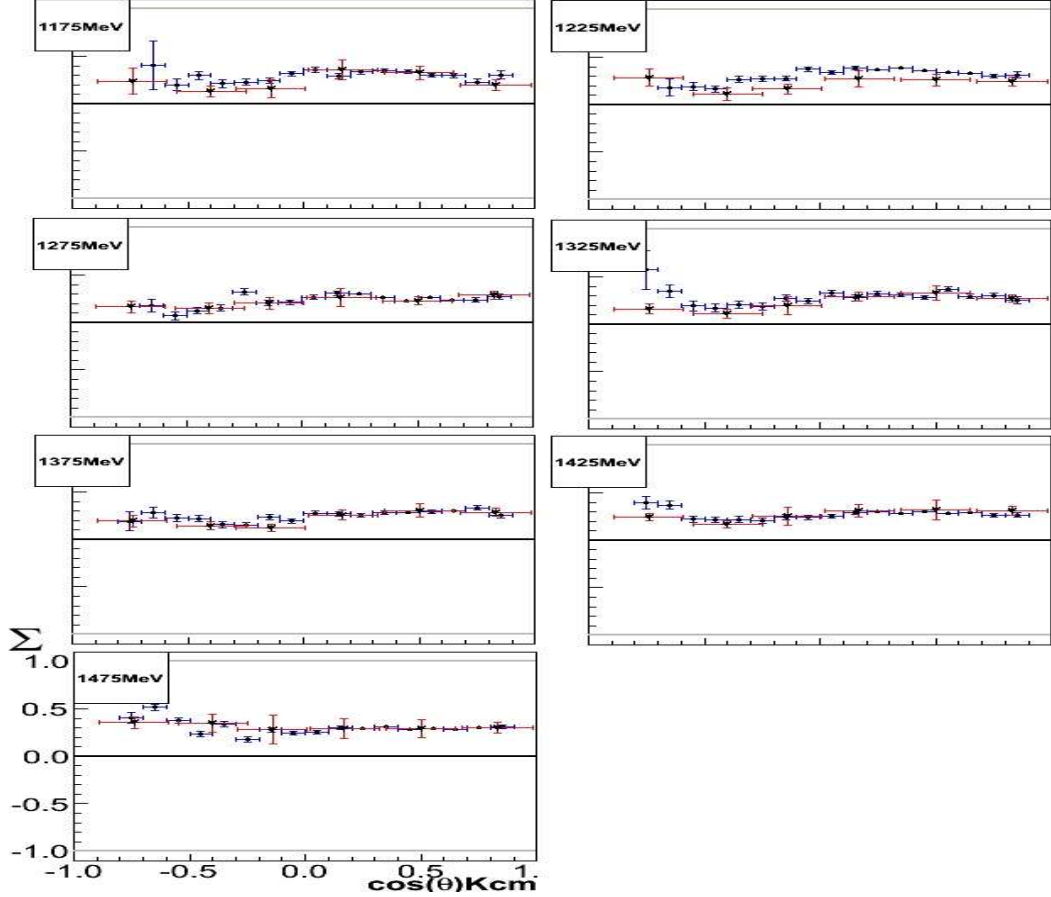


Figure 2.9: Photon asymmetries for the reaction $\gamma p \rightarrow K^+ \Lambda$ as a function of $\cos \theta_{cm}^{K^+}$. Comparison to GRAAL. JLab data is shown by circles with blue lines and those from GRAAL are indicated by triangles with red lines.

For the $K^+ \Sigma^0$ channel, comparison with the GRAAL data again (figure 2.12) showed very good agreement across the full kinematic range of comparison, with the LEPS data also showing good agreement at forward angles. There were only very slight differences with the LEPS data at higher energies.

2.4.2 Quasifree Proton

The GRAAL collaboration also published preliminary beam asymmetry for η photoproduction from the quasifree proton and neutron in deuterium in 2005 [48]. Exclusive measurements were made with the BGO Crystal Ball, with recoil neutrons and protons that were emitted at $\Theta_{lab} = 3 > 23^\circ$ being detected in an assembly of forward detectors. This forward detector assembly included two planar multiwire chambers, a time-of-flight wall made of thin scintillator strips, and a lead-scintillator sandwich TOF wall. The ηp and ηn final states were identified in a similar fashion as was used for previous measurements [46] on the

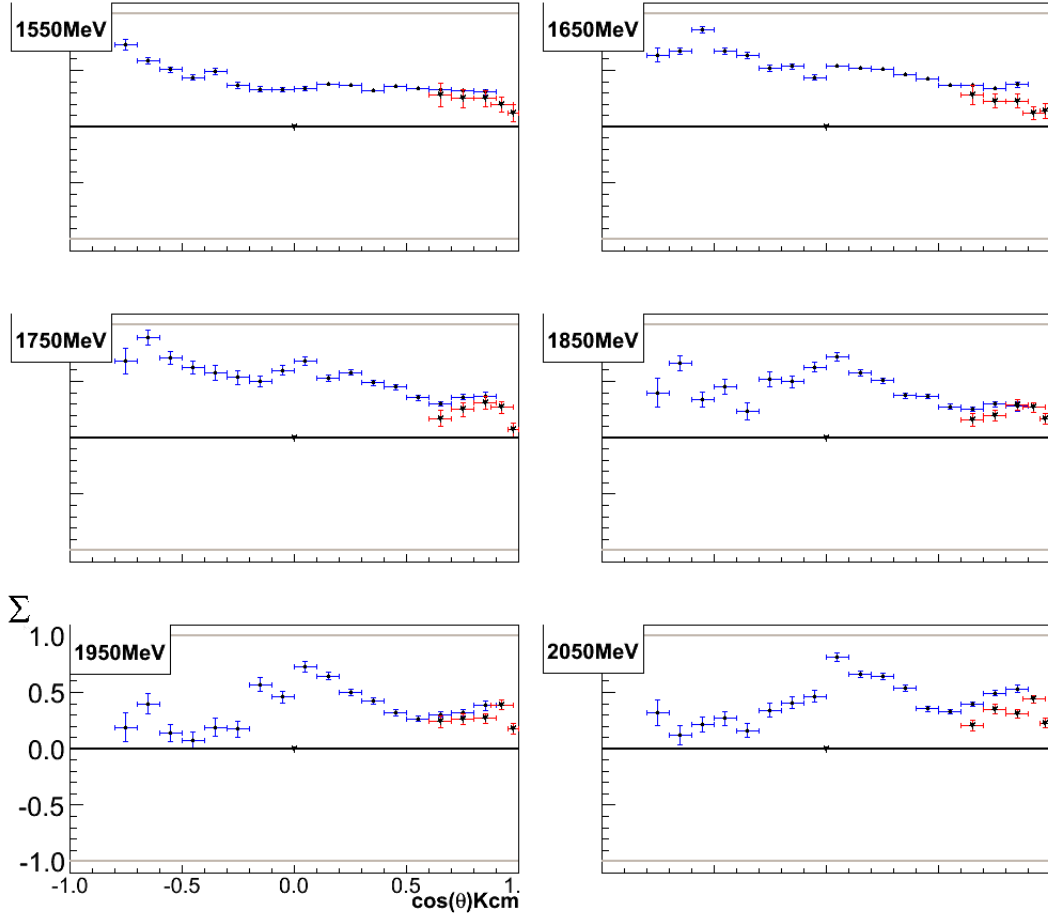


Figure 2.10: Photon asymmetries for the reaction $\gamma p \longrightarrow K^+ \Lambda$ as a function of $\cos \theta_{cm}^{K^+}$. Comparison to LEPS. JLab data is shown by circles with blue lines and those from LEPS are indicated by triangles with red lines.

free proton.

In the case of the beam asymmetry measurements (figure 2.13), in the region of the $S_{11}(1535)$ resonance, the beam asymmetry is roughly the same for both the neutron and proton, ~ 0.2 . At $W = 1.65 > 1.73$ GeV though there are opposite changes in both asymmetries. The proton beam asymmetry drops to almost 0 whereas the neutron beam asymmetry rises to ~ 0.4 . The GRAAL collaboration points out that the beam asymmetry measurements are more sensitive to the non-dominant contributions, as it is given by the interference of helicity amplitudes [53, 54]. They also go on to suggest that an observed peak in the neutron cross-section and a corresponding change in beam asymmetry may be an indication that one of the nucleon resonances has a stronger photocoupling to the neutron than to the proton.

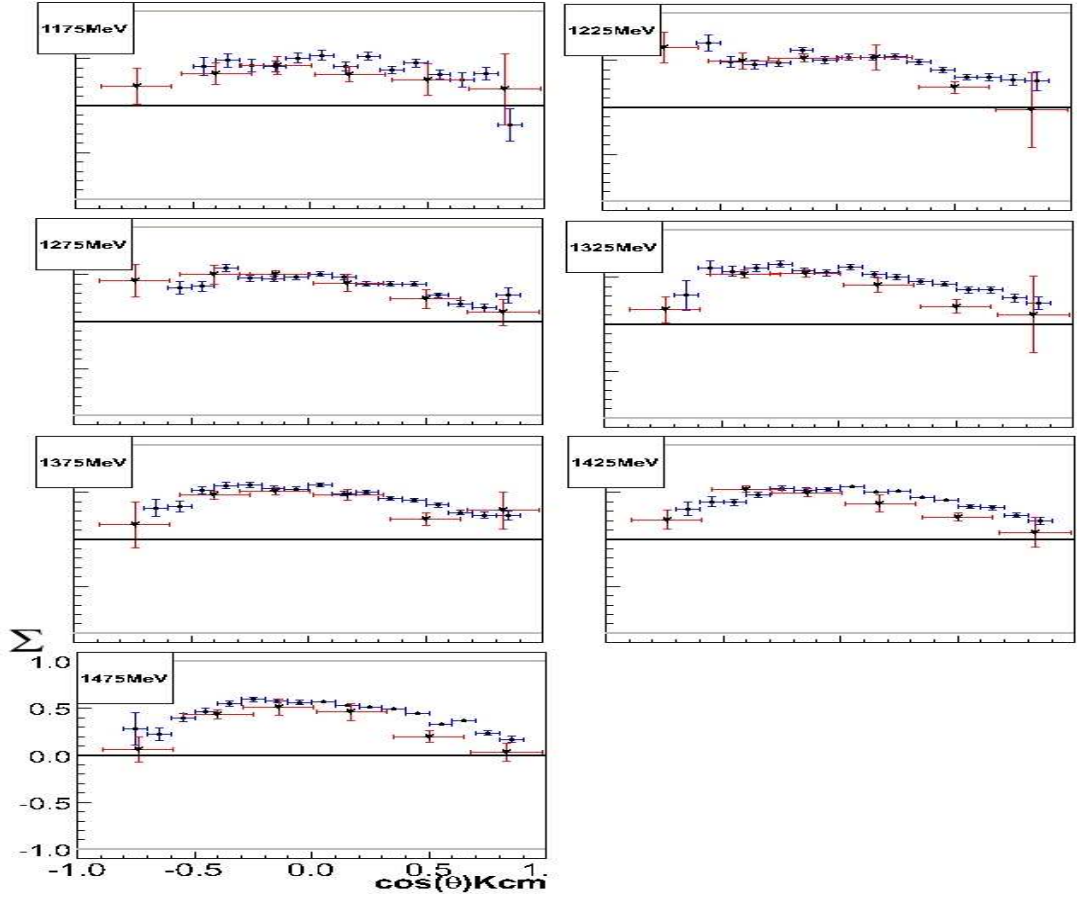


Figure 2.11: Photon asymmetries for the reaction $\gamma p \rightarrow K^+ \Sigma^0$ as a function of $\cos \theta_{cm}^{K^+}$. Comparison to GRAAL. JLab data is shown by circles with blue lines and those from GRAAL are indicated by triangles with red lines.

Given the small differences between those measurements made on the deuteron to those made on the proton (see figure 2.14) in this presented GRAAL data, it is not expected for previous proton measurements to differ greatly from deuteron measurements in similar energy or angular ranges in the current analysis. Even though the data shown here comes from η -photoproduction, the photoproduction process common to both the η and the K^+ still produces no expectation of differences between the proton and the deuteron.

2.4.3 Quasifree neutron

In 2006, the LEPS collaboration published results of beam asymmetry measurements from the $\gamma n \rightarrow K^+ \Sigma^-$ reaction channel [49]. These results they compared with the same measurements from the $\gamma p \rightarrow K^+ \Sigma^0$ channel. The experimen-

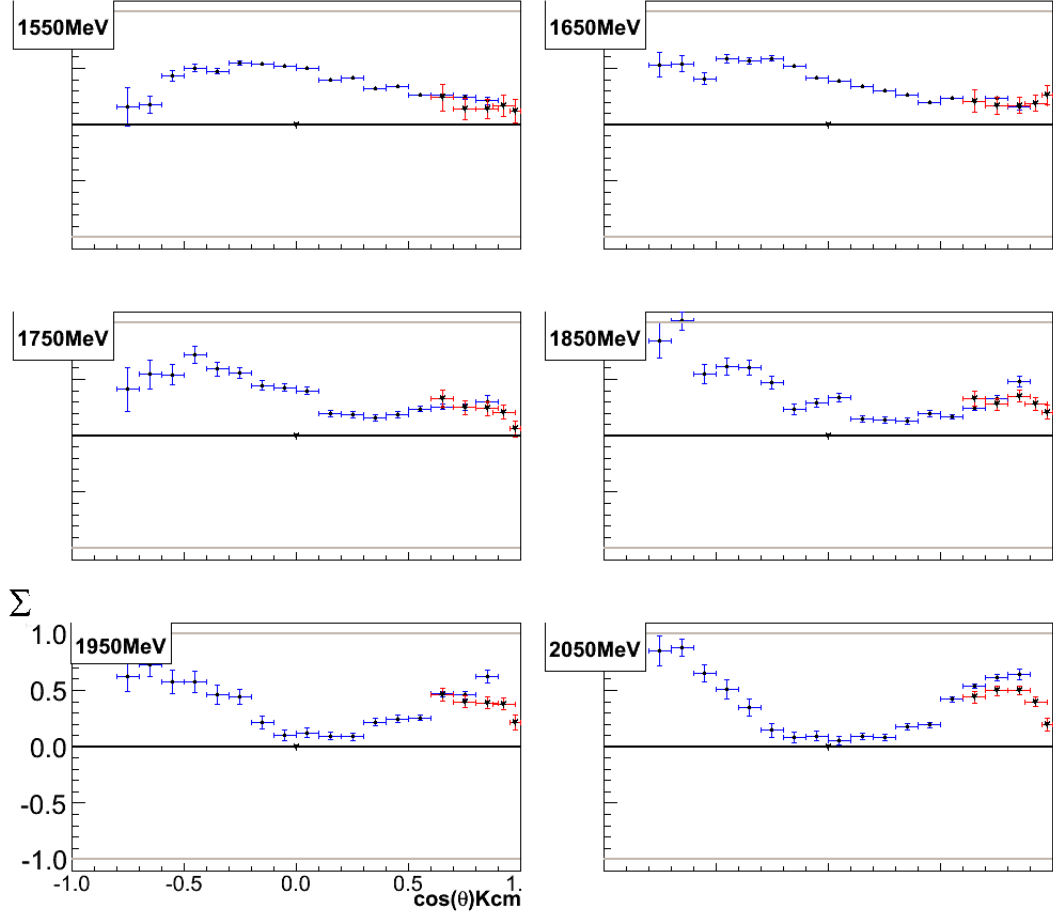


Figure 2.12: Photon asymmetries for the reaction $\gamma p \longrightarrow K^+ \Sigma^0$ as a function of $\cos \theta_{cm}^{K^+}$. Comparison to LEPS data. JLab data is shown by circles with blue lines and those from LEPS are indicated by triangles with red lines.

tal setup was the same as was described in section 2.4.1 for the LEPS photon asymmetries from the free proton.

In this analysis, the hyperon yield was extracted from the difference in the production yield ratios of $N(\Sigma)/N(\Lambda)$ in the LD₂ data and $N(\Sigma^0)/N(\Lambda)$ in the LH₂ data. The production yields of Λ , Σ^0 and Σ^- and the background under the the Σ peak were obtained by a fit to the missing mass spectrum with six free parameters. The peak shape was reproduced by the sum of two Gaussians having different widths and amplitudes and was fixed in the fit. Two free parameters were used to scale the heights of the Λ and Σ^- peaks. The peak position of Λ was a free parameter, and the Σ^0 and Σ^- peaks were placed at 0.077 and 0.082 GeV higher than the Λ peak respectively. As a result of the fit, the production yield ratio $N(\Sigma^-)/N(\Sigma^0)$ was obtained.

The beam asymmetry measurements are shown in figure 2.15. For $K^+ \Sigma^-$, the asymmetries are positive and larger than those for the $K^+ \Sigma^0$. The asymmetries

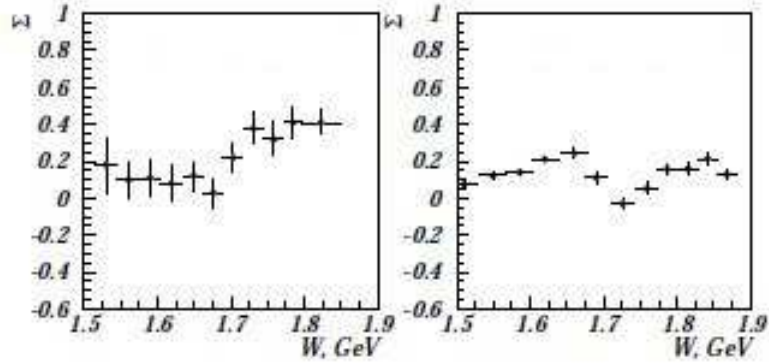


Figure 2.13: Beam asymmetry measurements for ηn (left) and ηp (right) photoproduction from 2005 GRAAL quasi-free nucleon results [48].

close to $+1$ at $\cos\theta_{cm} < 0.9$ indicated the dominance of the K^* exchange in the t -channel. the asymmetries are small at $0.9 < \cos\theta_{cm}$ because the asymmetries go to zero at $\cos\theta_{cm} = 1$. One interesting feature that was noted was that the asymmetries for $K^+\Sigma^0$ gradually increase with increasing centre-of-mass energy, while the energy dependence of the asymmetries for $K^+\Sigma^-$ is small at $W > 2.0$ GeV.

The Regge model calculations overestimated the data for the $K^+\Sigma^0$, while the calculations generally agreed very well with the data for the $K^+\Sigma^-$, particularly at higher energies. The agreement suggested that an additional contribution, not present in the calculations, is small in the $K^+\Sigma^-$ channel. It was thought that contributions from Δ^* resonances could explain the $K^+\Sigma^0$ data, but this would reduce the $K^+\Sigma^-$ asymmetries and thus not accurately reproduce the beam asymmetry data. It was speculated that the difference between theoretical and experimental asymmetries for the $K^+\Sigma^0$ was, at least in part, due to contributions from u -channel Λ and Λ^* exchanges and s -channel N^* resonances which have a much stronger coupling to γp than to γn .

2.4.4 Quasifree kaon photoproduction on nuclei

Previous to the work done at Giessen, Lee, Mart, Bennhold and others performed an investigation into the quasifree reaction $A(\gamma, KY)B$ using three different model approaches [16]. They first examined fits to previous data from SAPHIR [28, 30, 56] using two different models. The first of these fits used an older model (M1) that used a cutoff function to reproduce the required high-energy fall-off yet preserve gauge invariance, but despite the success of this approach, they found no microscopic basis for it. They used a method by Haberzettl [57–59] which allowed

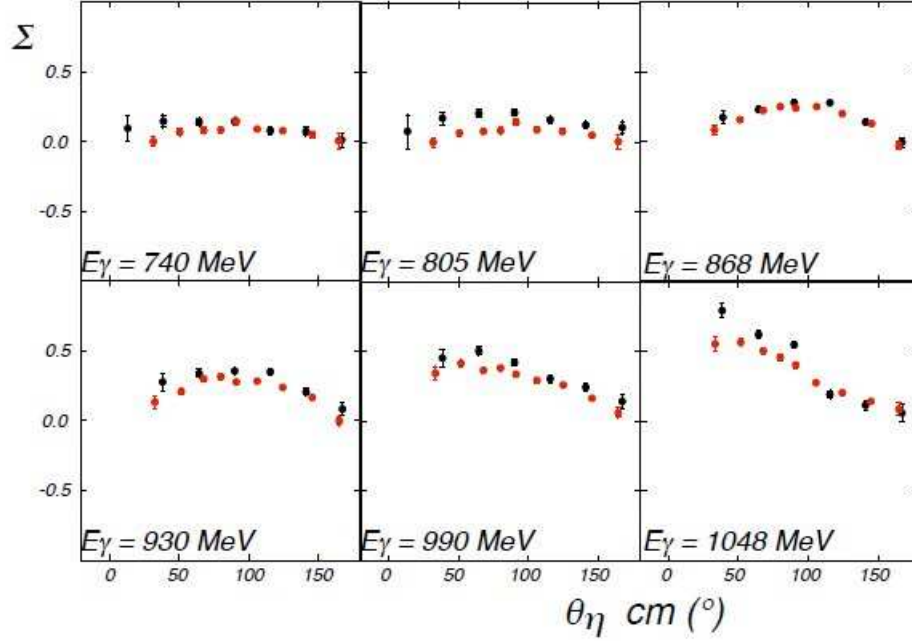


Figure 2.14: Comparison of GRAAL beam asymmetry measurements for ηp from the free (black circles) and the quasi-free (red circles) proton [55].

them to remove the cutoff term from their previous model and provided a good phenomenological description of experimental data. This then gave them the form of their second model (M2). The third model (M3) they presented in their paper used a distorted wave impulse approximation (DWIA). Using these models they examined the potential of exclusive quasifree kaon photoproduction on nuclei to reveal details of the hyperon-nucleus interaction and made detailed predictions for the coincidence cross-section and the beam asymmetry. The study served two main purposes, first, to examine the sensitivity of various observables to the hyperon-nucleus final-state interaction and secondly, to establish a kinematic range in which polarisation observables are insensitive to distortion effects.

M1 and M2 model calculations of the beam asymmetry were produced and these are shown in figure 2.16. The asymmetry was almost zero near threshold for all three channels but became sizeable at higher energies. They found large differences between M1 and M2, which led them to conclude that the beam asymmetry would be an ideal observable to distinguish between different dynamical inputs, an observation also made by the same group in other work [11].

In comparing the M1 and M2 model schemes they re-emphasised the idea that polarisation observables offered good potential for discriminating between models that use different dynamical inputs. They stated that while their updated model (M2) incorporated methods with a field-theoretical foundation, it was still

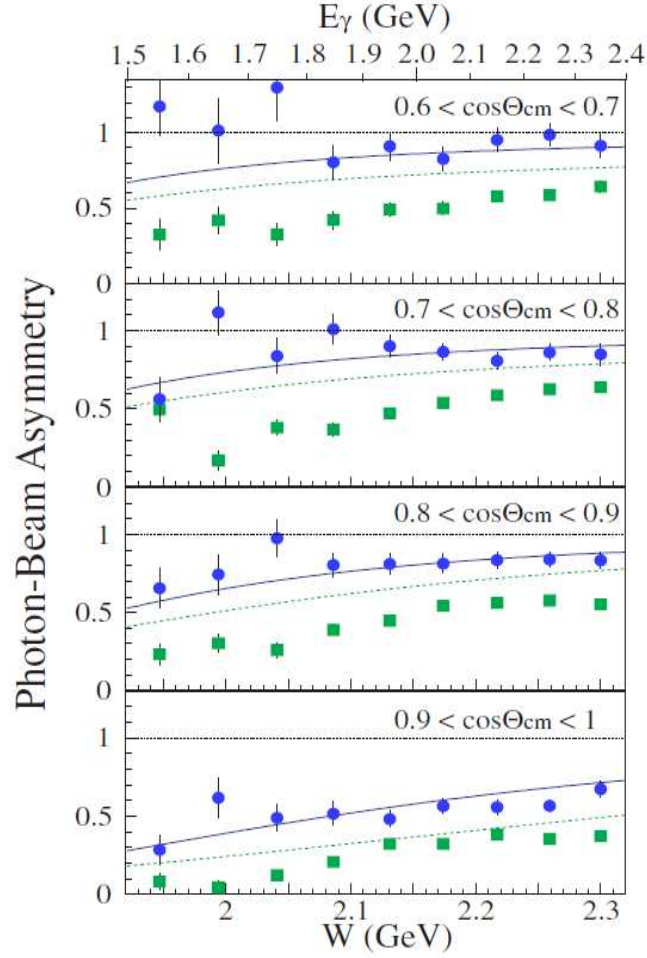


Figure 2.15: LEPS beam asymmetries for $\gamma n \rightarrow K^+\Sigma^-$ (circles) and $\gamma p \rightarrow K^+\Sigma^0$ (squares). The solid and dashed curves are the Regge model calculations for the $K^+\Sigma^-$ and the $K^+\Sigma^0$ channels, respectively.

desirable to establish justification phenomenologically also and to this end they identified polarisation observables as playing a crucial role.

DWIA model calculations

In the distorted wave impulse approximation (DWIA), a non-relativistic model (model M3) is used at intermediate energies to compensate for the effects of a mean nuclear potential. Basic scattering reaction calculations often assume that the incident particle behaves as a plane wave until it interacts with the a nucleon in the nucleus. In fact the potential field of the nucleus, which is usually given by an optical potential, distorts the nucleon wavefunction.

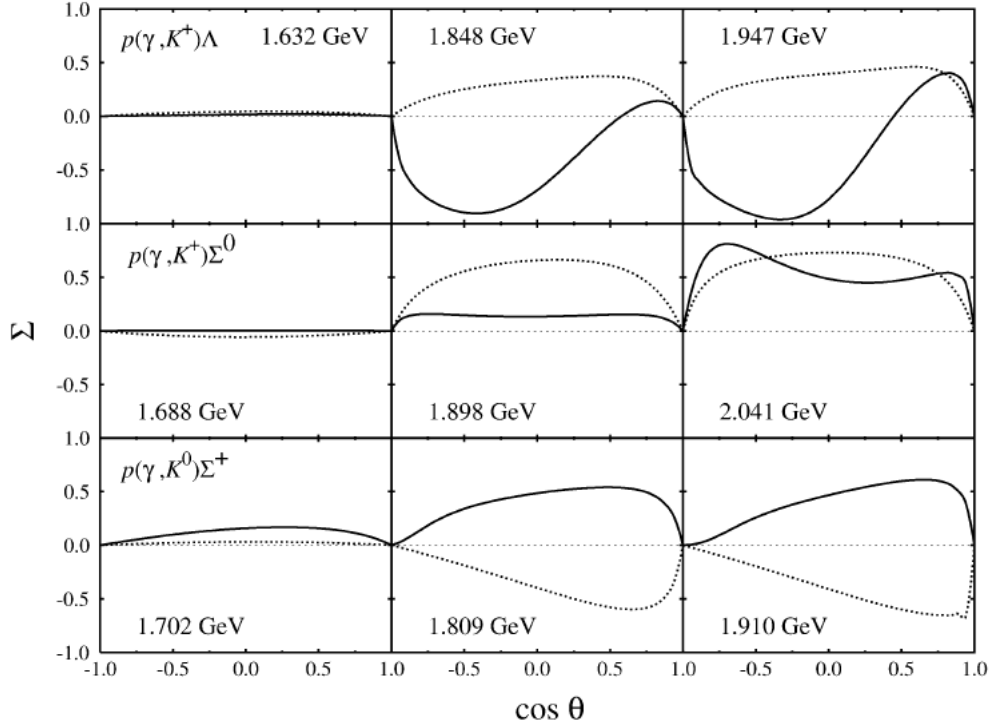


Figure 2.16: Photon asymmetry of $p(\gamma, K^+)Y$. The solid curve indicates the updated model and the dotted curve shows the older model.

Kaon-nucleus interaction

Unlike the πN interaction, the K^+N interaction is rather weak on the hadronic scale. Due to strangeness conservation, there are no hyperon resonances in the K^+N system, nor any inelastic channels, with the exception of (K^+, K^0) charge exchange on the neutron. The large medium effects due to $\pi NN \rightarrow NN$ annihilation and Δ propagation in the π -nucleus system are absent from the K^+ -nucleus scattering. As a result, the low-energy K^+N interaction can be understood through a simple background scattering with a smooth energy dependence.

To generate the distorted waves for this approach, they solved the Klein-Gordon equation using a first-order optical potential constructed from the elementary K^+N amplitudes. For K^0 , they used the same potential as for K^+ as a starting point, as little is known about the K^0 -nucleus interaction, though, in principle, the information could be obtained by measuring kaon charge exchange on nuclei. They went on to state that improved optical potentials like the one developed by [60] should be used in future studies, but felt that the potentials they used for their exploratory study were sufficient.

Hyperon-nucleus interaction

Due to insufficient data, there were very few optical potentials that could describe hyperon-nucleus scattering. For their analysis, they used the global optical model by Cooper et al. [61,62]. When their model was applied to bound nuclear systems they found it gave a reasonable description of the experimental data [63]. After this they slightly adjusted the model parameters in order to more quantitatively reproduce the data. For the Σ case, the model was also constrained by existing information from Σ^- atoms and from ΣN scattering. The distorted hyperon wavefunctions were then generated using the Schrödinger equivalent potentials.

The group presented their results in two different kinematic schemes, the quasifree and open kinematic regimes. They also limited themselves to coplanar arrangements where the hyperon was on the opposite side of the kaon ($\phi_Y = 180^\circ$).

Quasifree kinematics

The quasifree kinematics closely resembled the two-body kinematics in free space, except in the case being described the reaction was occurring on a bound nucleon with finite momentum. The quasifree kinematic scheme had the feature that the energies of the outgoing particles varied in the whole angular range, making it maximally dependent on the final-state interactions and minimally sensitive to the details of the nuclear wavefunction.

They presented calculations of the kaon angular distributions for the observables for $^{12}\text{C}(\gamma, KY)^{11}\text{B}_{\text{g.s.}}$ at $E_\gamma = 1.4$ GeV and reaction missing momentum, $p_m = 120$ MeV/c, where $\text{B}_{\text{g.s.}}$ represents the final nucleus in its ground state. Figure 2.17 shows the effects of final-state interactions. It shows four different calculations for the coincidence cross section ($d^3\sigma$), the photon asymmetry (A_γ), and the hyperon recoil polarisation (A_Y): in Plane Wave Impulse Approximation (PWIA) where plane waves were used for the outgoing kaon and hyperon, in DWIA with hyperon final-state interactions (FSI) turned off, in DWIA with kaon FSI turned off, and in full DWIA.

The results show that the angular distributions were peaked in the forward direction and that the magnitudes of the beam asymmetry and hyperon recoil polarisation were sizable and should be measureable in experiments. The PWIA results agreed qualitatively with model results from [64], with the differences being attributed to Abu-Raddad and Piekarewicz's use of an older elementary amplitude.

On its own, the kaon FSI caused small ($\sim 10\%$) reductions in the cross sections

and had little influence on the polarisation observables. With just the hyperon FSI, larger (up to 40%) reductions were seen in the cross sections for the $K\Sigma$ channels than for the $K\Lambda$ channels (up to 20%). They expected such behaviour in the cross sections however, since, by construction, the Σ potentials are stronger than the Λ ones. When the interference of both FSIs were present, the kaon and hyperon distortions appeared to combine with a degree of destructive interference in the $K\Lambda$ channels. Conversely, in the $K\Sigma$ channels, the combined FSIs constructively interfered with each other in a way producing an enhanced DWIA cross section, compared to when only the hyperon FSI was present. They concluded from this that the kaon and hyperon distortions interfered with each other in a complicated pattern, which made the extraction of the hyperon-nucleus potential more difficult. The influence of the kaon FSI was also apparent for the polarisation observables. Consequently, the net effects of the FSIs on the cross sections were comparable in all six channels. They noted that the beam asymmetry was more strongly affected by the FSIs in the $K\Sigma$ channels, particularly the $K^+\Sigma^-$, whereas it had little effect in the $K\Lambda$ channels, but that the effects may be too small to be detected experimentally as the cross sections in the regions of large effects were correspondingly small.

Open kinematics

In the open kinematical regime, p_m was allowed to vary freely. They presented their results as a function of photon energy for the same reactions.

Figure 2.18 shows the effects of FSIs under the open kinematical regime. Including both the kaon and hyperon FSIs led to a reduction (up to a factor of two) of the cross sections. They also found that in most cases, FSI significantly affected the shape of the polarisation observable distribution. This indicated that the findings in figure 2.17, that the polarisation observables were independent of the FSI, remains valid only under certain kinematical situations. The conclusions regarding the relative contributions to the FSI to the cross sections from figure 2.17 still hold true, but the role of the kaon FSI is now different as compared to the quasifree kinematics in that it constructively interferes with the hyperon FSI in almost all cases. The double peaks in the cross section of the two Λ channels are of kinematic origin; they arise from the range of values p_m , which crosses the maximum of the p -shell single-particle wavefunctions twice.

After all aspects they investigated were considered, the group found differences between the PWIA and DWIA results that indicated the importance of both kaon and hyperon final-state interactions. They found that the hyperon

FSI lowered the differential cross sections on the order of 20-40% while the polarisation observables could change by more than a factor of two. They expect that precise measurements of the quasifree kaon production process, complemented with direct scattering wherever possible, should enhance understanding of the Y-nucleus interaction in the future.

They pointed out that several ingredients for this reaction have to be known more precisely before any quantitative conclusions about the hyperon-nucleus potential can be drawn. The K^+ -nucleus interaction has been studied in great detail with sophisticated descriptions available that can reproduce K^+ -nucleus elastic scattering data. The kaon FSI, despite being relatively weak in strength, plays a nontrivial role. It can interfere with the hyperon FSI to reduce or enhance the combined FSI effects and future investigations of this reaction should include improved kaon wavefunctions.

They found a narrow kinematic window where the FSI did not affect selected polarisation observables. To access this range requires keeping close to quasifree kinematics with moderate missing momentum ($p_m < 150$ MeV/c) and photon energies below $E_\gamma < 1.4$ GeV. Within this kinematic region, the beam asymmetry turned out to be insensitive to final-state distortion for the $K\Lambda$ channels while for the $K\Sigma$ channels the hyperon recoil polarisation was found to be insensitive. They found polarisation observables that were free of distortion would provide an excellent tool for uncovering effects of the formation, propagation and decay of higher-lying N^* resonances in exclusive channels.

2.5 Summary

The field of strange meson photoproduction has undergone something of a revival in the last 15 to 20 years, and this is mainly due to the development of high luminosity, high duty-factor accelerators and large acceptance spectrometers. This renewed interest has coincided with an increased focus on resolving the issue of missing resonances, with recent quark model predictions that some of these missing states should couple more strongly to $K^+\Lambda$ and $K^+\Sigma^0$ final states [2]. Mart and Bennhold developed an isobar model in an attempt to reproduce the early cross section results from SAPHIR, and from this model it appeared there was some evidence for one of these missing states. More recent model calculations however, were able to likewise reproduce the SAPHIR results but by using a different approach to handling the non-resonant background terms that excluded any missing resonances. Both these approaches highlighted a major problem in

attempting to extract resonance information from a limited data set. Particularly, they suggest that new photon asymmetry data should be sensitive to contributions from previously missing baryon states. The possible inclusion of new states has also been suggested by further model calculations that include higher spin contributions, with all approaches indicating the need for new data to firmly confirm or deny their existence.

Another issue that has been demonstrated by recent analyses is the lack of consistency between cross section results measured at both SAPHIR and CLAS. Multipole calculations by Mart and Sulaksono show a clear dataset dependence upon which specific resonances are predicted to couple to the $K^+\Lambda$ channel. This extremely undesirable situation necessitates further measurements to be added to the world database to test the consistency of the two sets of cross section data. Beyond this, the same CLAS data set used to make the cross section measurements also gave the first evidence of a fully polarised Λ when using a circularly polarised photon. The result of this has significant ramifications for the contemporary theoretical understanding of the process of strangeness photoproduction with a model hypothesis being developed involving quark spin. The analogous results from this and other analyses involving linearly polarised photons should provide a test of this hypothesis and could potentially indicate new physics in the production of strange quarks from a photon.

The work contained here will improve the understanding of how the final observables are affected by re-scattering effects in the final state interaction. It will go on to help establish the validity of the quasifree approximation, a crucial step for KY photoproduction from neutron channels. When the results of this analysis are taken in conjunction with their theoretical interpretation they should provide some further insights into the process of strangeness photoproduction. Beyond this, when the observables from this analysis are looked at in concert with past and future CLAS analyses [12, 17, 52, 65, 66] they will be able to help construct a model independent framework of any missing states without any phase ambiguities. Ideally, this will aid the resolution of the missing resonances issue and help establish the correct degrees of freedom to be used in the resonance energy region.

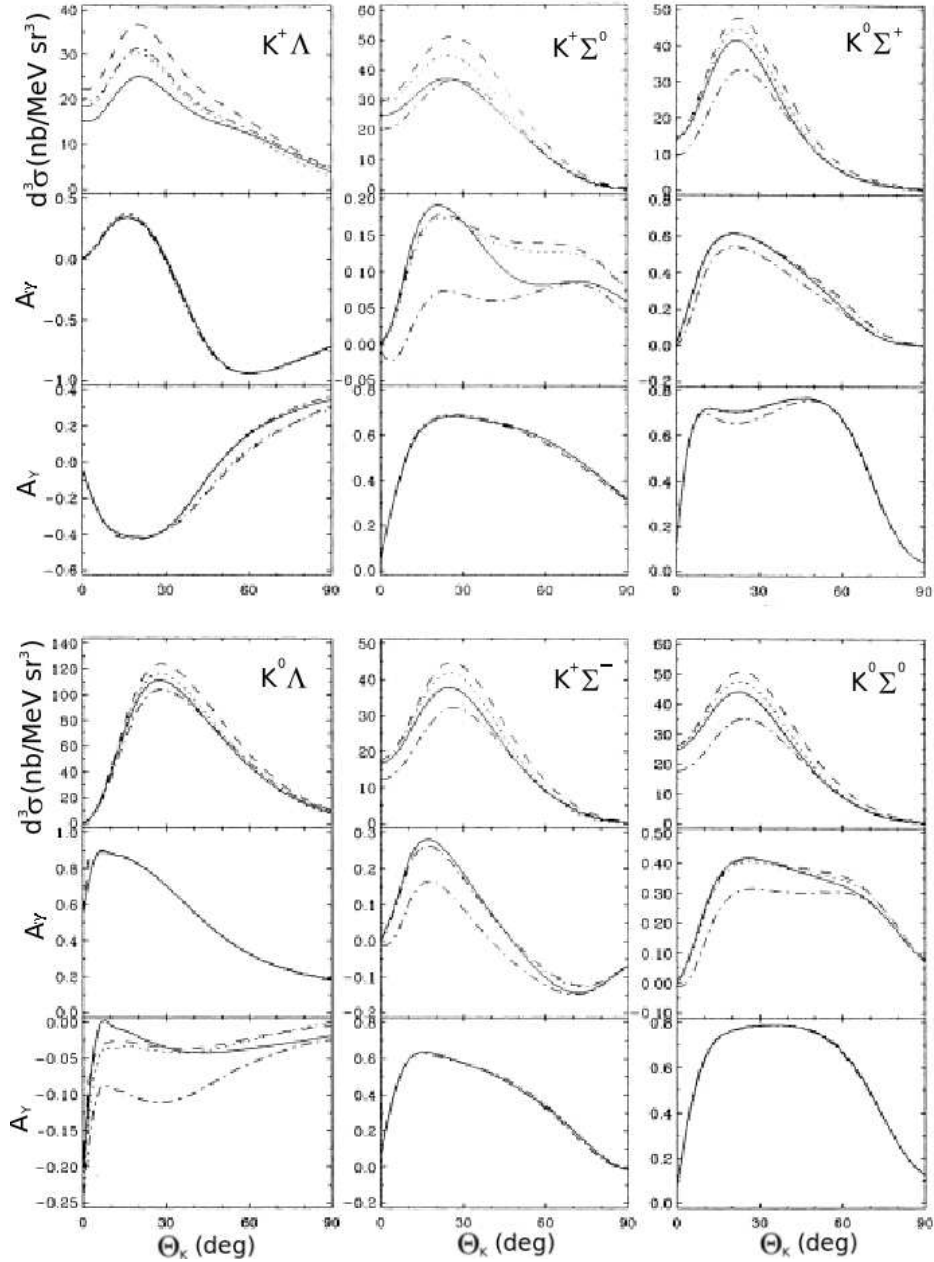


Figure 2.17: Effects of final-state interactions under quasifree kinematics for the reaction $^{12}\text{C}(\gamma, KY)^{11}\text{B}_{\text{g.s.}}$ at $E_\gamma = 1.4$ GeV and $p_m = 120$ MeV. The four curves correspond to calculations in PWIA (dashed), in DWIA with only kaon FSI (dotted), with only hyperon FSI (dash-dotted), and the full DWIA (solid). The top graph in each plot shows the cross sections, the middle graph shows the photon asymmetry (denoted by A_γ) and the bottom graph shows the hyperon recoil polarisation (denoted by A_Y).

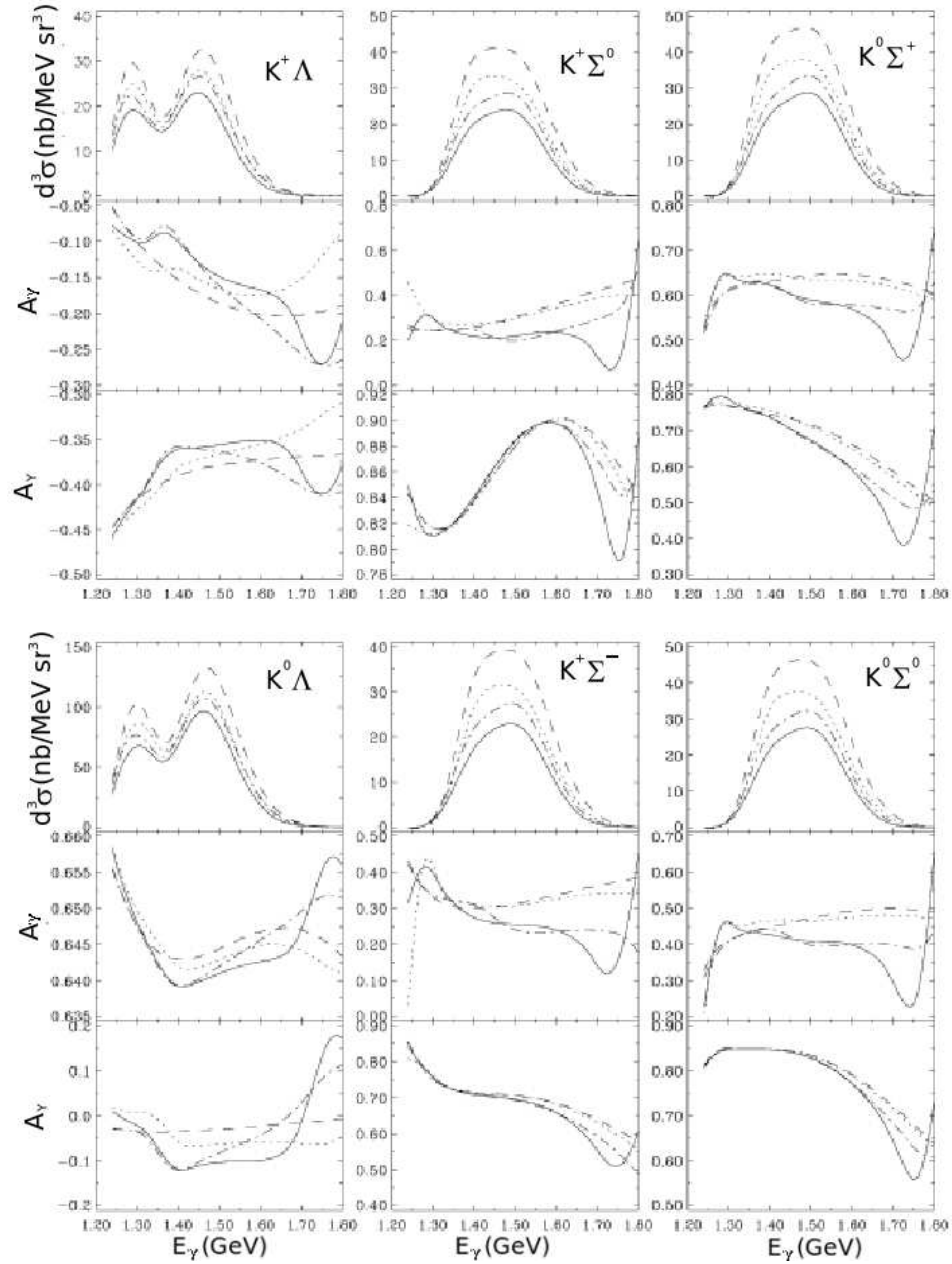


Figure 2.18: Effects of final-state interactions under open kinematics for the reaction $^{12}\text{C}(\gamma, KY)^{11}\text{B}_{\text{g.s.}}$ at $\theta_K = 30^\circ$, $\theta_Y = 35^\circ$ and recoiling kaon kinetic energy, $T_K = 450$ MeV. The four curves correspond to calculations in PWIA (dashed), in DWIA with only kaon FSI (dotted), with only hyperon FSI (dash-dotted) and the full DWIA (solid). The top graph in each plot shows the cross sections, the middle graph shows the photon asymmetry (denoted by A_γ) and the bottom graph shows the hyperon recoil polarisation (denoted by A_Y).

Chapter 3

Experimental Setup

This chapter describes the apparatus and detector components used during the g13 run period (Oct 30th 2006 to June 30th 2007) to investigate the $\vec{\gamma}D(p) \rightarrow K^+\Lambda^0$ and $\vec{\gamma}D(p) \rightarrow K^+\Sigma^0$ reactions. The g13 experiment [17] was performed at the Thomas Jefferson National Accelerator Facility (JLab) in Newport-News, Virginia, using the CLAS spectrometer and a linearly polarised tagged photon beam.

3.1 JLab, Hall-B

JLab operates an electron accelerator, CEBAF (Continuous Electron Beam Accelerator Facility) [67], which utilises superconducting RF cavities to accelerate bunches of electrons to high energies. A schematic is shown in figure 3.1. The beam from the injector is accelerated through a racetrack shaped recirculating beamline, with two linear accelerators joined by two 180° arcs with a radius of 80 m. The linacs can boost the beam energy as it is circulated in the accelerator up to five times, achieving energies in the region of 6.0 GeV. The beam, however, can be extracted at any of the complete passes with 1.2 GeV per pass. By using RF separators at the entrance to each hall it is possible to deliver so-called “beam buckets” (electron bunches) of different polarisations and currents to the three target halls simultaneously. The accelerator can offer beam currents as high as $120\mu A$ in Halls A and C whilst at the same time delivering currents as small as 1 nA to Hall-B. The operational luminosity of Hall-B is limited due to the rate capability of the CLAS detector system and the photon tagger tolerance.

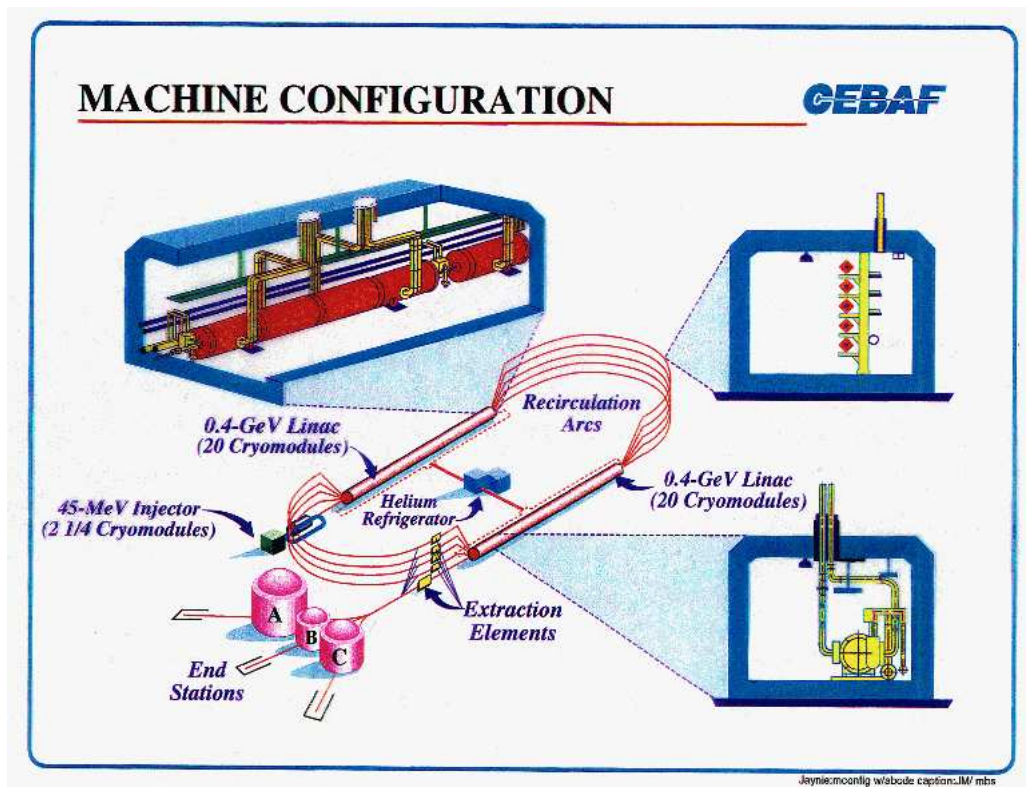


Figure 3.1: Overview of the CEBAF facility and its main components.

The g13 experiment took place in Jefferson Lab's Hall-B and used a tagged Bremsstrahlung photon beam and the CEBAF Large Acceptance Spectrometer (CLAS) which is a large acceptance ($\sim 70\%$ of 4π steradians), multi-layered, multi-sectored detector. The photon beam was linearly polarised using the Coherent Bremsstrahlung (CB) technique, and was incident on a liquid deuterium (LD_2) target and the particles resulting from the subsequent photoproduction reaction were detected in the CLAS detector. In figure 3.2 below we can see a schematic representation of experimental Hall-B showing the relative positions of the CLAS detector and the photon tagger.

The remainder of this chapter describes the various detector systems and sub-systems, along with other apparatus used in Jefferson Lab's experimental Hall-B.

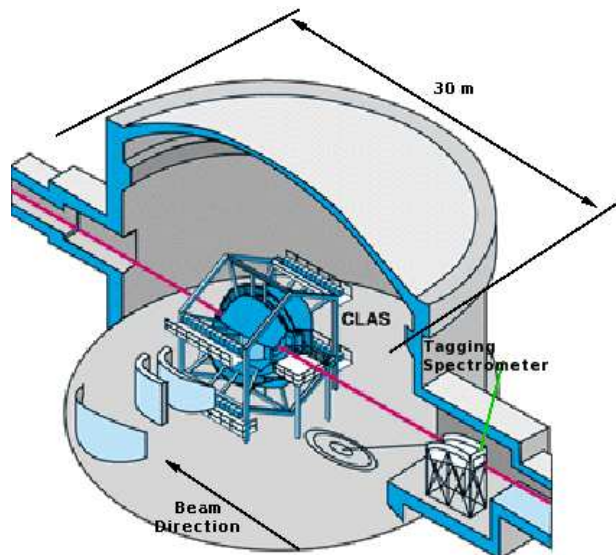


Figure 3.2: Representation of the layout of experimental Hall B showing the locations of the CLAS detector and the photon tagging spectrometer in the bottom right of the picture. The red line indicates the path travelled by the photon beam in Hall-B, where it enters from the bottom right of the diagram and is terminated by the beam dump, located in the top left of the diagram.

3.2 Coherent Bremsstrahlung Facility

The linearly polarised photon beam used in the g13 experiment was produced using the Coherent Bremsstrahlung (CB) technique, where the incident electron beam is scattered off of an appropriately oriented diamond radiator [68]. The mixed photon and electron beams then pass through the photon tagger where the photon beam continues undeflected whilst the energy degraded electrons in the electron beam are steered out of the beam using the magnet and onto the tagger hodoscope where the energy of the electron can be measured and subsequently the energy of the photon can be determined. The layout of the CB facility in Hall-B is illustrated in figure 3.4, indicating the relative positions of its main components. A brief description of the CB process is given below. A more in-depth treatment of the CB process is detailed in reference [68], while reference to its specific use at JLab can be found in references [50, 51].

In the Bremsstrahlung process an electron incident on a suitable radiator is decelerated by the electromagnetic field of the radiator's nuclei and ends up emitting an energetic photon. When an amorphous radiator such as carbon is used, then the Bremsstrahlung produced photons exhibits an energy spectrum that

falls off with increasing photon energy (see figure 3.3 top). Alternatively, if a radiator with a regular lattice structure, such as diamond, is chosen then the Bremsstrahlung photons are produced at discrete fractional energies corresponding to specific momentum transfers of the electrons in the crystal nuclei. The energy spectrum of these produced photons exhibits the characteristic coherent peak structure. If the diamond is appropriately oriented with respect to the electron beam direction then one particular reciprocal lattice vector can be isolated in the crystal radiator. Photons produced in this way then have a high degree of linear polarisation, in particular for those photons within the coherent peak (figure 3.3 middle). The diamond orientation is controlled using a goniometer which allows for finely tuned movements of the diamond to be made in all six degrees of freedom. The layout of the beamline is shown in figure 3.4 and shows all the main components of the beamline, which are: the goniometer and diamond radiator, the tagger, the collimator, the target and CLAS.

Radiator and Goniometer

The choice of radiator for the linearly polarised photon experiments is important as this determines the quality and stability of the produced photon beam. Any defects present in the crystal radiator can have adverse effects on the CB process. This is because the background production of unpolarised photons can become significant, resulting in a beam with a lower degree of relative polarisation.

The main consideration for the choice of a CB radiator is that it must have a regular crystal lattice structure as the incident electron must be scattered in a radiator whereby the recoil momentum can be taken up by the entire crystal as opposed to the individual atoms [68]. Diamond is the most common choice for a CB radiator because of its small lattice constant and relatively high Debye temperature. This high Debye temperature means that the amplitude of the thermal motion of the atoms in the lattice is small and the lattice structure is relatively unaffected by thermal effects [69].

Another important consideration when selecting a CB radiator is the thickness of the radiator as this has an effect on the angular divergence of the beam. When an electron passes through a crystal radiator there is a spread in the direction of the electrons due to multiple scattering effects, defects in the crystal lattice and divergence of the initial electron beam. This angular variation of the beam must be considered as any alteration in the orientation between the primary

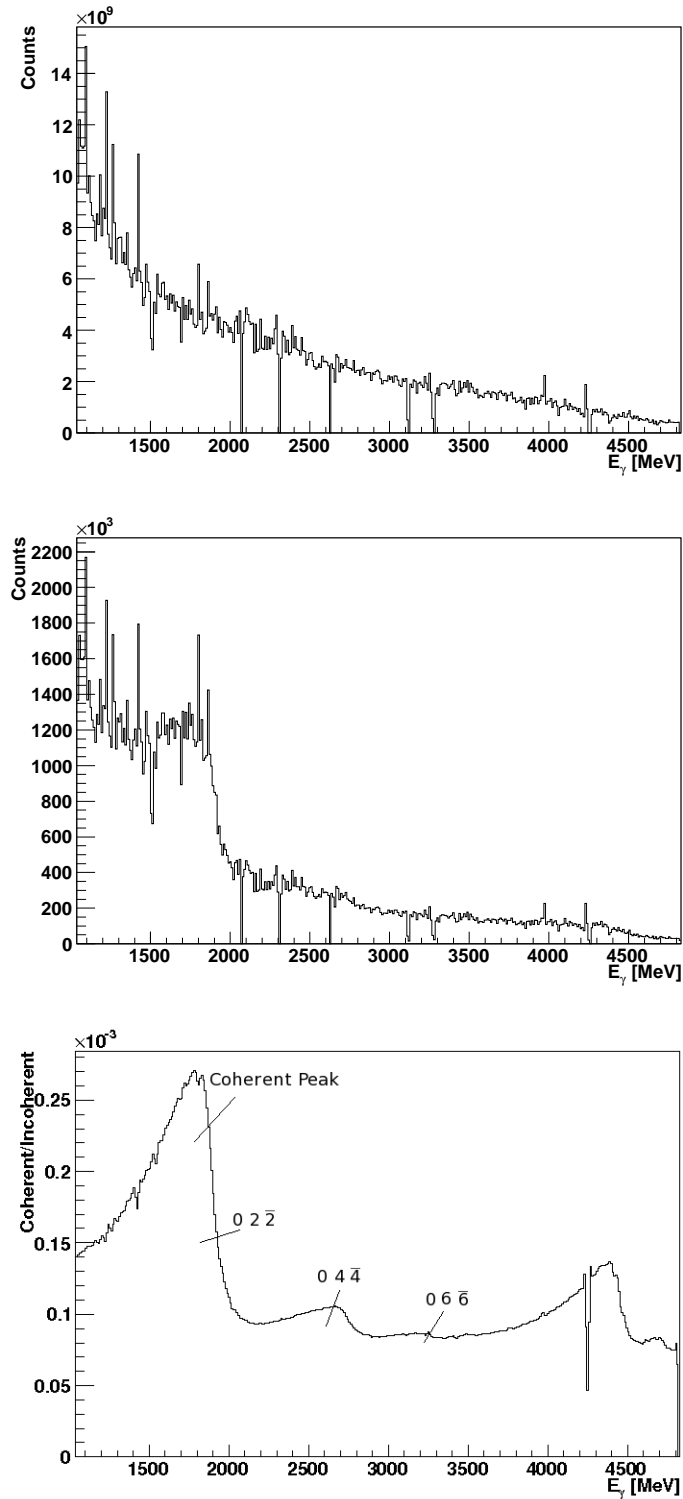


Figure 3.3: (top) Energy spectrum of Bremsstrahlung photons produced from an amorphous radiator (incoherent). The $\frac{1}{E_\gamma}$ dependence of the spectrum can be seen. (middle) Energy spectrum of Bremsstrahlung photons produced from a diamond radiator (coherent). The coherent peak structure can be seen. (bottom) Enhancement spectrum of coherent/incoherent with the different peaks and the relevant reciprocal lattice vectors they came from.

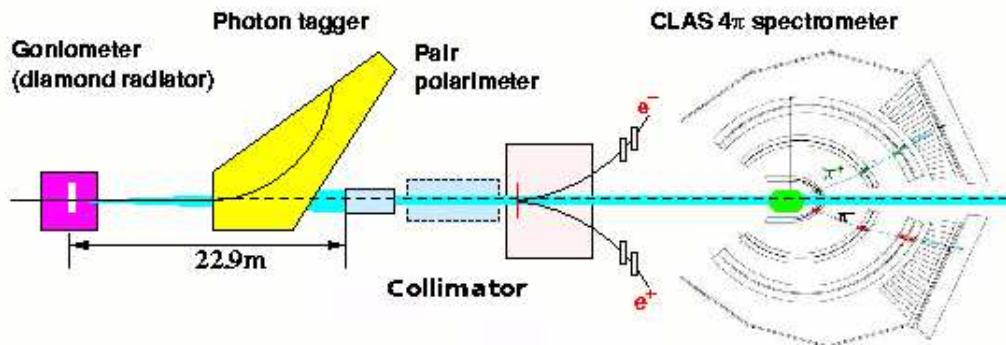


Figure 3.4: Schematic layout of the beamline in Hall B showing main features involved in the coherent Bremsstrahlung facility.

electron beam and the diamond will result in the coherent edge shifting to a different energy. This implies that an electron angular variation will result in a broadening of the coherent peak structure and hence reduce the maximum degree of polarisation [70, 71]. During g13b, a $50 \mu\text{m}$ diamond was used to produce the linearly polarised photons. The holding mount (the goniometer) for the diamond radiator is shown in figure 3.5 and the degrees of freedom are shown in figure 3.6.

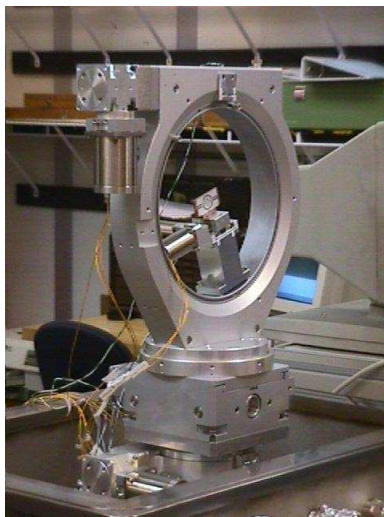


Figure 3.5: The goniometer [72] shown under test conditions with the radiator ladder visible in the centre.

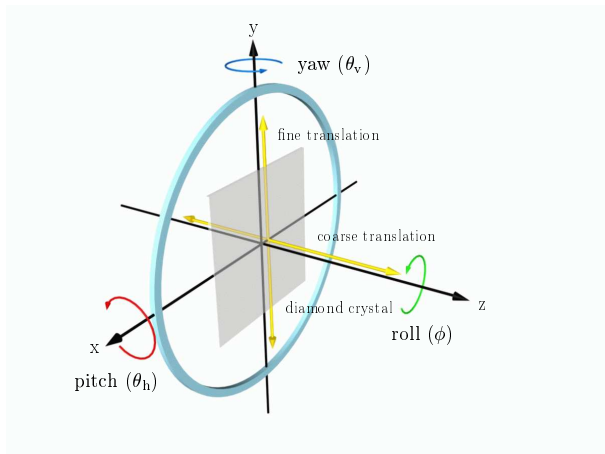


Figure 3.6: Schematic representation of the goniometer's degrees of freedom.

Photon Tagging Spectrometer

The photon tagger in Hall-B is used for tagging Bremsstrahlung produced photons over 20-95% of the incident electron energy range [73]. Bremsstrahlung radiation occurs when an incident electron is decelerated in the presence of an electromagnetic field. During this deceleration, the electron compensates for the accompanying energy change by emitting a photon with an energy equal to the energy lost by the deceleration. The electromagnetic field is produced by the nuclei in the radiator material. The concept of tagging describes the process whereby the detected energy of the degraded electron is associated with a particular photon, and the energy of the photon that was produced (and can then go on to initiate a reaction in the target) can be calculated from the following relation: $E_\gamma = E_0 - E_{e'}$ where E_0 is the energy of the incident electron beam determined by the accelerator and $E_{e'}$ is the energy of the degraded electron that was detected in the photon tagger. The tagger is crucial to determining a timing coincidence between particular photons and events and also provides a timing coincidence for the other detector subsystems.

On the exit side of the radiator there is a mixture of an electron and photon beam. The beams then arrive at the photon tagger where the photon beam passes undeviated to the target [73] and the electron beam is steered out of the beamline through the tagger via the tagging magnet. The uniform dipole field of the tagger magnetic yoke focuses the the energy degraded electrons onto the scintillator hodoscope and full energy electrons onto the tagger beam dump. The photon tagging system uses a dipole magnet that operates over a photon

energy range of 20 ~ 95% of the initial electron energy. The hodoscope has three requirements. It provides accurate momentum information for the detected electron to allow the photon energy to be determined to the required resolution. It also provides timing information that is accurate enough for coincidences to be made with any subsequent events triggered by the photon in a downstream detector. It is also important that the hodoscope provides sufficiently good timing resolution to allow the identification of the exact 2 ns beam bucket in which an event occurred. To achieve these aims, the hodoscope itself is made up of two different planes of scintillator detectors known as the timing and energy planes, (T and E-planes respectively). They are both highly segmented and have their working surfaces normal to the beam trajectory. A side view of the tagger is shown in figure 3.7.

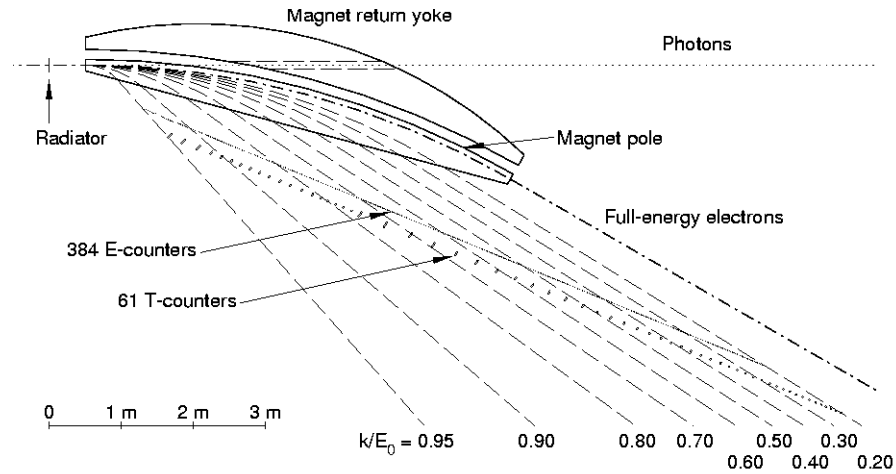


Figure 3.7: Schematic representation of the tagger, showing the relative positions of the E and T-counters. Figure from reference [73].

The hodoscope consists of 61 overlapping T-counter scintillators used for timing measurements. These are then divided into 121 T-bins including the original T-counters and the overlaps between them ($\sim 10\%$), the overlaps being used to provide a higher resolution. To be able to associate a tagged photon with the appropriate 2 ns beam bucket the T-plane resolution has to be better than 300 ps. Each scintillator is 2 cm thick and can provide a timing resolution of around 50 ps, ten times better than the 500 ps timing resolution of the E-counters. This is achieved by making them thicker than (2 cm compared to 4 mm) and situated further from the dipole magnet than the E-counters, shown in figure 3.7. The

T-paddles were also arranged in two separate groups with the first 19 paddles covering the photon energy range of 75% to 95% of the incident electron energy being narrower than the remaining 42 paddles covering the rest of the photon energy range [73]. The paddle array was built to be orthogonal to the electron trajectory so as to reduce the effects from particles that were back-scattered.

Each T-counter scintillator has two photomultiplier tubes (PMTs) and a pipeline multihit time-to-digital convertor (TDC). The multihit TDCs allow each T-counter to register many photons for each trigger. However, since most of the photons are close in energy, it can be difficult to “tag” the correct one if two or more arrive within the same beam bucket (2 ns). Such events, though, are easily identified. In order for a valid tagger event to be registered there must be a coincidence between a T-counter and its associated E-counters. T-counter signals are read out from both ends using fixed light guides and PMTs.

Similarly, there are 384 E-counters of 4 mm in thickness used for energy determination, which can be likewise divided into 767 E-bins. The overlaps in this case is on the order of one third of a paddle again being used to provide a higher resolution. The widths of each of these plastic scintillators varies between 6 and 18mm depending on position so as to produce constant momentum bins of around $0.003E_0$ and they are 20 cm long and 4 mm thick. In the hodoscope the E-plane lies above the T-plane and with the E-plane close to the exit flange of the magnet vacuum box. This minimises the effect of multiple electron scattering as they pass through the exit window and helps to optimise the resolution. The paddle array was also built to be orthogonal to the electron trajectory as it passes through the focal plane, again to reduce the effect of signals from back-scattered particles [73].

Each E-counter has only one PMT and a standard TDC. Signals from one end of the E-counters are read out via a light guide connected to an optical fibre and this optical fibre is connected to the PMT. As constant fraction discriminators are used in the tagger PMTs no time-walk correction is required.

The outputs of each of the tagger TDCs are grouped together in blocks of four. These blocks are then ORed together in a module known as the tagger master OR. This signal then goes on to form part of the CLAS trigger (see section 3.5).

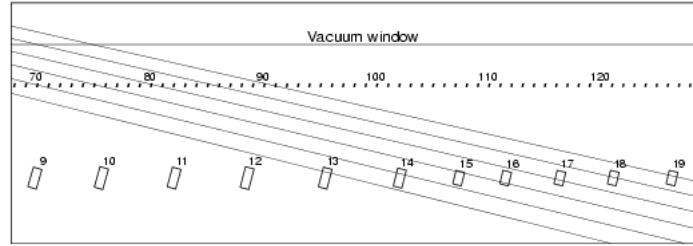


Figure 3.8: Scale drawing of a short hodoscope section. Shown is the orientation of the E and T-Plane scintillators with some typical electron trajectories superimposed. The figure shows the “venetian blind” geometry of the hodoscope. Figure from reference [73].

Active Collimator

The active collimator is located directly downstream of the photon tagging spectrometer and is shown under test conditions in figure 3.9. The collimator has an aperture of 2 mm in diameter and is located 22.9 m downstream of the diamond radiator. The device is composed of 13 nickel disks, each having an outer diameter of 50 mm and a thickness of 15 mm. Each disk has a small aperture bored through its centre and they are stacked into a cylindrical sheath of stainless steel with a 4 mm cubic scintillator sandwiched between them. This measures the rate of e^+e^- pairs produced by photons outside the 2 mm core incident on the first nickel disk. This makes online monitoring of the count rates in the scintillator possible, which can be translated into shifts in beam position. These shifts are identified as asymmetries in the measured rates from the photomultiplier tubes located at different positions around the scintillator.

The main purpose of the active collimator is to enhance the degree of linear polarisation, P_γ , within the coherent peak. As described in [68] the natural emission angle of CB decreases with increasing photon energy. For incoherent Bremsstrahlung the angular distribution is independent of the photon energy. This means that by tightly collimating the photon beam, it is possible to enhance the relative contribution of CB and thus enhance the relative degree of linear polarisation.

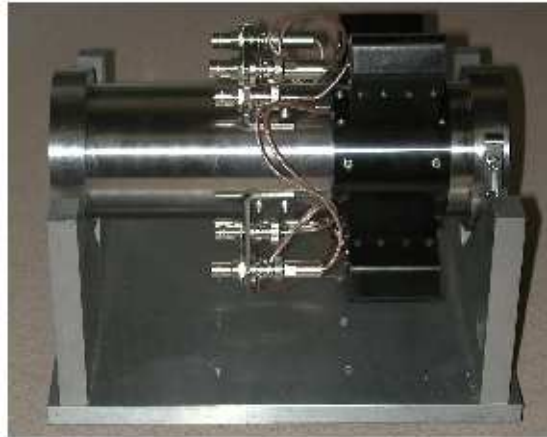


Figure 3.9: The active collimator shown under test conditions before it is installed in the beamline.

3.3 G13 target

The target for g13 consisted of a 40 cm long, undiluted LD₂ (liquid deuterium) target (6.5 g/cm²). The liquid deuterium was kept at around 10K throughout running. Liquid hydrogen was used for certain normalisation and calibration runs. The target was placed 20 cm upstream of the centre of the CLAS detector, at $Z=-20$ cm. The cell was made of Kapton and a representation of it is shown in figure 3.10.



Figure 3.10: Representation of the 40 cm long LD₂ g13 target cell.

3.4 The CEBAF Large Acceptance Spectrometer (CLAS)

The CLAS [74, 75] detector at JLab is a multi-sector and multi layered detector with an nearly full 4π solid angle coverage. It is made up of a six coil super-

conducting magnet and each layer is designed to detect different information of a particle's track through the detector, beginning when a reaction occurs in the target placed in the centre of the detector.

Starting from the detector layer nearest to the target there is the start counter, used to provide information on when exactly a reaction occurred. After this there is the first region of the drift-chambers (DC), then in the second region of the drift-chambers there is a torus magnet. This provides a toroidal magnetic field and can either bend a particle's trajectory inwards or outwards. With the third region of the drift chambers the momentum of the particle can be calculated from the arc traced out in the DC. Cerenkov counters (CC) are used for electron identification, time of flight (TOF) scintillation counters to determine particle momentum and electromagnetic calorimeters to determine particle showers. All these different subsystems in layers combine to give information on a particle's charge, momentum, mass and velocity. The toroidal field generated by the magnets focusses particles of one charge (inbending) into the beamline direction whilst those of the opposite charge are outbent onto the detector. During g13 the magnetic field had a negative polarity resulting in positively charged particles being bent inward towards the beamline while negatively charged particles were bent outward and away from the beamline [74, 76–78]. An illustration of the CLAS detector is shown in figures 3.11 and 3.12. The following sub-sections describes the various sub-systems of CLAS.

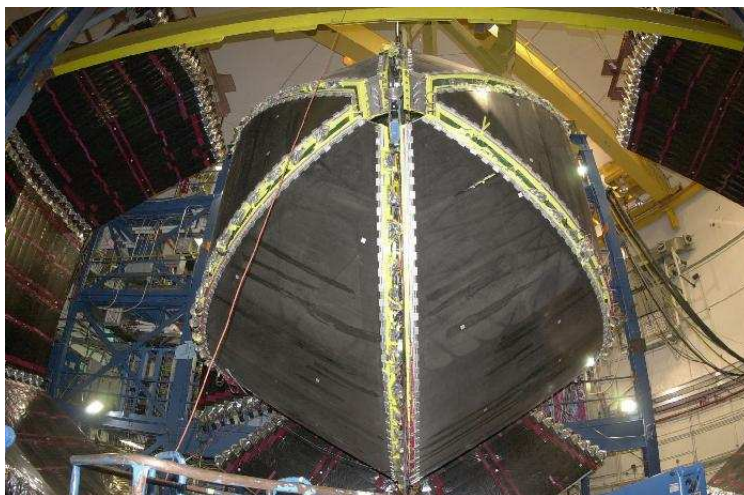


Figure 3.11: The CLAS detector in Hall B.

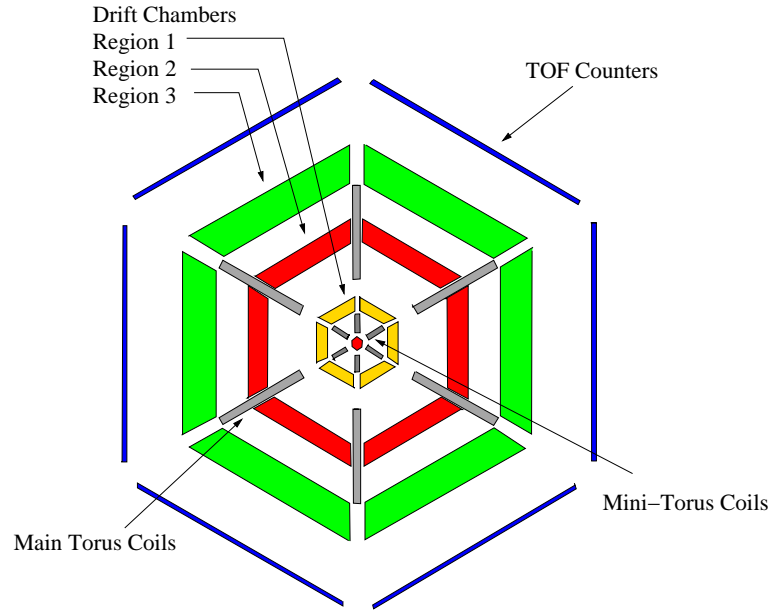


Figure 3.12: Schematic representation of the CLAS detector showing the various regions and layers present.

3.4.1 Superconducting Torus Magnet

Six superconducting coils mounted around the beamline produce the toroidal magnetic field in CLAS [74]. It is this configuration of the field coils that creates the six different sector structure of CLAS. The presence of these coils also reduces the acceptance down to $\sim 70\%$ of the full 4π solid angle coverage. These coils are mounted with 60° degree separation and the particle's momentum is always transverse to the field generated by the coils. The maximum field intensity that can be generated by the magnet is around 2 T with the main component in the azimuthal direction. Close to the coils however, the field can deviate slightly from the pure azimuthal. The circular inner shape of the coil serves to reduce such deviations and any reaction products tend not to experience any significant azimuthal kick when crossing the inner boundary of the system. The toroidal geometry also has the advantage of maintaining a field free region in the centre that can be used for the operation of a polarised target.

The magnet used to generate the field is approximately 5 m in length and 5 m in diameter. During g13 the magnet ran with a current of -1497 A, a field setting chosen to maximise the acceptance of negatively charged particles as the main channels in the g13 proposal [17] contain more negatively charged particles. This comes at the cost of losing more positively charged particles through the

beamline hole at forward angles. The coils are designed with 4 layers and 54 turns of aluminium-stabilised NbTi/Cu conductor and are cooled to temperatures of 4.5 K by forcing super-critical helium through cooling tubes located at the edge of the windings.

When experiments require electron running instead of photon running, a mini-torus can be placed around the target to prevent Møller electrons from entering region one of the drift chambers.



Figure 3.13: Picture of the bare torus coils extracted from the CLAS detector.

3.4.2 Start Counter

The start counter (SC) [79] detects charged particles from interactions in the target and produce a signal that indicates the start time of the interaction. This signal then allows us to measure the time of the hadronic interaction by correlating the signal with the correct electron beam bucket. A diagram of the sub-system is shown in figure 3.14.

The SC surrounds the target in the centre of CLAS and is constructed of six pieces of scintillator connected in a coupled paddle arrangement which provides three effective sectors of scintillator in the forward direction. There are 24 EJ-200 scintillator paddles in the device. Each coupled paddle is oriented so as to geometrically map onto two sectors of CLAS. The signal from any charged particle detected within the scintillator is read out via an acrylic light-guide connected to a photomultiplier tube (PMT). The PMT is connected in the backwards direction to give six channels that correspond to the six sectors of CLAS. The six channels have charge-to-digital and time-to-digital convertors (QDC and TDCs respectively) that provide energy and timing information of the interaction in the scintillator.

The scintillators in each paddle have a 502 mm long straight section with a tapered end called the 'nose'.

Timing resolution of ~ 290 ps for the long straight "leg" part and ~ 320 ps for the "nose" part of the SC can be achieved with calibration and the SC has the same angular coverage as that of the TOF subsystem. The timing information from the SC simplifies the identification of the RF beam bucket from which the associated reaction photon was produced. SC information combined with time-of-flight and drift chamber information is used to provide a means of particle identification.

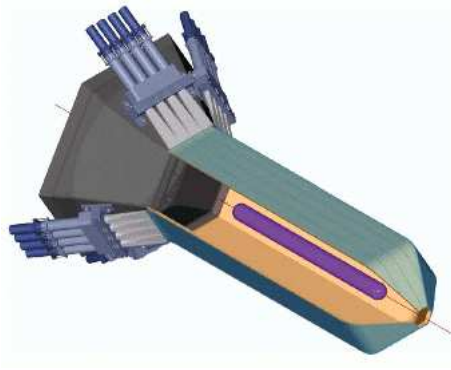


Figure 3.14: Representation of the start-counter subsystem. The target can be seen in the centre in purple.

3.4.3 Drift Chambers

The drift chambers (DC) [77, 80] in CLAS are used to detect and measure the trajectories and momenta of charged particles passing through the detector. The drift chambers are arranged in three regions and are placed between the coils of the superconducting torus. With the coils in place the DC system has around 80% azimuthal angle coverage while having a polar angular range from 8° to 142° .

Each of the three drift chamber regions is divided into six equal parts by the torus coils, ultimately leading to eighteen different sections of the drift chambers in total. The three radial locations are referred to as "regions". Each region of the drift chamber covers 60° in the azimuthal (ϕ) angle and is constructed in such a way that the curvature of the wire plane in each region is parallel to the magnetic field, providing maximum sensitivity to the track momenta. Each region of the drift chambers consists of two superlayers which themselves are comprised of six wire layers or planes. The first (or axial) superlayer is arranged axially to

the magnetic field whilst the second (or stereo) superlayer is arranged with a 6° offset in its orientation to the axial superlayer. The stereo superlayer provides the azimuthal measurement of the track trajectory. The chamber bodies support the wires running between the two endplates and the midpoints are arranged into layers of concentric circles, with the wire positions shifted by half the nominal wire spacing in successive layers [74]. The wire layers are arranged such that they produce a regular repeating pattern of hexagonal cells.

An hexagonal cell consists of one sense wire maintained at a positive voltage with six surrounding field wires maintained at a negative voltage. The diameter of these cells differ in each region of the drift chambers; region 1 cell diameter is 0.7 cm, region 2 cell diameter is 1.5 cm and region 3 cell diameter is 2.0 cm. The resolution of these different diameter cells ranges from $\sim 310 - 380 \mu\text{m}$. The DC sense wires are made from $20 \mu\text{m}$ diameter gold-plated tungsten. A small diameter was chosen as it limits wire tensions and operating voltages while the gold-plated tungsten ensures chemical inertness. Field wires are fashioned from $140 \mu\text{m}$ gold-plated aluminium alloy. Aluminium was used because of its long radiation length and therefore its ability to minimise multiple scattering. Altogether, the DC system consists of 35,148 sense wires. The drift chambers are filled with a gaseous mixture comprising 90% argon and 10% carbon dioxide.

When in operation, a potential is applied to the layers of the drift chamber. As a result, any charged particle passing through the drift chambers ionise the gas molecules and the electrons produced from this avalanche onto the positive sense wire in the cells. The particle's drift distance (and therefore position) can be determined by measuring the drift time of the electrons onto the positive sense wire. Multiple measurements of the particle's drift distance as it passes through all three regions of the drift chambers allow tracking of the particle's trajectory.

For effective tracking the individual chambers detect multiple hits for each track and automatically decide which ones represent the most likely trajectory of the particle. In region 1 (innermost layer) the particle's initial direction upon entering the drift chambers is detected whilst in region 3 its final direction when leaving the drift chambers is detected. Region 2 of the drift chambers contains the region of highest toroidal field strength in the detector and so the particle's momentum can be determined from the track curvature in this region. The trajectory of the curvature of the particle depends on its charge and the polarity of the magnetic field. The drift chambers are designed to make positional measurements of the particle track with a resolution of a few microns. This allows measurement of a particle's momentum between the range 0.2 and 2.0 GeV. This

portion of the particle detection is known as 'tracking'.

The region 2 and 3 drift chambers are shown in figure 3.15 in their installed positions along with a representation of a particle track passing through two of the superlayers.

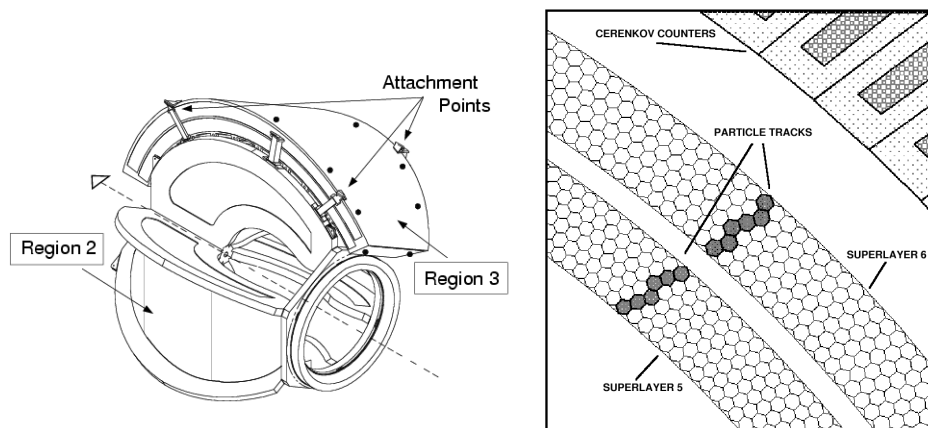


Figure 3.15: Region 2 and 3 drift chambers (left) shown in their installed positions on the torus cryostat [75]. Particle track passing through two of the drift chamber superlayers (right).

3.4.4 Time of Flight Scintillation Counters

The time of flight (TOF) subsystem [81] covers the fiducial volume of the CLAS detector. This corresponds to lab angles within the range from $8^\circ < \Theta < 142^\circ$ and in total covers an area of 206 m^2 . This active region is covered by using 57 scintillator paddles for each of the six sectors and with the last 18 paddles coupled into 9 logical pairs, resulting in a total of 48 logical counters per channel per sector. Each of the scintillators is 5.08 cm thick although their respective lengths and widths alter depending upon their actual position. The minimum length is 32 cm, found at forward lab angles ($\sim 8^\circ$) and the maximum length is 445 cm found at a lab angle of $\sim 76^\circ$. The widths vary from a minimum of 15 cm at forward angles and 22 cm at larger angles. The dimensions of the scintillator paddles in relation to its position achieves the best compromise between spatial coverage and best timing resolution. The intrinsic timing resolution for the TOF subsystem is determined using cosmic rays and for g13 it was found to be 80 ps for the short scintillators and 150 ps for the longer scintillators. The TOF system in CLAS was designed to provide good segmentation for flexible triggering and prescaling, and excellent timing resolution for particle identification. One of the

main system requirements is that it must be able to separate kaons and pions up to a momentum of 2 GeV/c.

The scintillator paddles are manufactured from Bicron BC-408 scintillator. This choice of material optimises timing resolution by allowing for a relatively fast response time with low light attenuation. A schematic representation of the TOF paddle arrangement can be seen in figure 3.16.

Each of the scintillators has a PMT attached at either end [74] and the signal is read out by both a QDC and a TDC and can be used to generate prompt signals for the CLAS level 1 trigger. For any particle travelling through the CLAS detector, the flight time of the particle from the target to the TOF subsystem is used to determine its velocity by measuring the flight time between itself and the start counter (3.4.2). This velocity, along with the momentum determined previously from the drift chambers, is used to calculate a particle's mass by using the relation $p = \gamma mv$. It is standard practice in CLAS analyses to utilise the mass calculated from the TOF subsystem in order to produce preliminary particle identification, as was done with this analysis.

For neutral particles, their identification happens with information from the electromagnetic calorimeter layer which is described in section 3.4.5. By detecting ionising radiation the TOF bars can detect charged particles. The TOF scintillation bars work by detecting the light signal given off from an atom of the scintillator material de-exciting after a particle from a target reaction has excited it. The light signal is then amplified in the PMT attached to the bar and read out by the electronics in the base. There is a proportional relationship between the intensity of the light, and therefore the size of the electronic signal eventually recorded by the base, and the amount of energy loss of the particle. Timing differences give information about the position of the particle from which a mass can be calculated.

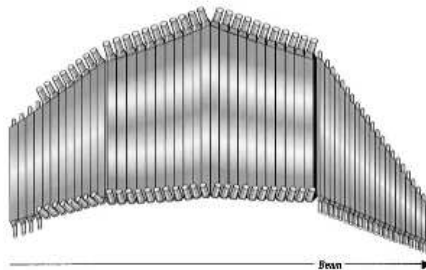


Figure 3.16: Schematic representation of one sector in the TOF paddle arrangement.

3.4.5 Electromagnetic Calorimeter

The electromagnetic calorimeter (EC) [82] is used primarily for the detection of neutral particles such as photons with energies greater than 0.2 GeV and neutrons. The EC is also able to detect electrons with energies greater than 0.5 GeV [75]. Each of the six sectors of CLAS has an electromagnetic calorimeter subsystem covering a polar angle of $8^\circ < \Theta < 45^\circ$ and consisting of thirty-nine sandwiched layers of scintillator and lead. Each layer of scintillator is 10 mm thick whilst each layer of lead is 2.2 mm thick.

The scintillator-lead sandwich construction of the EC is shown below in figure 3.17. It is apparent from the figure that each layer has the shape of an equilateral triangle, this is in order to cover the hexagonal geometry of the CLAS detector. Also apparent in the figure is the successive 120° rotation in the scintillator strip orientation of each layer (labelled here the u, v and w planes). The recurring three plane configuration produces stereo information on the position of the energy deposited in the scintillator. The calorimeter also makes use of a “projective geometry” layout, whereby the area of each successive layer increases linearly with distance from the centre of CLAS.

Particles interacting in the lead-scintillator sandwich layers lose energy by radiating a Bremsstrahlung photon (which, in turn, induces e^+ , e^- pair production and therefore more Bremsstrahlung production down to ionisation energies) typically within one radiation length and produce an energy shower. We can then identify an interacting particle based upon the energy detected in the scintillators. In order to reconstruct a valid hit in the EC, it is necessary to have energy deposition in all three views of a module. The energy and time of the hit can then be determined by measuring the path lengths from the particle hit position to the readout edge.

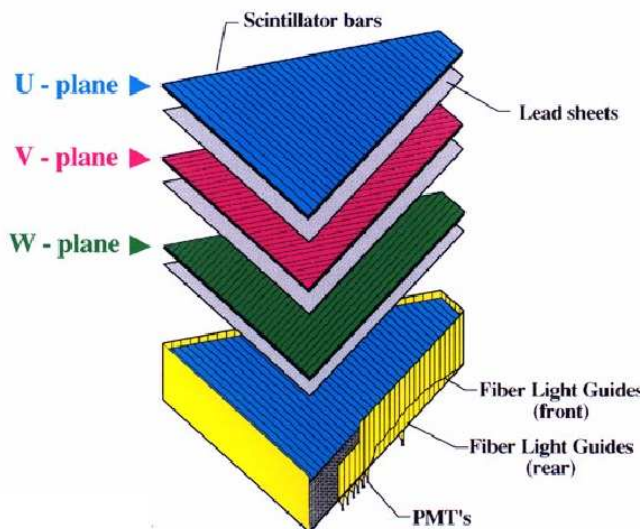


Figure 3.17: Diagram of the three differently rotated layers (each one offset by 120°) of the EC. Each layer contains 13 layers of scintillator.

3.4.6 Beam Position Monitors

The Beam Position Monitors (BPMs) are used to monitor any shift in direction of electrons and/or photons along the beamline. This is important for any experiment, such as g13, involving photon running so as to ensure that the electrons from the accelerator are correctly incident on the diamond radiator and that the photons pass through the collimators. These BPMs are positioned at three different locations on the beamline. 2C21A sits just upstream of the goniometer while 2C24A is situated just upstream of the tagger and 2H01A is just downstream of the tagger [74]. The electron beam induces a current in wires adjacent to the beamline and it is this current which is measured by the BPMs. The current varies depending on the position of the electron beam in relation to the sense wire and therefore allows the BPMs to correctly determine and record the placement of the electron beam within the beamline. The information from the BPMs is written into the data stream every 2 seconds.

3.5 Trigger and Data Acquisition System

The trigger system in CLAS uses logic signals from the various detector subsystems in CLAS to determine whether to initiate the digitisation and readout of

the QDCs and TDCs or whether to perform a fast clear/reset. The trigger configuration is set up so that it maximises the number of events of interest recorded whilst also minimising those resulting from detector noise or accidentals. The configuration of such a trigger is tailored to the conditions and needs of an individual experiment. Depending on event rates in the detectors and the system live-time the trigger can be configured to a highly specific final state configuration of particles or be left to be fairly loose triggering.

CLAS has two levels of trigger (level 1 and level 2) which pass or reject events depending on the trigger configuration. The level 1 trigger processes digital signals, via memory lookup, from the outer subsystems such as the TOF or the EC, whilst the level 2 trigger utilises tracking information from the drift chambers to perform a stricter cut on the acceptability of an individual event. The final component of the trigger is the trigger supervisor.

The level 1 trigger [83] is initiated by the logic from the start counter and is configured to make a decision based on some combination of tagger master OR, TOF and start counter logic. It then uses a lookup table to identify true charged particle tracks by matching between hits in the TOF and hits in the start counter corresponding to the same sector.

The level 2 trigger uses tracking information from the DC, looking for suitable particle tracks before declaring an event valid. The system is designed to give fast information on a physics event of interest in concert with the level 1 trigger, as well as providing a stricter constraint on which events are read out.

The trigger supervisor takes all level 1 and level 2 trigger inputs and produces all common start and stop signals, busy gates and resets required by the detector electronics.

The particular configuration for g13 was such that only level 1 was used and an event detected in a single sector would initiate the trigger.

3.5.1 Data Acquisition

After the trigger supervisor the process of data acquisition (DAQ) and converting events into an analysable format can begin. Jefferson Lab uses a system of data acquisition known as CODA [84]. The DAQ receives data from the various detector systems and this is digitised into VME and FASTBUS crates in the hall before being collected by VME readout controllers [74]. These digitised values are then tabulated in a way that each event has a unique identifier number associated with it. These data arrays, or event fragments, are then buffered and sent to an online acquisition computer. Here the event fragments are processed in the Event

Builder which collates each fragment and converts the resulting data word into BOS [85,86] format. After this the Event Transport transfers the complete event to shared memory where it can be used for online monitoring or data analysis. Figure 3.18 below shows an online reconstruction of a hadronic event from the CLAS Event Display (CED). Finally, the Event Recorder writes the event to a RAID¹ array from where it is transferred to the JLab Tape Silo via a fibre link and where it now becomes available for offline analysis.

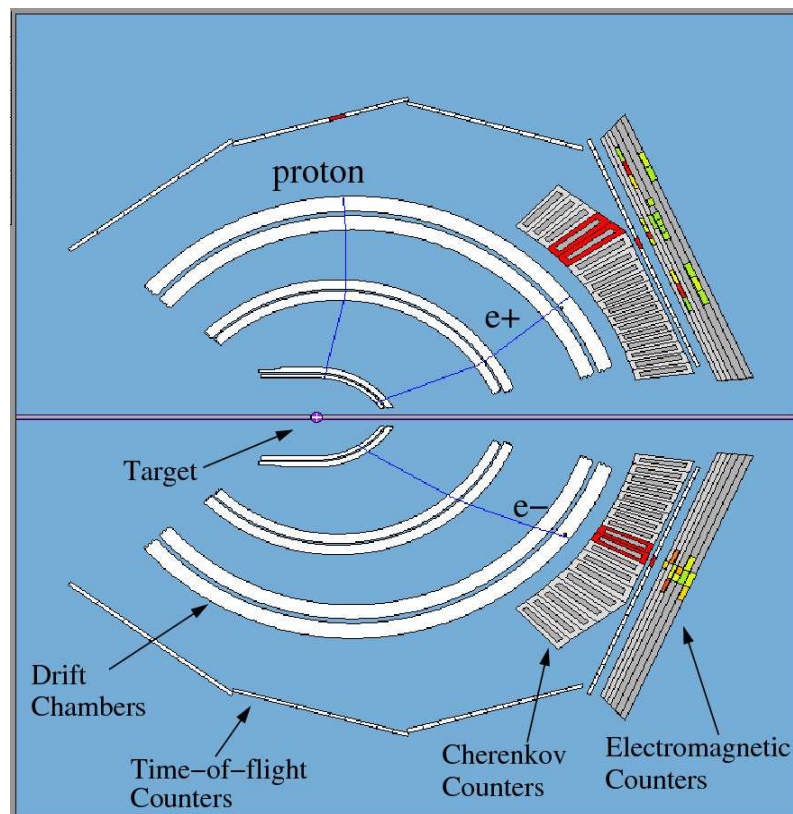


Figure 3.18: An online reconstructed hadronic event in CLAS, displayed using CED (CLAS Event Display).

The maximum event rate is 8 kHz and maintained a DAQ livetime of $\sim 85\%$.

Summary

The CEBAF accelerator uses superconducting technology to deliver a high quality and luminosity beam of electrons to three separate end stations in Jefferson Lab. These halls, with their complementary detector setups, allow a

¹RAID - Redundant Array of Independent (Inexpensive) Disks. D. A. Patterson *et al*, SIGMOD Conf. 1998

broad spectrum program to be conducted within the lab. Hall-B's coherent Bremsstrahlung facility enables a secondary beam of linearly polarised photons to be produced by scattering the initial electron beam off of a diamond radiator. Devices in the beamline such as the beam position monitors and the pair spectrometer then allow the beam quality to be monitored and enhanced throughout the running of an experiment. It is this unique setup, alongside the CLAS detector's high acceptance for charged particles that makes Jefferson Lab's Hall-B the ideal facility to investigate spin observables in strangeness photoproduction.

This chapter detailed the experimental apparatus and setup used during the g13 experiment at Jefferson Lab's Hall-B. Before any analysis can be undertaken however, it is necessary to calibrate the various detector subsystems just described in the previous sections in order to convert the output into a meaningful physical format (e.g. time, position, momentum). The next chapter describes the process of calibrating the subsystems and the data reconstruction.

Chapter 4

Data Processing and Calibrations

In order to perform physics analysis of the experimental data acquired during the run period, it is necessary to convert the raw signal information from the detector subsystems into meaningful physical values. These physical values come in the form of timing, position, energy and momentum of the detected particles. The first stage of this conversion process is done by undertaking two tasks in parallel. One task being the data reconstruction, also known as *cooking*, and the second is to calibration of the individual detector subsystems. Each detector subsystem has an offline software package designed to produce calibration constants which used by the *cooking* process. Many iterations of these parallel tasks are required in order to refine the data into the final form necessary for physics analysis.

4.1 Run Conditions and Data

Table 4.1 shows a summary of the run conditions for the g13 experiment.

| Running Condition | Linear Polarisation |
|----------------------------|-----------------------------------|
| Torus Current | -1500 A |
| Trigger | two-sector, no tagger |
| Beam Current | ~ 10 nA |
| Tagged Photon Energy Range | 1.1 – 2.3 GeV |
| Radiator | diamond (50 μ m) |
| Target | LD_2 and LH_2 |
| Target Length and Diameter | 40 cm and 40 mm (max diameter) |
| Target Position | 20 cm upstream of CLAS centre |

Table 4.1: G13 running conditions.

G13 used different electron beam energies to produce different energies of polarised photon beam ($= 1.1 > 2.3$ GeV, in steps of 200 MeV). This meant that different electron beam energies (and thus polarisations) could have contributed to the same coherent peak setting. This then required the calculation of a weighted mean polarisation of each coherent peak and polarisation plane setting. The polarisation plane depends on the diamond orientation in the goniometer and is defined to be either parallel (PARA) or perpendicular (PERP). The PARA or PERP refers to the orientation of the Bremsstrahlung photon's electric field vector with respect to the horizontal. Where an amorphous radiator was used the polarisation plane is defined as AMO (for amorphous). The polarisation plane was altered between PARA and PERP after every run and AMO was only used during certain special runs.

Given the running conditions above, ~ 120 TB of data were collected, satisfying the required targets given in the proposal [17]. The data are summarised in table 4.2 for production on the LD_2 target.

| | | Triggers | | Mean Pol. | |
|---------------------|------------------|-------------------|-------------------|-----------|------|
| E_e (GeV) | E_γ (GeV) | PARA | PERP | PARA | PERP |
| 3.302, 3.914, 4.192 | 1.3 | 3.7×10^8 | 4.3×10^8 | 0.75 | 0.71 |
| 4.065, 4.475 | 1.5 | 1.9×10^9 | 1.7×10^9 | 0.70 | 0.74 |
| 4.065, 4.748 | 1.7 | 2.2×10^9 | 1.8×10^9 | 0.71 | 0.73 |
| 5.057 | 1.9 | 3.6×10^9 | 2.7×10^9 | 0.74 | 0.78 |
| 5.057, 5.157 | 2.1 | 3.0×10^9 | 2.6×10^9 | 0.70 | 0.70 |
| 5.157 | 2.3 | 2.8×10^9 | 2.9×10^9 | 0.71 | 0.71 |

Table 4.2: Electron beam and photon beam settings with total triggers for each polarisation plane setting and mean polarisations.

4.2 CLAS Data Output

Output (see section 3.5.1) from the CLAS detector subsystems is transferred and collated on an event-by-event basis within a dynamic memory structure known as BOS (Bank Operating System) [85, 86]. Each detector subsystem within CLAS has at least one BOS bank containing the relevant raw output. These banks are then accessed using the appropriate function calls when required for calibration or *cooking*. Typically, the output of each data run is split into files of ~ 2 GB in size, and one standard data run (~ 2 hours for g13) gave rise to $\sim 50 - 60$ data

files. During uninterrupted production running it was possible to take $\sim 10 - 12$ runs per day.

4.3 Data Reconstruction / *Cooking*

The process of data reconstruction or *cooking* [87], converts the raw BOS bank outputs (see section 3.5.1) into reconstructed or *cooked* BOS banks. A *cooked* BOS bank is a collection of data words containing detector subsystem which is now in physical format (e.g. position, time, momentum). This process utilises a software package called RECSIS (REConstruction and analySIS package). The raw data are first calibrated appropriately, depending upon the detector subsystem, resulting in a set of calibration constants. Each of these constants is stored in a centralised MySQL [88] database and linked to RECSIS via an experiment-specific run index. Once a set of calibration constants is deemed to be adequate they are then used to adjust the reconstructed physical information in the BOS banks and one iteration of the data *cooking* is complete. This adjustment of the bank information accounts for factors such as detector position, trigger times and offsets of each detector subsystem with respect to the others.

For the g13 experiment there were two overall passes of the *cooking*, each consisting of multiple versions, before the calibration constants were finally decided to be of high enough quality for physics analysis. Pass refers to the current iteration of the overall process, while version refers to the current status of the calibrations. Data processing in this fashion is very computationally intensive and took ~ 12 months of constant running on the JLab computing farm with ~ 20000 raw input and ~ 80000 subsequent output files.

4.3.1 Quality Monitoring

One vital component of the data reconstruction process is the monitoring of the subsequent outputs. During g13 a package called CSQL [89] was implemented, which allows for the storage and visual monitoring of the *cooking* process results via a web interface. The package was linked to RECSIS and during processing, various outputs of interest were monitored over whole versions. As a result, data runs requiring further refinement could be easily identified. One example of a CSQL monitoring plot, showing the number of reconstructed K^+ and K^- particles per event, can be seen in figure 4.1 below. The main purpose of the monitoring process is to check for any drift of calibration constants, and illuminate any other detector problems throughout the experimental run.

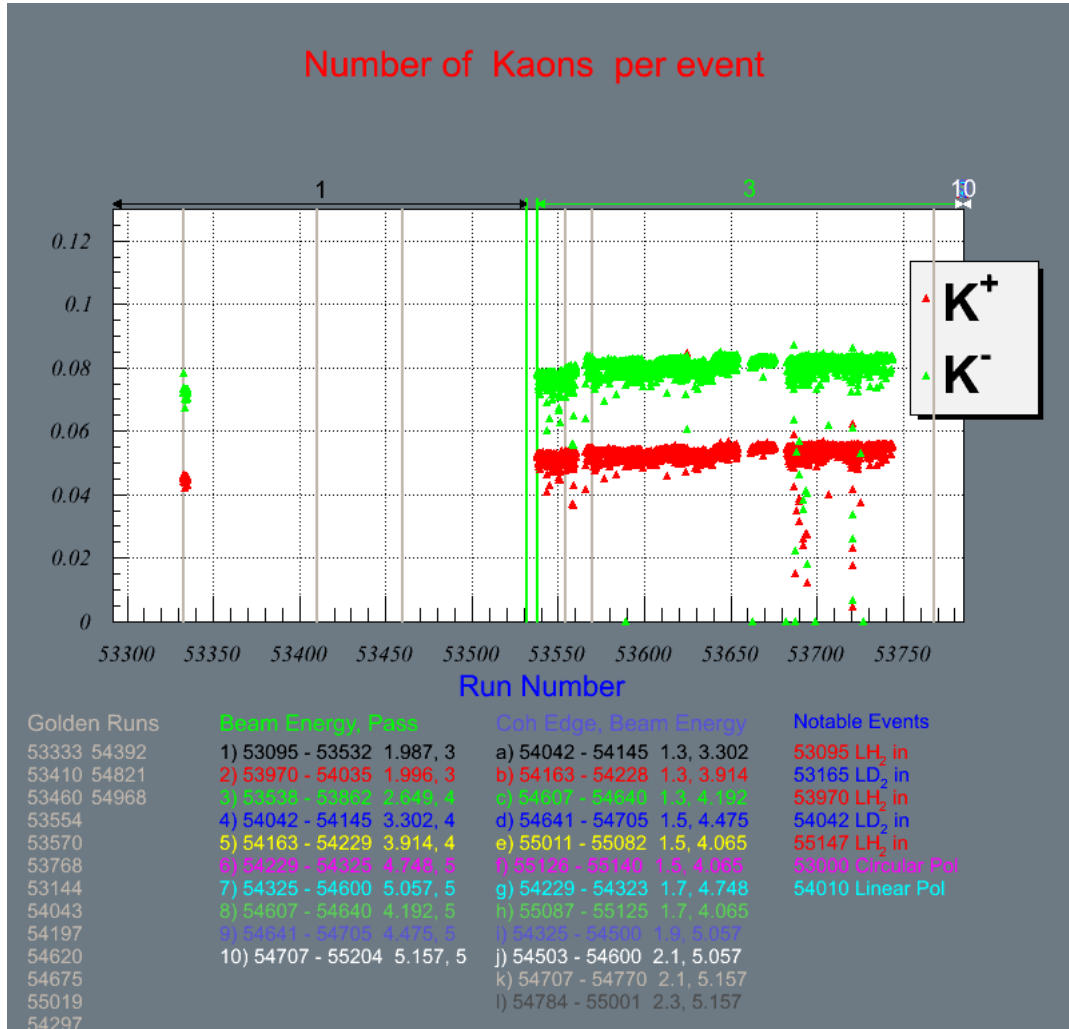


Figure 4.1: An example of a CSQL monitoring plot from g13 cooking. The plot shows how many K^+ and K^- particles we were getting, per event and as can be seen, we are reconstructing $\sim 4\%$ K^+ and $\sim 8\%$ K^- particles per event. The physical interpretation of this is that out of our overall data set, $\sim 4\%$ are events involving a K^+ and $\sim 8\%$ are events involving a K^- . Particles may be mis-identified at this point though but this is be accounted for at later stages of the analysis.

4.4 Subsystem Calibrations

Timing calibrations are of particular importance with CLAS, since timing is the basis for all particle identification (PID) and the determination of particle momenta. Further to this, the determination of the correct beam bucket, from timing, is necessary to correctly identify the event photon. In this section brief overviews of the calibration principles and methods for each of these subsystems is presented. More detail is given in relation to the calibration of the photon tagger, for which the author was responsible.

The overall calibration procedure has the following steps:

1. Calibration of the start counter and alignment to the time of flight (TOF) from scintillator paddles.
2. Calibration of the photon tagger, the beam RF time and alignment to the TOF.
3. Calibration of the TOF.
4. Calibration of the drift chambers.
5. Calibration of the electromagnetic calorimeters with respect to the TOF.

These steps are repeated many times until satisfactory calibration constants are converged upon and physics data reconstructed. In order to ensure these constants are satisfactory over the entire experimental run range, calibrations are conducted on reference runs which are chosen at regular intervals spanning the entire run range. Given the necessity for high quality particle identification and accuracy of reconstructed masses, both invariant and missing, these reference runs are taken frequently.

4.4.1 Start Counter Calibration

The calibration of the start counter (see section 3.4.2) is performed in two stages, followed by the alignment of the start counter time to the time of flight subsystem. The first stage of the calibration process involves internally aligning each pair of coupled paddle scintillators, whilst the second stage aligns the three pairs with respect to each other.

When a hit is registered in a pair of coupled paddles, two TDC timings result (T_1 and T_2). For real physical events, the time difference between these two timings should be a constant. These real events are then selected and the time

difference ($T_1 - T_2$) distribution is plotted. By then adjusting a constant associated with each paddle, the time difference can be centred on zero. This internal alignment procedure is carried out for all three coupled paddle scintillator pairs.

The next stage requires alignment of the now internally aligned paddle pair with respect to each other. In order for this to be done, an external reference time is required with which to compare the start counter time of each paddle pair. This external reference time is provided by a tagger T-counter, and so for each coupled paddle pair the start counter time is subtracted from the T-counter time. Again at this point, the constants for each coupled paddle pair are adjusted (but now by the same amount) so as to align the the main peak of this time difference distribution with the main peaks of the distributions from the other pairs. This timing difference alignment however, need not be centred on zero as this is simply an internal calibration of the start counter subsystem and is accounted for in the photon tagger time and time of flight calibrations. Once all three pairs have been calibrated in this fashion, the start counter is considered to be calibrated. Calibration plots for the start counter are shown in figure 4.2.

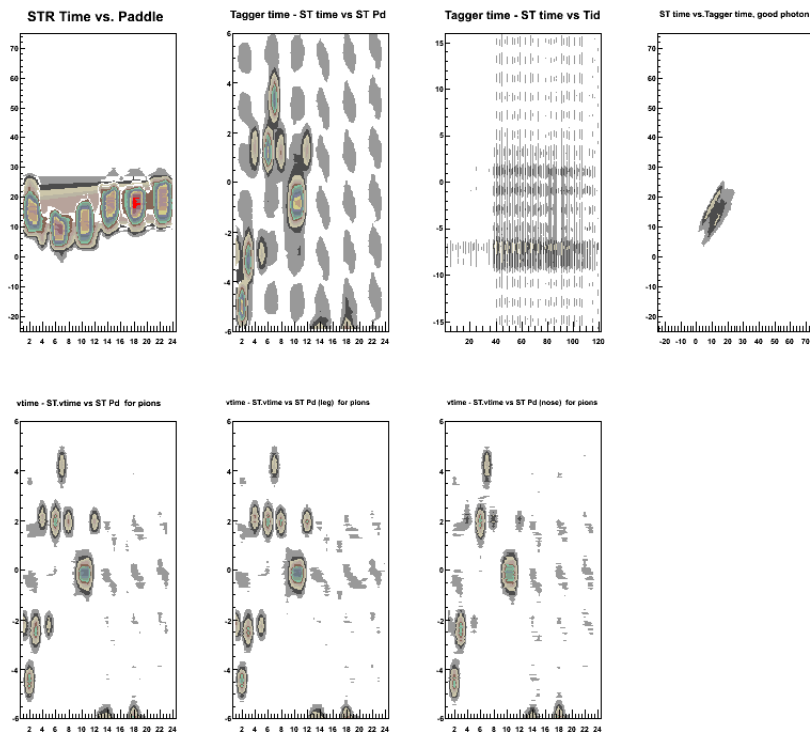
The final stage in the calibration of the start counter is to determine a constant time offset, known as $st2tof$. As was discussed in sections 3.4.2 and 3.4.4, it is necessary to align the start counter time with the time of flight subsystem in order to obtain accurate time of flight measurements, since the start counter provides the event start time. Aligning of the start counter to the time of flight is achieved by subtracting the vertex time of a track as measured by time of flight, from the vertex time of the track as measured by the start counter, and aligning the resulting distribution's offset to be aligned on zero. The final evaluation of $st2tof$ cannot be done until both the drift chamber and time of flight calibrations are completed. Consequently, the $st2tof$ value changes after each iteration of the overall calibration procedure as was previously described (see section 4.4).

4.4.2 Photon Tagger Calibration / Beam RF

Calibration procedures for the photon tagger (see section 3.2) and beam RF are detailed in Refs. [73, 90]. This section contains a brief description of the tagger calibration process, along with some representative plots of the calibration for the g13 experiment.

The concept of the photon tagger calibration can be described as follows. The TDC values from the E-counter and T-counter PMTs are required to be converted into times. This is done by calculating and storing some calibration constants ($ps/channel$) for each TDC. These values are then used to convert the

Start Counter Histograms (2)



Start Counter Histograms (2)

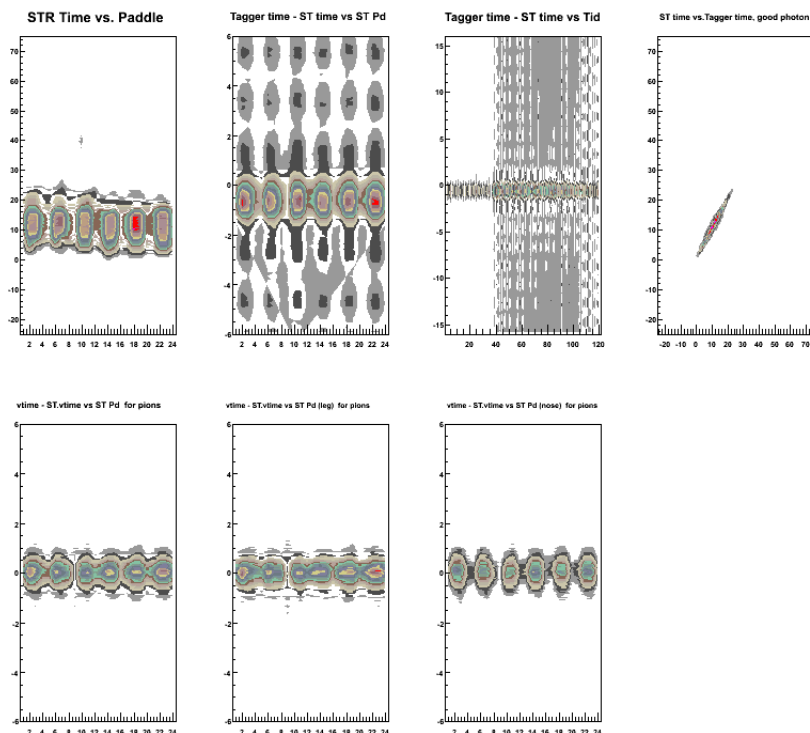


Figure 4.2: Start counter calibration plots showing before calibration (top) and after (bottom).

TDC channels into times. Once these times have been determined, geometrical matching between E-counter hits and T-counter hits is performed. This matching is only performed if the E-counter and T-counter hits represent a certain combination, based on the overlap of the E and T focal planes in relation to typical electron trajectories, as shown in figure 4.3. This combination must be one in which the electron did not scatter after interacting with the radiator foil. At this same stage of geometrical matching, a timing coincidence between the E-counter hit and T-counter hit is also required. Determination of the final timing involves using the T-counters, which are individually corrected for offsets, to identify the 2 ns beam bucket. Finer (< 2 ns) corrections to this timing are achieved using the RF machine time. The remainder of this section details the procedures involved in this calibration.

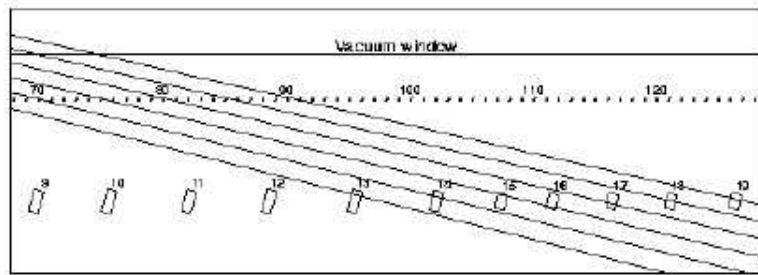


Figure 4.3: Schematic representation of a portion of the tagger hodoscope. The orientation of the counters in both the E and T planes can be seen, as can the overlap of the E-counters and T-counters relative to the electron trajectories.

The tagger calibration process can be broken down into several discrete stages, each of which produce calibration constants for use in the reconstruction/*cooking* process.

1. T-counter TDC Left-Right slope calibrations.
2. Base peak calibrations.
3. RF timing adjustments, C'_i s.
4. Tagger to time of flight offset.

Once the tagger has been calibrated, an output bank called TAGR is produced in the *cooking* output. This bank contains time, energy and T and E-counter information. It should be pointed out that in order for a tagger event to be properly reconstructed, E-T coincidences are matched using a lookup table. This E-T coincidence is required, via hardware, to be within 20 ns. The bottom left

Tagger Histograms

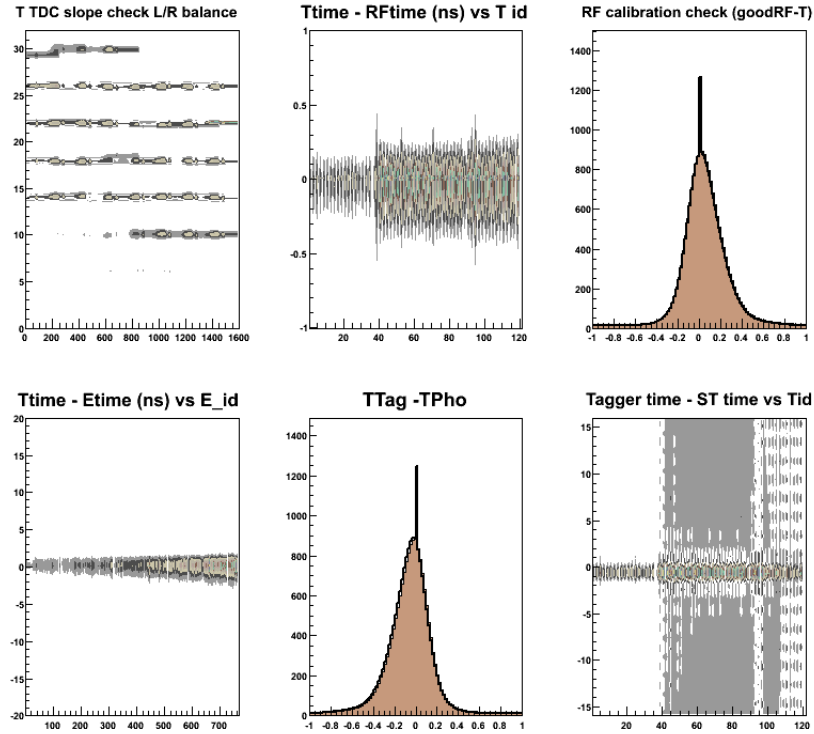


Figure 4.4: Tagger calibration output plots for a well calibrated run. (Top left) LR balance alignment, (top middle) tagger t-counter time minus RF time versus T-counter, (top right) RF calibration check, (bottom left) tagger t-counter time minus e-counter time versus E-counter, (bottom middle) tagger time minus RF corrected tagger time and (bottom right) tagger time minus start counter time versus T-counter.

plot of figure 4.4 shows this coincidence, T-counter time minus E-counter time versus E-counter number (E-id). When a hit falls within this coincidence window, the timing of the photon is determined by the T-counter time and the RF.

At this point one can look at the RF offset calibration. The machine RF time is measured via a PMT placed at the entrance to Hall B. The TDC signal resulting from this (RF TDC time) is pre-scaled by a factor of 40 resulting in a signal with a period of 80 ns. An optimum RF calibration should have the time difference between the tagger time, TTAG, for all 121 T-counters, minus the RF corrected tagger time (TPHO) equal to zero. In the bottom middle of figure 4.4 we can see this difference plotted after the calibration process. Each stage of this process is detailed in the following subsections.

T-counter TDC Left-Right Slope Calibration

The timings from the left and right TDCs from each T-counter need to be corrected. To do this we compare the the time calculated by both TDCs and then correct them relative to each other and the RF, on a counter by counter basis. The calibration software for the photon tagger measures and plots two slopes, β_{LR} and β_{RF} , from which the correction can be determined. These slopes are defined below:

β_{LR} is the slope of $\frac{\langle t_L - t_R \rangle}{2}$ versus t_{mean}

β_{RF} is the slope of $t_{mean} - t_{eb}$ versus t_{mean}

where t_L and t_R are the measured left and right TDC times respectively, t_{mean} is the mean of these two times ($\frac{\langle t_L + t_R \rangle}{2}$) and t_{eb} is the electron bucket time which produced the photon.

To calculate the new or corrected slope constants (the multiplicative factor required to convert a TDC channel to ns), S_L and S_R , we use the following relations:

$$S_L = s_l \times \frac{1}{(1 - \beta_{LR})(1 - \beta_{RF})} \simeq s_l \times (1 + \beta_{LR})(1 + \beta_{RF}), \quad (4.1)$$

$$S_R = s_r \times \frac{1}{(1 + \beta_{LR})(1 - \beta_{RF})} \simeq s_r \times \sim (1 - \beta_{LR})(1 + \beta_{RF}), \quad (4.2)$$

where S_L and S_R are the newly calculated slopes for the left and right TDC slopes respectively and s_l and s_r are the pre-calibration slopes for the left and right TDCs respectively. A calibrated T-counter should exhibit a flat slope at a time difference of zero when plots of $\frac{\langle t_L - t_R \rangle}{2}$ versus t_{mean} and $\langle t_{mean} - t_{eb} \rangle$ versus t_{mean} are examined. A well calibrated set of TDC slopes is illustrated in the top left of figure 4.4. All T-counter slopes are shown using an arbitrary scale, the times are in ns .

Base Peak Calibrations

The TDCs in the tagger operate in what is known as common-start self-triggered mode. This means that they start to measure time when either the CLAS level 1 trigger fires (common-start) or when a hit is recorded on a T-counter (self-triggered). Since either the left or right TDC registers the first time and become the trigger, the base peak calibration constant is the mean position of the TDC peak. As a result of this, the actual time measured by the T-counter TDCs is

the TDC time with the base peak constant subtracted, and therefore corrected for the signal delay.

The constants are evaluated with the following definitions for each individual T-counter T_i ($i = 1...61$):

$$\langle Peak(L)_i \rangle = \langle TDC(L)_i \rangle - \langle T(L/R)_i \rangle, \quad (4.3)$$

$$\langle Peak(R)_i \rangle = \langle TDC(R)_i \rangle - \langle T(R/L)_i \rangle, \quad (4.4)$$

where $Peak(L)_i$ and $Peak(R)_i$ are the new constants (absolute peak positions) for the T-counter TDCs (left and right respectively), $TDC(L)_i$ and $TDC(R)_i$ are the measured TDC times for the left and right respectively and $T(L/R)_i$ and $T(R/L)_i$ are related to the relative time delays between the left and right (right and left) TDCs. This relative time delay is used to account for certain physical factors, for example, the fixed cable delays. Provided the hardware alignment is good enough, then the timing window for coincidences can be made shorter and therefore improve the real to random ratio. Even with perfect alignment, however, the timing window still has a width at least as wide as the resolution of a single channel.

RF Timing Adjustments, C'_i s

After these previous stages have been completed we must now identify the correct RF beam bucket from which the reconstructed hit was obtained. The available RF time is actually given relative to the trigger time, t_{RF} . The information it provides then, is related to the phase shift between the machine RF time, with a period of 2.004 ns, and the trigger. The time of the tagged photon, t_{TPHO} , is given by the equation:

$$t_{RF} = t_{TPHO} + k_{event} \times 2.004, \quad (4.5)$$

where k_{event} is the RF beam bucket offset and determined on an event by event basis. The method of determining t_{TPHO} is now explained.

To improve the timing alignment from the previous section (4.4.2), a reference detector is decided upon. For experiments involving photon running this is the start counter, and so it was for g13. The start counter is typically chosen as this is the first subsystem which detects reaction products in CLAS. By using a reference time, t_{REF} , from the chosen reference detector, the T-counter mis-

alignment at the trigger level can be determined and corrected for. This is done by the application of a constant for each T-counter, C_i^{REF} ($i = 1...121$), defined by the following:

$$C_i^{REF} = \langle t_{mean}^i - t_{REF} \rangle, \quad (4.6)$$

$$C_i^{REF} = (\langle D_i \rangle + \langle T_i \rangle) - \langle D_{REF} \rangle, \quad (4.7)$$

where t_{REF}^i is defined as before, D_i is the delay from the production of a tagged photon until the signal output of the T-counter, T_i is the delay from the output signal to the trigger and D_{REF} is the delay from the production of a photon to the TDC stop signal.

So far this stage has used the start counter for a reference time, but a more ideal solution would be to utilise the accelerator RF timing as a reference as this is more accurate and has a resolution of ~ 80 ps. However, to be able to use the RF as a reference, the RF phase shift for each T-counter has to be determined and accounted for by the constant C_i^{RF} , defined to be:

$$C_i^{RF} = \langle D_i \rangle + \langle T_i \rangle - \langle t_{eb} \rangle + k_i \times 2.004, \quad (4.8)$$

where k_i is an integer which takes a different value for each T-counter. The top middle plot of figure 4.4 shows the tagger time minus RF time distribution across all T-counters, which is used to calculate C_i^{RF} .

Now that we have obtained values for C_i^{REF} and C_i^{RF} we can now compute the value of k_i and therefore the exact C_i calibration constant for each T-counter. This is done using the following relations:

$$C_i^{REF} - C_i^{RF} = \langle D_{REF} \rangle + \langle t_{eb} \rangle - k_i \times 2.004, \quad (4.9)$$

$$C_i = \langle D_i \rangle + \langle T_i \rangle - \langle t_{eb} \rangle, \quad (4.10)$$

$$C_i = C_i^{RF} - k_i \times 2.004. \quad (4.11)$$

Once the procedures described above have been completed, two times for an event are now available in the TAGR bank, which (after the tagger has been aligned to the time of flight subsystem, see section 4.4.2) can now be used in further physics analysis. The first is the tagger time reconstructed on an event by event basis, t_{TAG} , and the second is RF bucket real time, considered to be the actual photon time, t_{PHO} . These are defined as follows:

$$t_{TAG}^i = t_{mean}^i - C_i, \quad (4.12)$$

$$t_{TPHO} = t_{RF} - k_i \times 2.004. \quad (4.13)$$

The photon tagger timing and the beam RF timing are now considered to be calibrated and aligned.

Tagger to Time of Flight Offset

When photoproduction data are being analysed, the time attributed to the tagged photon should be defined to be the time it takes the photon to reach the centre of the CLAS target, which is the assumed interaction point. This time is relative to the CLAS detector subsystems and can be defined, since the RF timing and the T-counter signal are now independent of each other. The principles and methods used to determine this tagger to time of flight offset, known as *tag2tof*, are the same as those for *st2tof*, explained in section 4.4.1. This timing convention in the physics analysis of data is accounted for by the addition (within the TAGR bank) of the *tag2tof* constant to the t_{TTAG} and t_{TPHO} values.

Tagger Energy Calibration

The energy calibration of the photon tagger is achieved using a model of the design geometry of the scintillation hodoscope (384 overlapping E-counters) and a two-dimensional field map of the pair spectrometer (PS) dipole magnet. The tagged photon energy spectrum is measured in coincidence with e^+e^- pairs as a function of the PS magnetic field and by taking advantage of the internal linearity of the PS, the energy of the tagging system can be calibrated. The absolute energy scale was determined using the e^+e^- rate measurements close to the end-point of the photon spectrum.

The PS consists of an aluminium pair production converter, eight scintillator paddles and a large aperture dipole magnet. The system is located 10 m downstream of the photon tagger radiator. The aluminium foil, which is 10^{-3} radiation lengths thick, is positioned 5.77 cm upstream of the dipole magnet within its magnetic field. The scintillators are positioned symmetrically on each side of the beamline and are arranged such that the PS can detect e^+e^- pairs over the full tagger energy range. The PS also contains two pairs of microstrip detectors covering an area of 400 mm². These microstrips allow for better determination of e^+e^- position.

The PS operates on the principle that when a photon interacts with the aluminium foil converter it will produce an e^+e^- pair. The magnetic field then sweeps these pairs out of the beamline and into the spectrometer scintillator and

microstrip detectors. The PS can then be used to determine the energy of the e^+e^- pair from their hit positions and can thus be used to infer the energy of the interacting photon.

In detail, the tagged photon energy, E_{tagg} , is measured in coincidence with e^+e^- pairs detected in the PS at different PS magnetic field settings. The photon energy measured in the PS, E_{calc} , is given by the following relation:

$$E_{calc} = E_{e^-} + E_{e^+} \quad (4.14)$$

where E_{e^-} and E_{e^+} are the energies of the electron and positron respectively, as determined from the reconstructed lepton trajectories and the PS magnetic field. During these special calibration runs, the data acquisition was triggered by a coincidence signal between the scintillation counters in the PS corresponding to the detection of an e^+e^- pair. For each triggered event, the information from the pair spectrometer and microstrip detectors, as well as the photon tagger E and T-counters was recorded. The ratio, $R = E_{calc}/E_{tagg}$, can then be calculated for each E-counter on an event by event basis. Ultimately, this ratio can provide an independent energy calibration of the photon tagger E-counters, and a correction factor which can be applied to the photon energy at the physics analysis stage.

4.4.3 Time of Flight Calibration

The time of flight calibration [81] process is an essential part of determining the quality of the charged particle identification and the mass resolution (see section 3.4.4). Moreover, it is at this point in the overall calibration process where the start counter, photon tagger and time of flight timings are aligned relative to each other. The TOF calibration has several stages, each of which is given a brief description in this section. The stages are as follows:

1. Status and pedestals.
2. TDC calibration.
3. Time-walk correction.
4. Left-Right PMT alignment.
5. Energy loss and attenuation length calibration.
6. Effective velocity calibration.
7. Counter to counter delay calibration.

The *status* of a scintillator is flagged for subsequent stages of the TOF calibration process, regardless of whether or not one or both sides of the scintillator are dead and the *pedestals*, which are ADC channels corresponding to zero, are measured using a pulse trigger.

The *TDC calibration* takes the form of a channel to time (ns) conversion. The response of the TDC to special pulser runs is analysed for different start-stop delays of the sent pulse. The resulting TDC channel vs. time distribution is fitted with the following function:

$$t = c_0 + c_1T + c_2T^2,$$

where c_0 , c_1 and c_2 are the determined calibration constants, T is the TDC channel number and t is the time in ns.

Time-walk corrections as a function of pulse height are determined for each PMT by performing special laser runs. It is because of the height-dependent rise time of an analogue pulse that this correction is necessary.

The *Left-Right PMT alignment* of each scintillator is the next stage of the TOF calibration. This alignment and the resulting left-right time offsets allow for the determination of hit position within the scintillator. The hit position from the TDC left and TDC right are then plotted for each scintillator on a sector-by-sector basis. This sector based distribution should be symmetric around zero, that is to say the x-projection of the left and right edges ($edge_L$ and $edge_R$, respectively) for each scintillator should be symmetric around zero. Any left-right time offset, Δt , arising is calculated via the following relation:

$$\Delta t = (edge_L + edge_R)/v_{eff},$$

where v_{eff} is the effective velocity in the scintillator material with a nominal value of $1.6 \times 10^8 \text{ ms}^{-1}$.

The next stage of the calibration process is the calculation of *energy loss*, $\delta E/\delta x$, in the scintillator, and the *attenuation length* of each scintillator. Reasonable timing calibrations are required for this stage in order to select pions for the energy loss calibration. Loose timing cuts are used to identify pions and the geometric mean position of the Minimising Ionising Particle (MIP) is measured for each scintillator using the pulse height outputs of the left and right ADCs. The MIP pulse heights are then normalised such that a particle incident normally at the centre of a scintillator bar has a pulse height equivalent to 10 MeV. The attenuation length is then calculated by determining the relation between the amount of light arriving at each PMT and the hit position along the scintillator.

The second-to-last stage is the calibration of the *effective velocity*, v_{eff} . The hit position along a scintillator with respect to the centre, y , is determined using timing information from both ends of the scintillator. Moreover, position y can be determined from tracking information. Therefore, a fit to the difference between the left and right timings (t_L and t_R) vs. y , can be used to determine v_{eff} and the position offset, y_{offset} , for each scintillator, using the relation:

$$y = \frac{v_{eff}}{2}(t_L - t_R - y_{offset}),$$

where t_L and t_R are the adjusted times from the left and right PMTs respectively. This calculated value is then used in the next TOF calibration loop at stage 4.

In the final stage of the TOF calibration the *counter to counter delays* are calibrated. Each of the time of flight subsystems 288 scintillator counters must have their timing aligned with the start counter and photon tagger subsystems. Pions are selected by cutting on the energy deposited in each scintillator and a distribution of vertex time from time of flight minus vertex time from the start counter/ photon tagger is produced. The main peak of this distribution is then fitted, and an offset can be determined which centres the peak on zero.

4.4.4 Drift Chamber Calibration

The drift chamber (section 3.4.3) calibration [77, 80] is required to accurately reconstruct the path a particle travelled through CLAS. This track reconstruction is based upon the measurement of the position of a particle within the drift chamber cells and is performed in two stages. The first stage is Hit Based Tracking (HBT) and the second, Time Based Tracking (TBT).

Hit based tracking is based upon a least squares fit of a track to hit wire position and is calculated when at least three out of five superlayers register a hit. The track segments resulting from the HBT are then linked across all superlayers in a region and all three regions in order to reconstruct the particle's track. HBT, however, has poor momentum resolution ($\sim 3 - 5\%$ for a 1 GeV/c track) due to the radially increasing diameters of the cells and the possibility of *holes* in the drift chamber. Holes are defined to be areas in a chamber with dead wires and they result in less than the maximum 34 layers registering track hits.

For the second stage, time based tracking, we require a measurement of the *drift time*. Here, information about the particle's flight time from the target to the time of flight scintillators is used to augment the drift time. A lookup table is then used to convert these augmented drift times into drift distances within

the cells, then, within each cell, these positions are fitted in order to determine the track parameters. The drift time, t_{drift} , is defined as:

$$t_{drift} = t_{start} + t_0 - t_{TDC} - t_{flight} - t_{prop} - t_{walk},$$

where t_{start} is the start time of the event, t_0 is the time delay of the wire, t_{TDC} is the raw measured time of the TDC, t_{flight} is the flight time of the particle to travel from the reaction vertex to the wire, t_{prop} is the propagation time of the signal along the wire, and t_{walk} is a time-walk correction made for short drift times differences in ionisation of slow and fast moving particles. The implication of this last term is simply that minimum ionising particles produce smaller signals, resulting in larger time smearings. It should be pointed out that t_{start} is constructed based upon coincident signals from the photon tagger, start counter and time of flight subsystems for photon experiments such as g13. TBT improves the momentum resolution for a 1 GeV/c track to $\sim 0.5\%$.

4.4.5 Electromagnetic Calorimeter Calibration

The aim of the electromagnetic calorimeter (section 3.4.5) calibration [82] is to find an agreement between the vertex time of a track measured by the electromagnetic calorimeter and an independent vertex time of a track as measured by the time of flight subsystem. This means that the EC vertex time minus the TOF vertex time distribution should be centred on zero. It is necessary that the EC time is well defined as this is essential in discriminating between photons and neutrons where detected particle's velocity is what identifies one from the other. It should be noted that not the entire energy of the neutron is deposited in the calorimeters. The calibration of the large angle electromagnetic calorimeters is done in a similar fashion.

4.5 Photon Polarisation

In order to obtain the degree of photon polarisation for any event we must first determine the coherent edge position, and the relationship between photon energy and polarisation when the coherent edge is at any position for any given polarisation plane. The photons are linearly polarised using the CB technique, as described in section (3.2). To maximise the degree of polarisation in the photon energy range of interest, the crystal is adjusted to position the coherent peak in the appropriate position in the photon energy spectrum. For example, figure 4.6

shows the enhancement spectrum as set up for polarised photons in the 1750 - 1950 MeV range. To obtain the degree of polarisation as a function of photon energy this enhancement spectrum from TDC fits is compared to an analytical Bremsstrahlung (ANB) calculation, which allows the user to adjust the beam divergence and other relevant parameters. A more detailed treatment of these parameters is given in [51]. Once the optimum agreement between data and calculation is found a set of polarisation lookup tables is generated; each table corresponds to a slightly different position of the coherent peak within the region of interest. This allows an event by event determination of the photon polarisation. The enhancement spectrum is regenerated for every 2 ns of data, and fitted with a 4th degree polynomial to determine the position of the “coherent edge” (figure 4.5) and hence select the appropriate lookup table for that 2 ns chunk of data. Such a technique is essential to allow for some drift of the coherent peak around its mean position due to small changes in the angle between the electron beam and the crystal lattice. The typical variation in the coherent edge position over a run is shown in figure 4.7.

Having now got mean polarisation values for each electron and photon beam and plane setting in g13a, the polarisations were then scaled according to the number events for each plane setting at each electron beam energy, resulting in an overall weighted mean value of the linear photon polarisation for g13a. These were the final values that were used to extract the beam asymmetry measurements for this analysis. The degree of linear polarisation achieved for the different coherent peak settings was $\sim 72 - 78\%$.

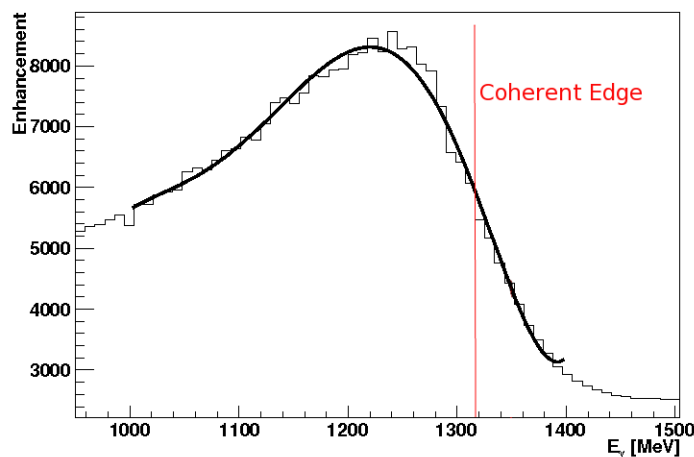


Figure 4.5: Enhancement plot.

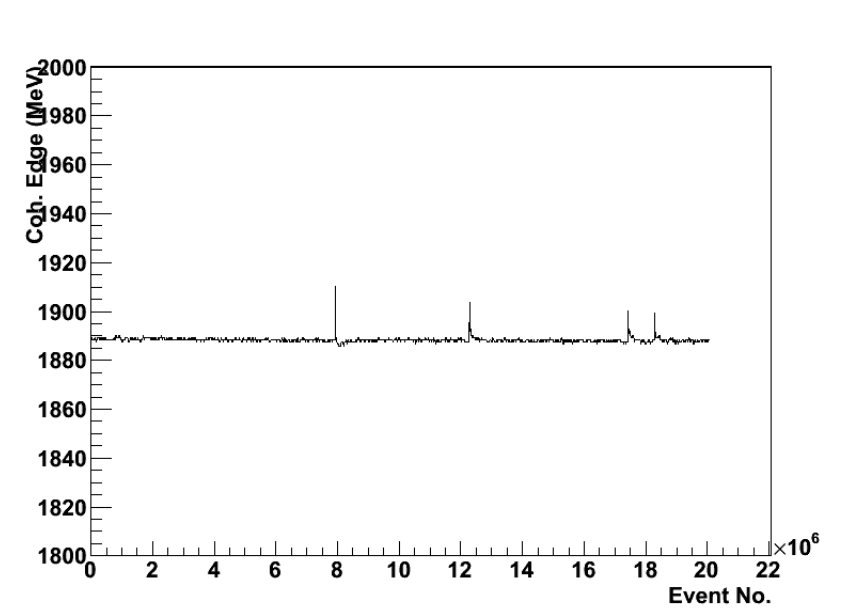


Figure 4.7: A typical variation of the coherent edge position over one run. While the position remains very steady, beam trips can be seen as individual spikes.

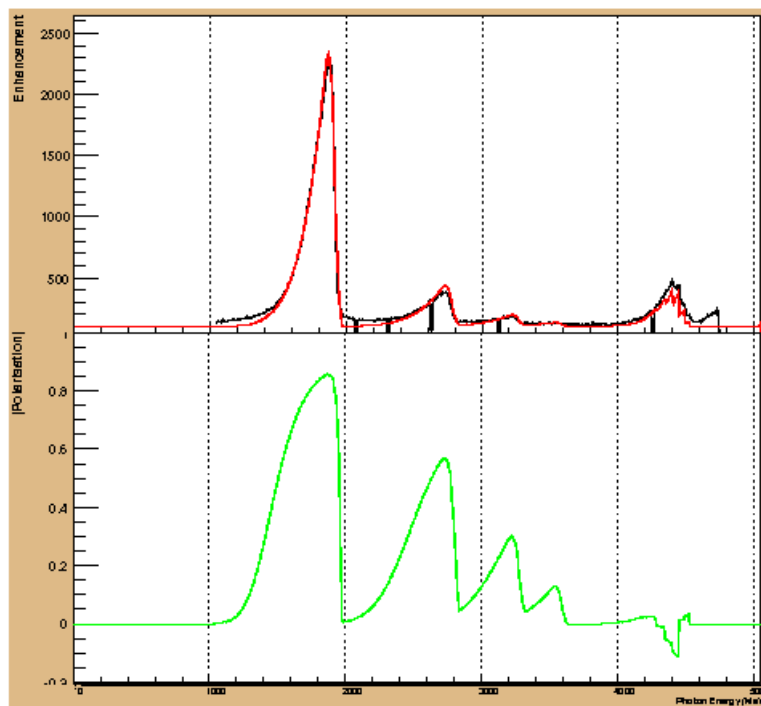


Figure 4.6: Collimated tagger scaler spectra compared with the ANB [91] calculation for the 1.9 GeV coherent peak position (top). The calculated photon polarisation versus energy (bottom).

The systematic uncertainties associated in obtaining the polarisation from

the ANB method arise from four main sources. These are the dependence of the polarisation on the tagger E-plane; the limit between the theoretical and data comparison; the changing height of the coherent peak and the uncertainty from the TDC spectra normalisation. The first effect arises because as many as six E-bins can be associated with each T-bin for which the polarisation is calculated. This can introduce an uncertainty in the true position of the coherent edge which can cause a change in the mean polarisation. The second effect arises from their being a range of parameters which will give equally good comparisons between the data and the calculation. The varying height of the coherent peak is caused by instabilities in the position of the electron beam and can give rise to a shift of the coherent edge position (see figure 4.5). This change of the apparent height of the coherent peak can produce an associated change in the polarisation due to varying numbers of the photons that are under the peak. The last case comes as a result of the signal noise in the TDC spectra that may cause errors in the normalisation procedure.

All these effects were considered in a previous analysis [51] which found the combined systematic uncertainty in the photon polarisation to be $\pm 4.3\%$. Further to this, it should be noted that there does appear to be some systematic effect when trying to calculate the photon polarisation at energies right on the coherent edge. This is due to the comparison between the data and calculation not being reliable at these energies. To fully calculate the systematic contribution from this it will be necessary to study the photon polarisation using a high statistics single pion analysis. Such a study is outwith the scope of this work but is currently being undertaken. This additional information will either improve the comparison with the higher statistics available or will be able to quantify the systematic uncertainty and therefore allow it to be accounted for. For the purposes of this analysis, a slightly larger $\pm 5\%$ systematic uncertainty will be used.

4.6 Summary

Once the processes described in this chapter have been completed, the data are then considered to be fully calibrated and in a format which can now be used for physics analysis. The information contained within the data is used for initial particle identification and the construction of 4-vectors. These particle 4-vectors allow for the physics analysis of events of interest within the data. The initial particle identification and event selection, along with the results of the data analysis, are presented in the following chapters.

Chapter 5

Data Analysis

This chapter describes the details of the analysis of the $\gamma d \rightarrow K^+ p \pi^-(n)$ channel from the g13 experiment. In this channel the neutron has been reconstructed by missing mass ($\gamma d \rightarrow p K^+ \pi^-$) from the corresponding 4-vectors of the detected particles. The analysis is presented for the conditions of the g13 experiment that have been described in 3. The steps described follow the order of the analysis as it was performed and the results for the complete range of photon energies covered during g13 (1.3 - 2.3 GeV in 200 MeV steps) are presented.

5.1 Particle Identification and Event Selection

5.1.1 TOF Mass Cuts

The first step in identifying the $\gamma d \rightarrow K^+ \Lambda^0(n) \rightarrow K^+ p \pi^-(n)$ and $\gamma d \rightarrow K^+ \Sigma^0(n) \rightarrow K^+ \Lambda^0 \gamma(n) \rightarrow K^+ p \pi^- \gamma(n)$ reactions is to select only those recorded events that contain the appropriate number of charged particles in the final state, in this case, three particles, plus the additional constraint of there being a minimum of one hit registered in the photon tagger. The neutron only spectates in this reaction and the neutron detection efficiency and momentum resolution of the CLAS detector means that reconstructing the neutron by missing mass results in better statistics. This means that only the three charged particles (K^+ , p and π^-) are detected in CLAS and the neutron is reconstructed from the missing mass of $\gamma d \rightarrow K^+ p \pi^-(n)$. The primary cut to be implemented in the analysis was a cut based purely on the mass squared as calculated by the time of flight detector subsystem (3.4.4) and was dependent upon the charge of the detected particle. The criteria were as follows:

- Detected non-zero charged particle must have a valid drift chamber track

and either an associated valid time of flight hit or an electromagnetic calorimeter hit.

- Selected time-of-flight mass squared range depending on particle charge as follows:
 - Positively charged particle, $0.49 < \text{mass}^2 < 1.44$ (GeV/c^2), possible proton identification.
 - Positively charged particle, $0.1 < \text{mass}^2 < 0.49$ (GeV/c^2), possible K^+ identification.
 - Negatively charged particle, $0 < \text{mass}^2 < 0.1$ (GeV/c^2), possible π^- identification.

At this point the hadron identification is only preliminary as there is not yet any clear distinction between kaons and pions. The TOF masses for all particles detected in this reaction can be seen in figure 5.1 below.

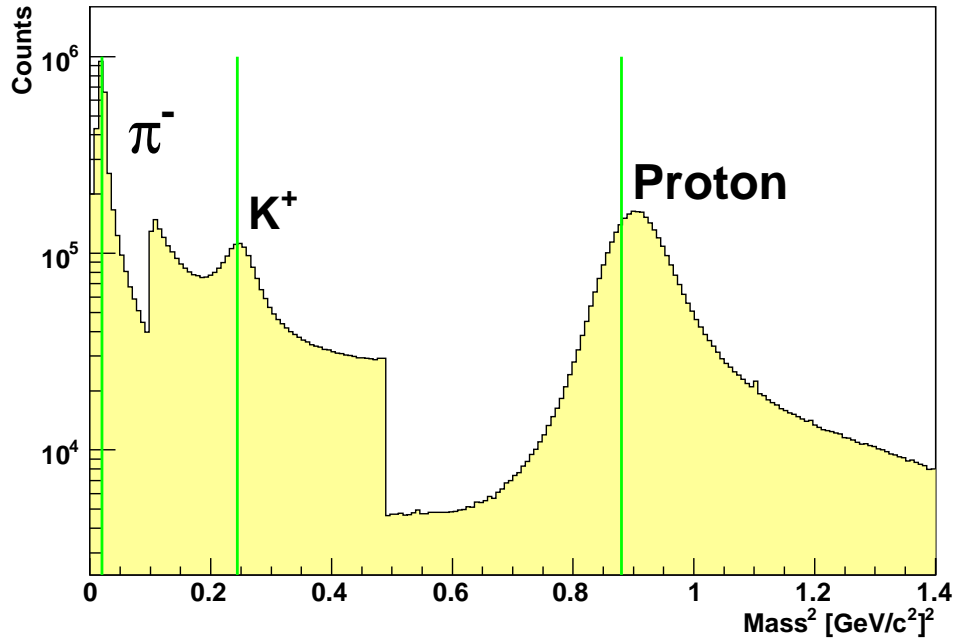


Figure 5.1: TOF mass² plot after simple selection criteria on the number of event particles allowed. It shows that the mass cuts can identify reasonably well the isolated protons but still they still exhibit some uncertainty over the kaon and pion separation. The sharp cutoff regions indicate where the cuts were placed to identify each particle and there are an equal number of counts in each region between the cutoffs.

When an event potentially contains $K^+p\pi^-$ according to these criteria, it is then allowed to pass on to the further stages of event selection.

5.1.2 Photon Selection

The second stage in the event selection process is that of identification of the corresponding event photon. Where an event has more than one photon (tagger hit), the actual event photon is identified to be the one whose time is closest to the event vertex time, the so-called “best” photon. This is done by minimising the time difference (*Diff*) between the proton vertex time and the photon vertex time according to the relation:

$$Diff = (TOFtime(p) - (TOFpath(p)/c \times \beta_c(p))) - (\gamma_{time} + (z(p)/c)) \quad (5.1)$$

where:

$$\beta_c(p) = p(p) / \sqrt{p^2(p) + m_{pdg}^2(p)} \quad (5.2)$$

using the PDG mass for the proton and the measured momentum.

Where:

$TOFtime(p)$ =proton TOF time,

$TOFtime(p)$ =proton path length to the TOF,

γ_{time} =event photon vertex time,

$z(p)$ =z - vertex position of the proton,

c =the speed of light.

If an event was found to have more than one photon in the same minimal vertex timing difference window (one 2 ns beam bucket) it was rejected. This occurs less than 1% of the time so the statistics that were lost because of this was negligible. This timing difference is shown in the top plot of figure 5.3.

At this point the tagger energy correction is applied to the identified photon. The correction is derived from the pair spectrometer and this accounts for E-counter to E-counter non-linearities, taking the form of a multiplication factor to E_γ , the photon energy.

5.1.3 Mis-identification of mesons

At this point in the analysis it is prudent to assume that a number of the reaction particles have been mis-identified with particles having a different mass but the same charge. In order to remove these mis-identified particles from the rest of the analysis, the momentum based on the drift chamber track is retained, but the mass is re-assigned to the PDG value of a viably mis-identified particle. The considered mis-identifications were as follows:

- Possibly identified K^+ as a mis-identified π^+ .
- Possibly identified K^+ as a mis-identified p .
- Possibly identified π^- as a mis-identified K^- .

In all of these cases the 4-vector is subsequently re-calculated along with the missing mass squared (MM^2) of the system and cuts are applied to remove events where it can be seen one of the reaction particles has been positively mis-identified according to the regime described above. The x-axis of each of each plot shows the undetected spectator neutron for $K\Lambda$ or the neutron plus photon in the case of the $K\Sigma^0$ channel. The undetected photon contributes to the smearing of the missing mass squared of the plots. More explicitly, the $MM^2(K^+p\pi^-)$ is assumed to conform to one of the following arrangements:

Case 1: $MM^2(\pi^+p\pi^-)$

From figure 5.2 it can be seen that there are events where a π^+ has been mis-identified as a K^+ . These events are been rejected by the cut $MM^2(\pi^+p\pi^-) < 0.98$ MeV. These events correspond to the concentration of events visible on the lower left of the figure at the mass squared of the missing neutron on the y-axis. The actual missing neutron that is associated with $K^+p\pi^-$ events corresponds to the upper right concentration in the figure.

Case 2: $MM^2(pp\pi^-)$

Figure 5.2 also shows events where a proton has been mis-identified as a K^+ . In this case, the events are rejected by the cut $MM^2(pp\pi^-) < 0.55$ MeV and in the figure these correspond to everything occurring below the red line.

Case 3: $MM^2(K^+pK^-)$

In the final case from figure 5.2, we can see events where a K^- has been mis-identified as a π^- and here the events are rejected by the cut $MM^2(K^+pK^-) < 0.55$ MeV.

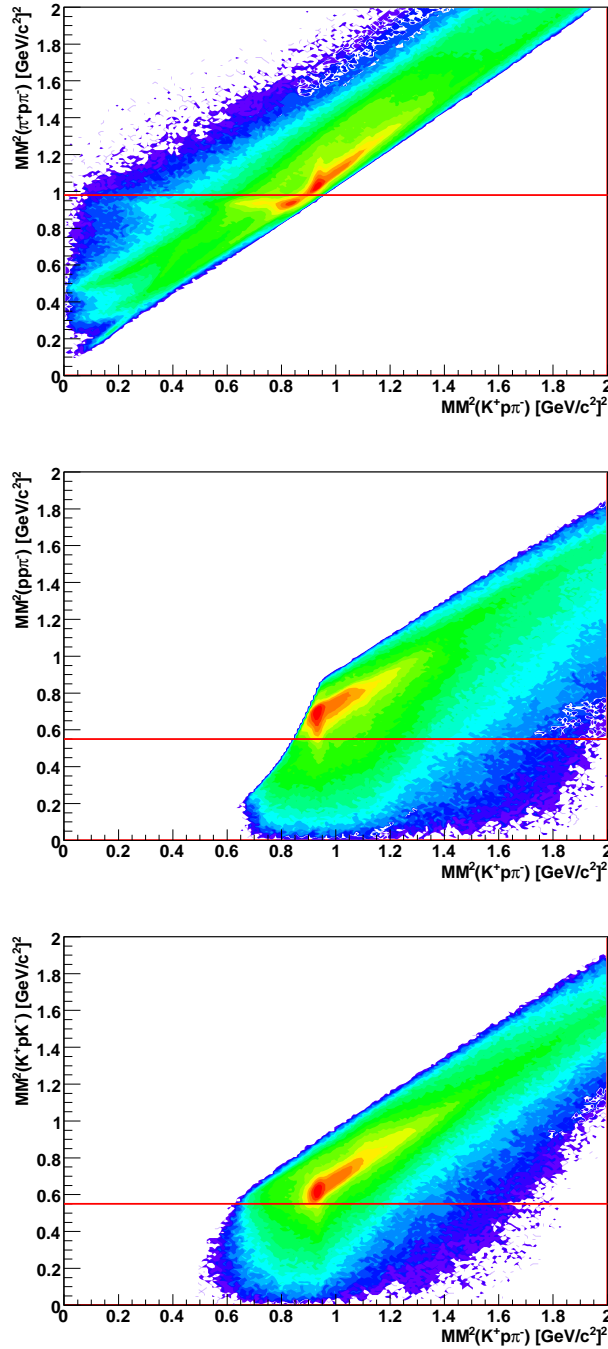


Figure 5.2: case 1: $MM^2(K^+p\pi^-)$ vs. $MM^2(\pi^+p\pi^-)$, case 2: $MM^2(K^+p\pi^-)$ vs. $MM^2(pp\pi^-)$, case 3: $MM^2(K^+p\pi^-)$ vs. $MM^2(K^+pK^-)$.

5.1.4 Hadron - Photon Vertex Timing Cuts

Before the vertex timing cuts are applied a cut of 300 MeV/c minimum momentum is applied to the identified hadrons in the reaction channel. This 300 MeV/c is the minimum detection momentum in CLAS.

Generally, if the timing calibrations of the detector subsystems are well defined, the vertex time of the hadron would be the same as that of the photon (i.e. their difference would be centred on zero, see top plot in figure 5.3). The slightly asymmetric shape of the distribution comes from the fact that the detected protons and pions have a detached vertex. This arises since the original decaying hyperon has time to appreciably move before it decays into the proton and π^- that are finally detected. The vertex time difference apparent in peaks at 2, 4, and 6 ns means that the associated identified photon was from a (2 ns) beam bucket 1, 2, or 3 earlier than the event proton. The best photon was then selected and the resulting peak from the distribution was fitted with a Gaussian function and a $\pm 3\sigma$ cut was applied.

The bottom plot in figure 5.3 shows the proton-photon vertex timing after the “best” photon selection, and the timing cut has been indicated. Figure 5.4 shows the result of applying the timing cuts to the K^+ and the π^- .

5.1.5 Hadron - Hadron Vertex Timing Cuts

The final constraint placed on the timing was a cut on the vertex time between the various identified reaction hadrons, more specifically, the proton-kaon (t_v^{pK}) and the proton-pion ($t_v^{p\pi}$) vertex times. As with the hadron-photon vertex timing described in the previous section (5.1.4) the peak was fitted with a Gaussian function and cut on $\pm 3\sigma$ was applied. Figure 5.5 (top) shows the effect of the timing cut for the K^+ whilst figure 5.5 (bottom) illustrates it for the π^- .

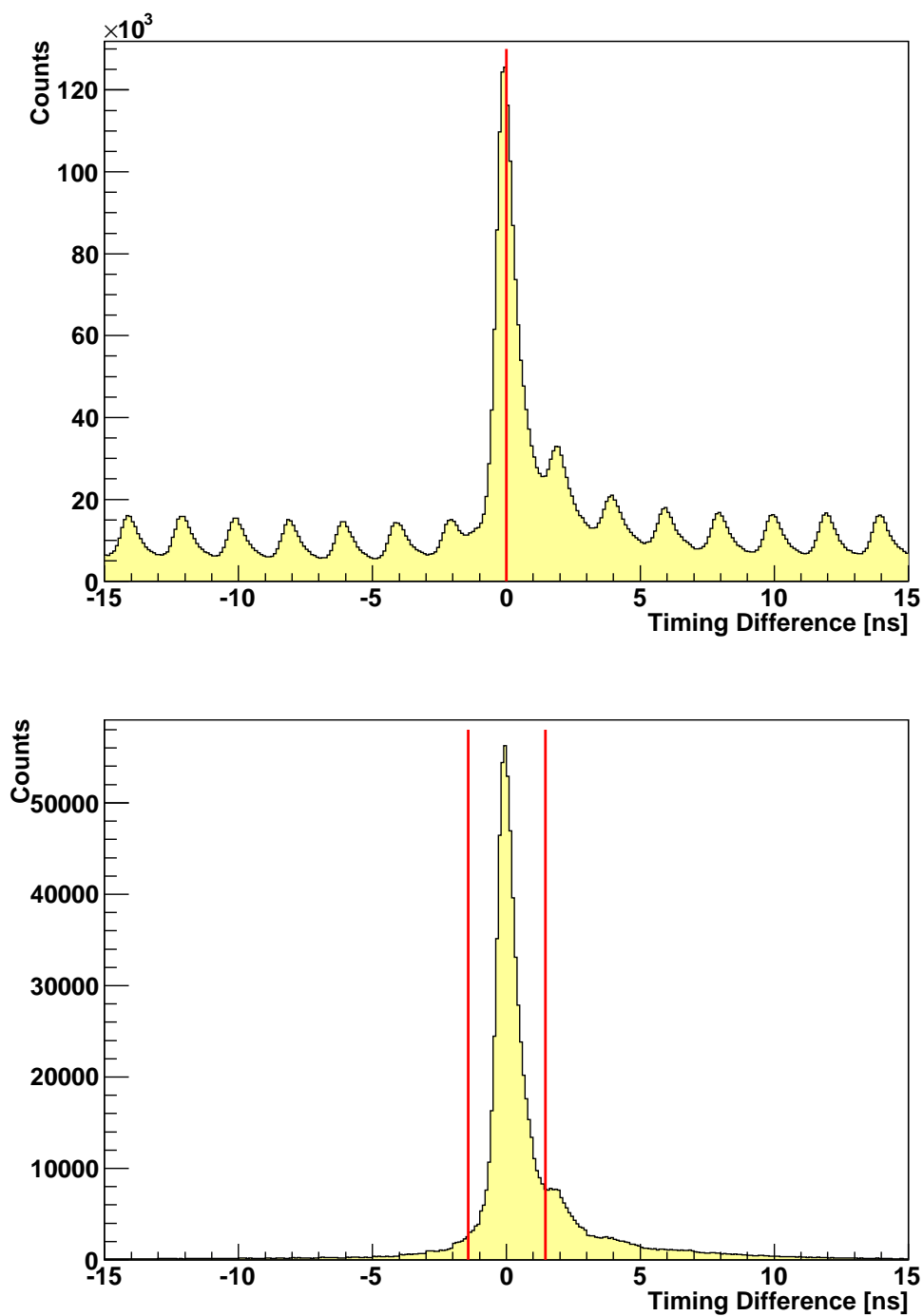


Figure 5.3: (top) $t_v^{P\gamma}$ for all photons, $t_v^{P\gamma}$ after “best” photon selection with $\pm 3\sigma$ cuts indicated by red lines.

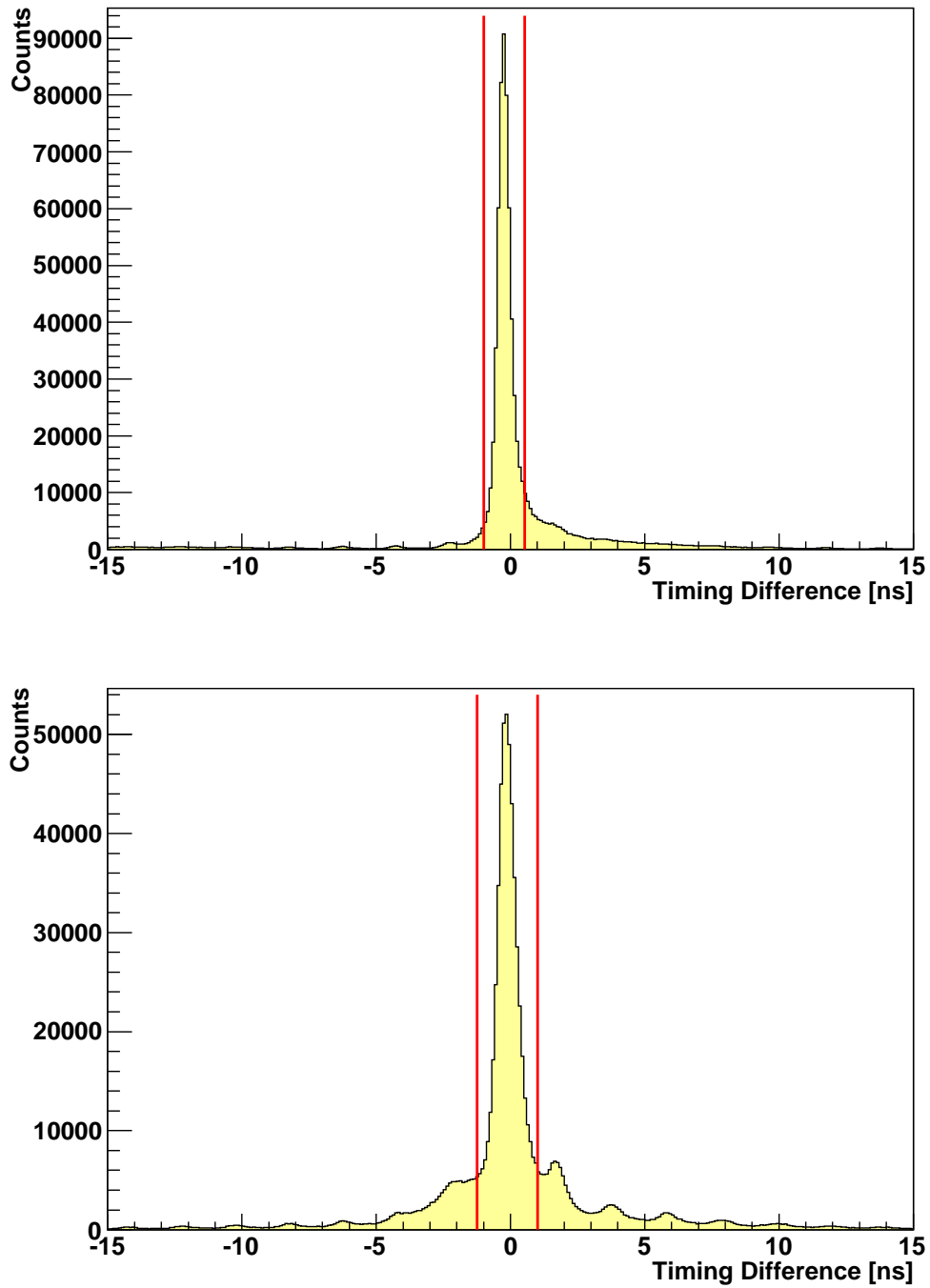


Figure 5.4: $t_v^{K^+\gamma}$ (top) and $t_v^{\pi^-\gamma}$ (bottom) after “best” photon selection, with $\pm 3\sigma$ cuts indicated by red lines.

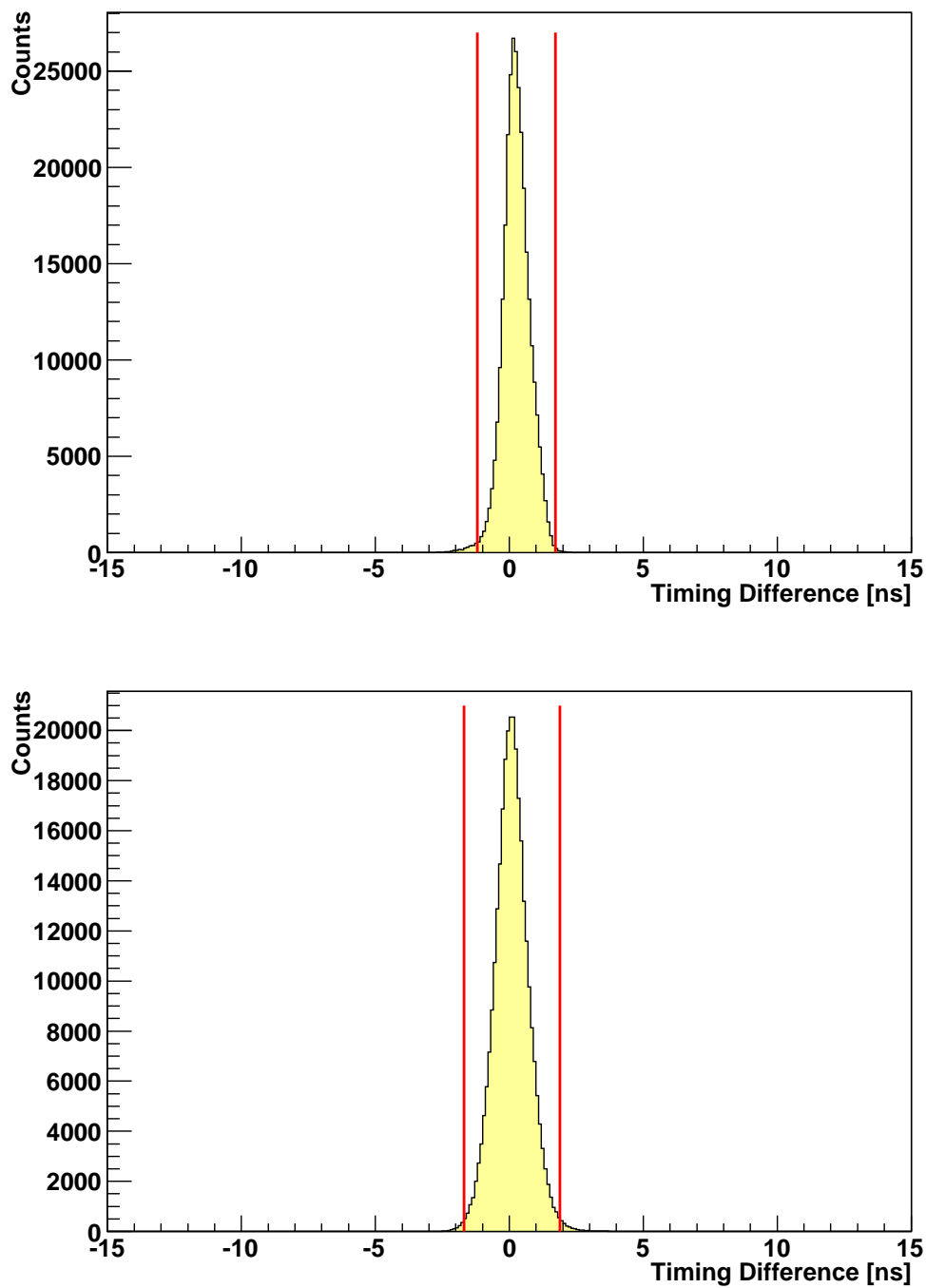


Figure 5.5: $t_v^{PK^+}$ (top) and $t_v^{P\pi^-}$ (bottom), after “best” photon selection, with $\pm 3\sigma$ cuts indicated by red lines.

5.1.6 Invariant Mass Cut

The final step in identifying the correct reaction particles involves a cut on the $[p + \pi^-]$ invariant mass so as to correctly identify those particles that came from reactions involving a Λ . These should reconstruct to a Λ invariant mass and by subsequently fitting a Gaussian to this invariant mass distribution a $\pm 3\sigma$ cut is used to identify the correct particles. This is shown in figure 5.6. At this point in the analysis, all the particles required for the $\gamma d \rightarrow K^+ p \pi^- (n)$ exclusive reaction have been identified and are now used in further analysis.

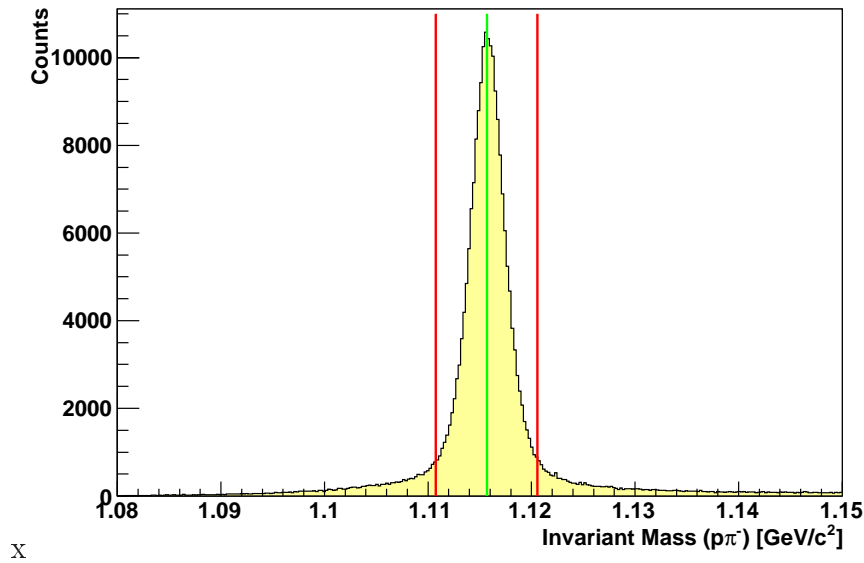


Figure 5.6: Invariant mass of $p + \pi^-$ with $\pm 3\sigma$ cuts indicated by red lines. PDG mass indicated by green line.

5.1.7 Energy Loss / ELOSS

A charged particle's original momentum at its production vertex is larger than that which is measured in the drift chambers. The reason for this is that a charged particle deposits some of its energy in the target cell, the target walls, the beam pipe, supporting structures and the start counter. The amount of this energy loss, or ELOSS, must now be accurately determined and the measured momentum appropriately corrected. By passing the particle's 4-momentum and vertex position, along with the geometry of the g13 target cell, into the ELOSS routine [92], the correction is determined. The momentum correction distributions (Δp vs. p) for the proton, the π^- and the K^+ are shown in figure 5.7 below.

As can be seen, more energy is deposited by a low momentum particle and consequently it will require a larger correction, whilst the opposite is also true for high momentum particles. This correction was applied very early on in the analysis, after preliminary particle identification and candidate reaction selection. The first analysis cut to be made subsequent to the ELOSS correction was the best photon selection.

5.1.8 Fiducial Cuts

Fiducial cuts are implemented in the analysis in order to account for and exclude those events which have a particle detected in a region of non-uniform acceptance in CLAS. Areas of non-uniform acceptance can be found at the edge regions of the drift chamber sectors and also in regions where particles could interact with the torus magnet coils. The cuts implemented here are designed to be the same for all sectors of CLAS, and are dependent upon angle (azimuthal ϕ) and charge. These cuts are applied after the implementation of all other corrections and cuts. For this analysis a fiducial cut on the azimuthal distributions of $\pm 5^\circ$ at each sector division in CLAS was used.

Figure 5.8 below shows the hit occupancy (ϕ vs. θ angle) for the 6 different drift chamber sectors, for both positively and negatively charged hadrons. The effect of the fiducial cuts on one sampled sector is also shown for positive and negative hadrons.

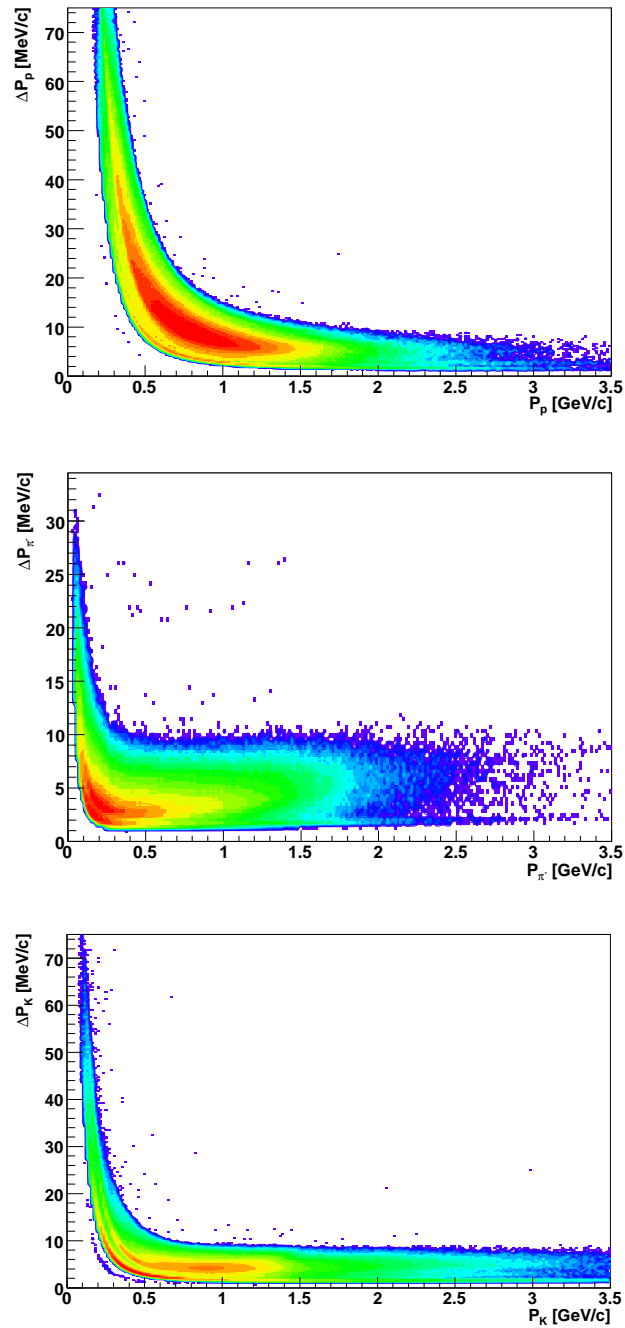


Figure 5.7: (Top) ΔP vs. P for the proton, (middle) ΔP vs. P for the π^- and (bottom) ΔP vs. P for the K^+ .

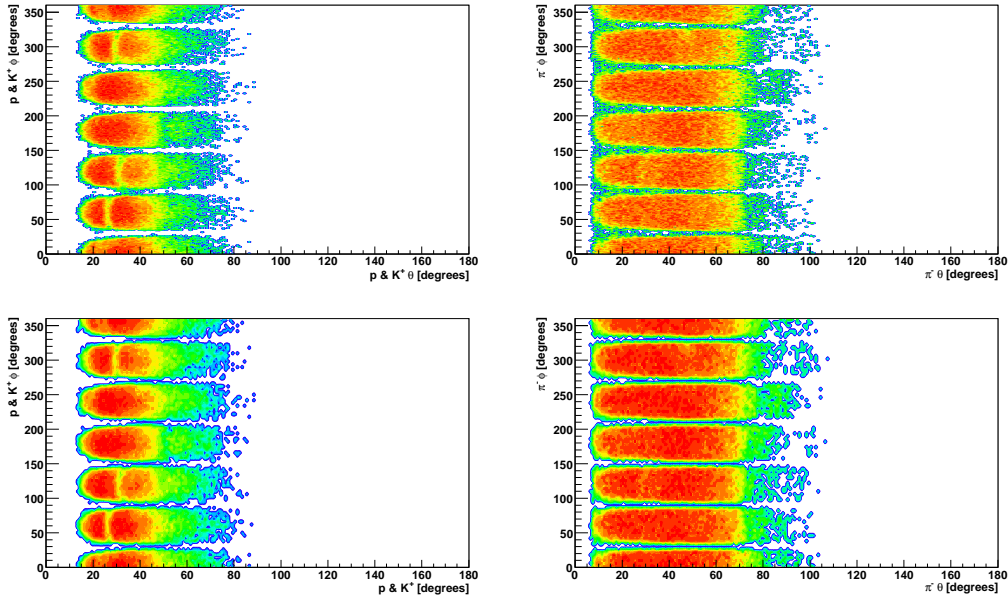


Figure 5.8: θ vs. ϕ for all positive particles (top left) and all negative particles (top right) before fiducial cuts, all sectors shown. θ vs. ϕ for all positive particles (bottom left) and all negative particles (bottom right) after fiducial cuts.

5.2 Analysis of $\gamma d \longrightarrow K^+ p \pi^- (n)$

5.2.1 Λ and Σ Separation

Since the Σ^0 decays into a $\Lambda\gamma$ with a 100% branching ratio, it is necessary to separate a Λ produced from a Σ^0 decay from one which was produced directly. When using a proton target, this can be done using the kaon missing mass. With a bound proton in a deuterium nucleus however, Fermi motion will smear out this distribution and clean separation by this method is no longer possible. It is possible to produce some separation in the hyperons' distributions, a process which will be described in detail shortly, but there always remains some overlap. This overlap will also be accounted for and the process for it described in the following sections.

Figure 5.9 shows that by combining the kaon missing mass, as it would appear in a $\gamma p \longrightarrow K^+ p \pi^-$ reaction (free proton), with the missing mass of a $K^+\Lambda$ produced from a $\gamma d \longrightarrow K^+ p \pi^-$ reaction (bound proton), one can see the Λ and Σ^0 peaks. The projection on the $K^+\Lambda$ -axis (x-axis), shown in the bottom of figure 5.9 show that the background is significant, and has to be accounted for in

the analysis.

By taking this projection onto the x-axis we see the missing mass distribution of our spectator particle. Here, the peak at ~ 0.939 GeV indicates a spectator neutron from reactions that produced a Λ and a K^+ in the final state, whilst the flatter broader peak to the right indicates reactions that produced a K^+ and a Σ^0 in the final state. The broadening in the latter case arises from the fact there is an undetected photon when the Σ^0 decays into a Λ . The peaks are ~ 77 MeV apart however, which corresponds to the mass difference between the two Λ and Σ^0 hyperons. By plotting this projection against photon energy, the separation of the two peaks can be seen more clearly, this is shown in the top plot of figure 5.10. From a combination of these two plots a cut was set at 0.965 GeV/ c^2 was justified to initially separate the hyperons. By performing a Gaussian fit to the spectator neutron peak (bottom of figure 5.9) and taking a -3σ cut one can define a lower limit cut at 0.87 GeV/ c^2 when defining the Λ hyperon. A Gaussian fit to the neutron plus photon peak is unreliable however, so a cut has been placed at 1.1 GeV/ c^2 , where contribution from the Σ^* excited state appears to begin to have an effect. These provide the justification for the vertical lines of the box cuts shown in figure 5.9 used to separate the hyperons.

Having gained a separation of the hyperons according to the spectator particle reconstruction, we can now take a projection onto the y-axis of the top plot in figure 5.9. This axis reconstructs the missing mass of the K^+ as if the reaction were from a free proton and thus should leave us with the hyperon masses. By projecting everything between the first two vertical cuts and the last two we reconstruct missing mass distributions for each hyperon separately. These are shown in the middle and bottom of figure 5.10 for the Λ and Σ^0 respectively, with green lines indicating the PDG masses for each hyperon. By fitting the Σ^0 peak with a Gaussian function one can then take a $\pm 3\sigma$ cut on each side to produce the horizontal cuts that complete the box cut around the Σ^0 hyperon. This procedure can also be applied to the Λ distribution, but a $\pm 3\sigma$ cut proves to be too narrow and a wider cut has been implemented instead. A wider cut is necessary in the case of the Λ hyperon so as to account for the combined widths of each hyperon. Also, this peak is required to be fitted with a function later on in the analysis, a process which will be described in detail shortly. By choosing too narrow a cut and removing too much of the tails at either side of the peak, the fitting algorithm can fail to produce a reliable result. The ratio of $K^+\Lambda$ events to $K^+\Sigma^0$ events was expected to be about 3 : 2 from estimates from the g13 experimental proposal [17] and this was observed to be the case from the data.

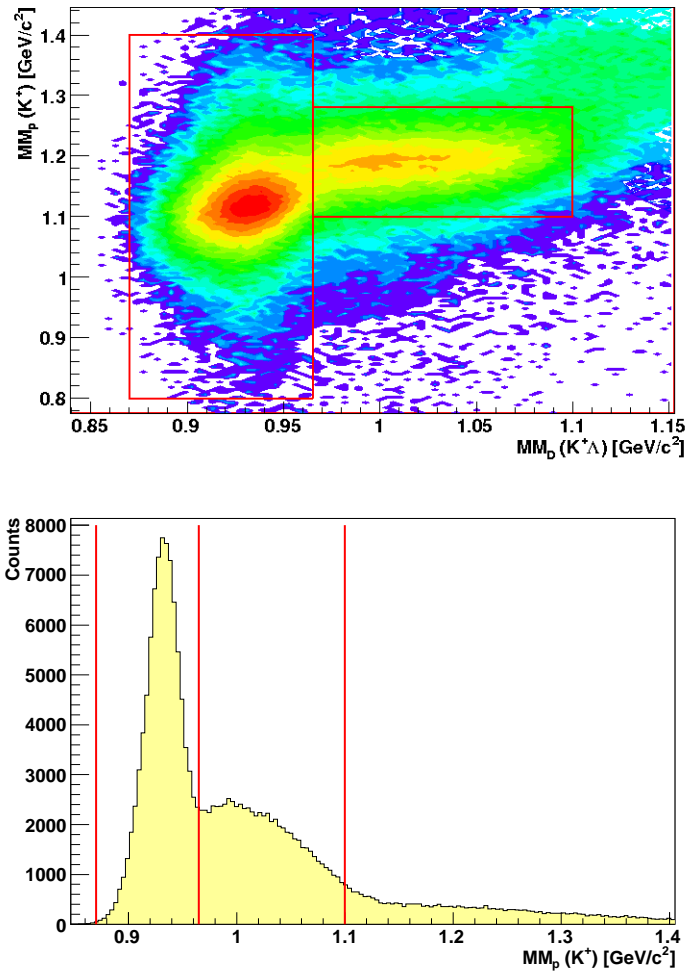


Figure 5.9: (top) Λ and Σ separation missing mass plots. Here the x-axis shows $MM(K^+\Lambda)$ from the deuterium target while the y-axis has $MM(K^+)$ as it would appear from a proton target. The red lines indicate the positions of the cuts for the next four plots. (bottom) $MM_D(K^+\Lambda)$ (x-projection of top plot) with the relevant cuts indicated.

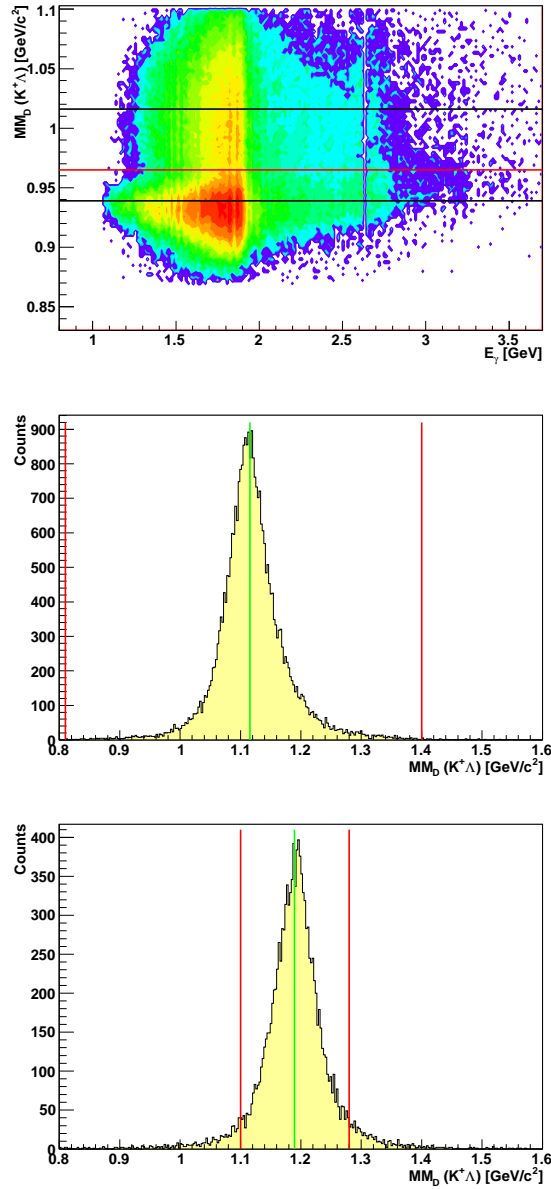


Figure 5.10: (top) $MM_D(K^+\Lambda)$ vs. E_γ with relevant cut indicated by red line and relevant spectator masses indicated by black lines for Σ^0 (top) and Λ (bottom) reactions respectively. (middle) $MM_P(K^+)$ in the range $0.87 < MM_D(K^+\Lambda) < 0.965$, for Λ reactions. Green line indicates PDG mass of Λ and red lines indicate cuts. (bottom) $MM_P(K^+)$ in the range $0.965 < MM_P(K^+) < 1.1$, for Σ^0 reactions. Green line indicates PDG mass of Σ^0 and red lines indicate cuts.

5.2.2 Momentum Cut

The final cut in the analysis was on the momentum of the neutron. The neutron momentum cut is made to keep those neutrons whose momentum is less than 200

MeV/c (and are therefore spectators). Figure 5.11 shows the momentum distribution versus $\cos\theta_n$ and the momentum distribution of the identified neutrons for each hyperon. The lower, green distribution in the right plot of figure 5.11 shows the spectator neutron momentum from Σ^0 hyperons and the taller, black, larger distribution those from Λ hyperons.

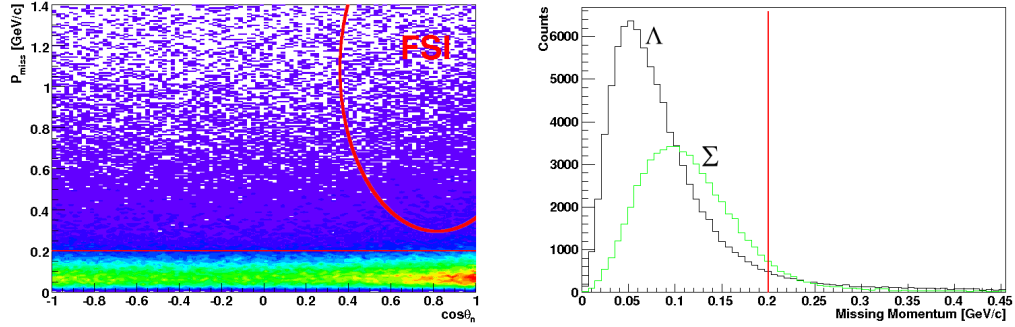


Figure 5.11: Neutron momentum distribution versus \cos of spectator neutron θ angle (left). Events corresponding to those expected to be in the final-state-interaction region are indicated in the red ellipse and the cut at 200 MeV/c is shown. The neutron momentum distribution (right). The red line represents the cut at 200 MeV/c which removes all non spectator (Fermi momentum) neutrons. Black line shows spectator neutron momentum from all $K^+\Lambda$ events and green line shows the spectator neutron momentum from all $K^+\Sigma^0$ events.

5.2.3 Hyperon Yield Extraction

The final stage in the event selection process involved extracting the yield for the reaction channels $\gamma d \rightarrow K^+\Lambda^0$ and $\gamma d \rightarrow K^+\Sigma^0$. These yields were extracted after kaon identification and subsequent rejection of mis-identified charged particles. Having now separated each hyperon (see section 5.2.1), the next step would be to extract from these the beam asymmetry measurements. With a cleanly identified beam asymmetry measurement from the $\gamma d \rightarrow K^+\Sigma^0$ channel we have one reliable result. However, in the case of the $\gamma d \rightarrow K^+\Lambda^0$ channel we have a contribution from the Σ^0 beam asymmetry to account for before we can produce results that we can be confident are due to the Λ channel only. This problem can be best highlighted by looking at the top left distribution in figure 5.10 where the Σ^0 resonance can be clearly seen to protrude significantly under that of the Λ resonance. Conversely, the taller, narrower Λ resonance contributes negligibly to that of the Σ^0 and is thus ignored. To be able to account for this

contamination effect the y-projections of the Λ are fitted with a Voigtian function (a Breit-Wigner convoluted with a Gaussian) in such a way that the overall Voigtian function fits the distribution by summing to smaller Voigtian functions that should describe the individual hyperon resonance contributions. A Voigtian function was used as this best describes the shape of a resonance. Each Voigtian function has four parameters that can be either fixed or allowed to vary within some constraints and these are the resonance width; the Gaussian width; the peak position; and the height scaling factor. The resonance and Gaussian widths were allowed to vary very slightly in the first instance in order to get some optimal values. After this, they were allowed to vary within some tight constraints around the optimum value. This ensured that any detector resolution or smearing effects can be accounted for in the final distributions. Likewise the peak positions were limited within some optimal values allowing us to ensure that the hyperons always remained ~ 77 MeV apart in mass, this being the mass difference between the Λ and the Σ^0 hyperons. The height scaling factor was allowed to vary over a much larger range than the other parameters. By fitting the distributions over each of the final angular bins the numbers of each Λ and Σ^0 contributing to the overall measured Λ asymmetry could be determined. By scaling this measured Λ asymmetry appropriately according to the measured Σ^0 asymmetry and the numbers of each hyperon contributing then a corrected, true value for the Λ asymmetry could be determined. An example of the fitting routine is shown in figure 5.12.

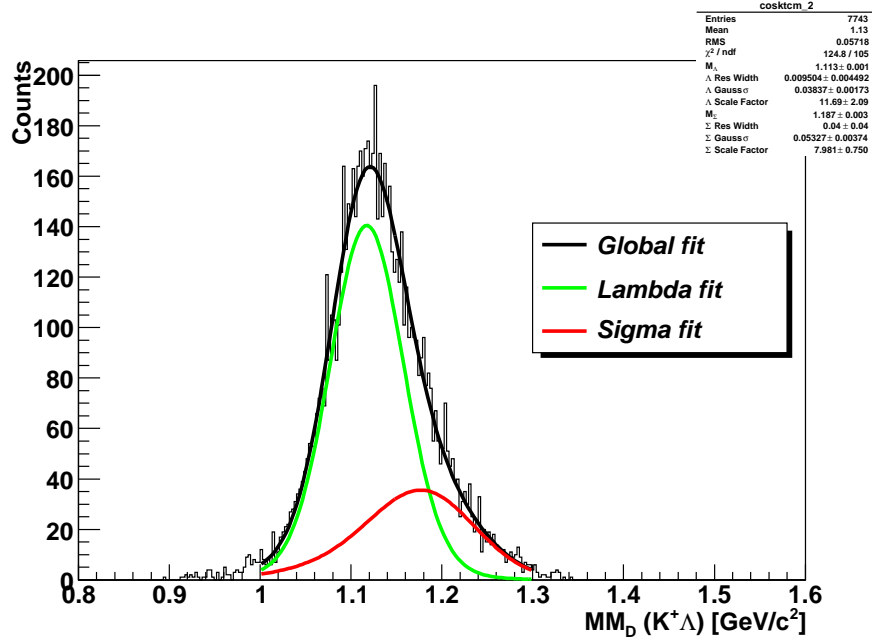


Figure 5.12: Voigtian fitting routine example for one angular bin to extract Λ and Σ^0 yields for Λ beam asymmetry correction.

The fitting routine was the final step to be made in the analysis before the beam asymmetry was extracted from the kaon angular distributions. In order to summarise these steps, table 5.1 shows the cuts applied (in order) to this analysis of the g13 data.

| Applied Cut | Cut Details |
|---------------------------------|--|
| Raw Events Skimmed BOS | 3 charged particles with appropriate associated masses |
| $MM^2(\pi^+ p \pi^-)$ mis-ID | $< 0.98 \text{ MeV}/c^2$ |
| $MM^2(pp\pi^-)$ mis-ID | $< 0.55 \text{ MeV}/c^2$ |
| $MM^2(K^+ p K^-)$ mis-ID | $< 0.55 \text{ MeV}/c^2$ |
| P_K | $> 300 \text{ MeV}/c$ |
| P_p | $> 300 \text{ MeV}/c$ |
| P_π | $> 300 \text{ MeV}/c$ |
| photon-kaon vertex time | $\pm 3\sigma$ |
| photon-proton vertex time | $\pm 3\sigma$ |
| photon-pion vertex time | $\pm 3\sigma$ |
| Invariant mass ($p + \pi^-$) | $\pm 3\sigma$ |
| $\Lambda^0 \Sigma^0$ separation | Box cuts, based on mainly $\pm 3\sigma$ Gaussian fit |
| P_n cut | $< 200 \text{ MeV}/c$ MeV/c , hyperon independent |
| Fiducial cuts | $\pm 5^\circ$ around fiducial regions |

Table 5.1: Analysis cuts.

5.3 Beam Asymmetry

The photon asymmetry results have been extracted for as wide a range of $\theta_{CM}^{K^+}$ and E_γ bins as is possible. The photon beam used during g13 had two orthogonal (PARA and PERP) polarisation settings, which produced almost equal number of statistics. The easiest way to then extract the Σ observable is to construct the asymmetry, A , as a function of ϕ as is described in section 2.2.2. This gave us the following expression:

$$A(\phi) = \frac{\sigma_1(\phi) - \sigma_2(\phi)}{\sigma_1(\phi) + \sigma_2(\phi)} = P_\gamma^{lin} \Sigma \cos 2\phi \quad (5.3)$$

By measuring in this way there is the advantage that the spectrometer's acceptance effect is cancelled out. This negates the requirement to undertake any complicated acceptance calculations when extracting the observables which could potentially introduce large systematic uncertainties. One thing to be noted however, is that the one instance where acceptances would not cancel each other out is if there were any difference in the track reconstruction efficiencies arising from differences in the beam intensities between the two polarisation states. During the course of g13 experimental running we attempted to minimise this effect by alternating the photon polarisation plane at constant intervals throughout.

5.3.1 Bin Selection

The particular bin widths chosen for each kinematic variable used in the measurement of Σ were selected in order to maximise the information extracted as a function of both E_γ and $\theta_{cm}^{K^+}$. Choosing an equal number of bins for each variable would seem to be the most logical choice, but a complication arises when binning in E_γ since there are different discrete energy settings for one coherent peak. Both the degree of photon polarisation and luminosity rapidly decrease when one moves away in energy from the coherent edge. Also, due to the low statistics remaining after all cuts had been made, it was decided best to take as large a bin in energy as was reasonable. By taking these factors into account it was decided to use one E_γ bin, 450 MeV wide per coherent peak setting. This concept of the bin selection is illustrated for the 1.9 GeV coherent spectrum in the top of figure 5.13.

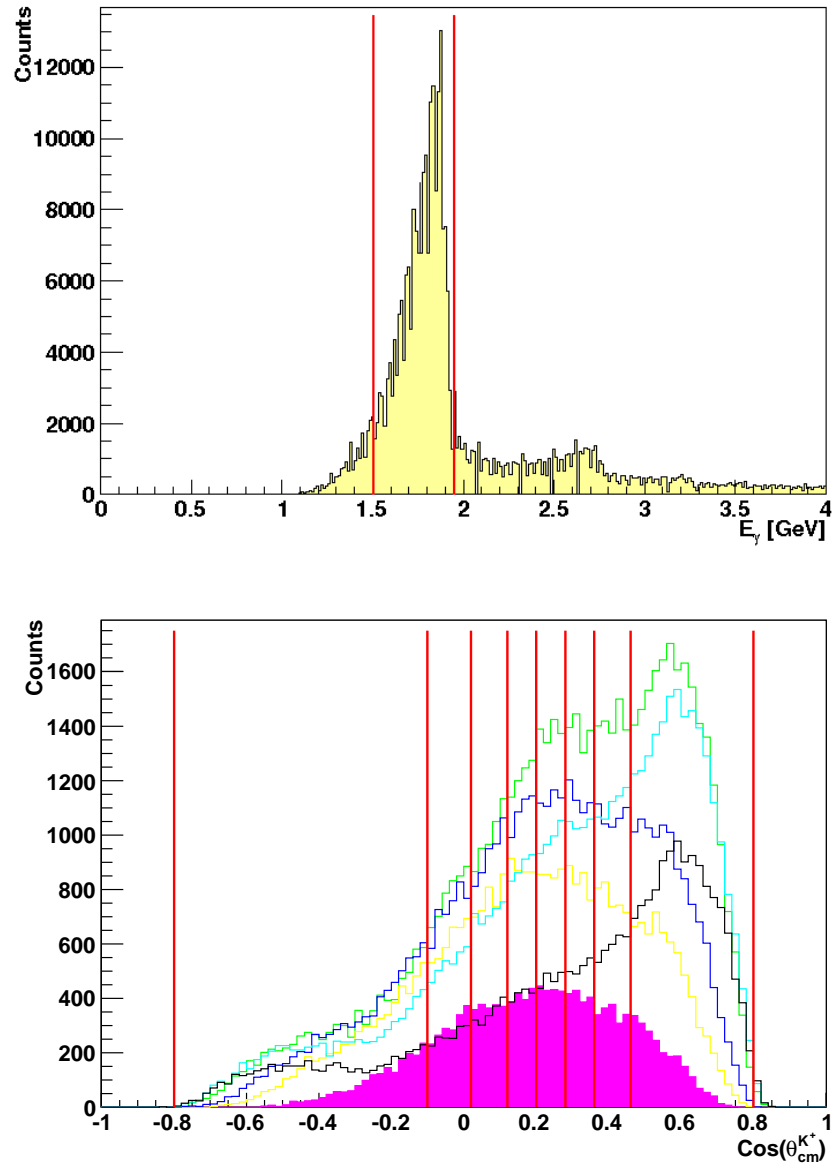


Figure 5.13: The 450 MeV energy bin selection. The distribution for the 1.9 GeV coherent peak setting is shown with the cuts indicated (top). The non-uniform angular bins superimposed on the $\text{cos}(\theta_{cm}^{K^+})$ spectrum (bottom). The majority of the events detected in CLAS are forward angled which results in lower statistics at the backward angles. The eight bins range from $\text{cos}(\theta_{cm}^{K^+}) = -0.8$ to 0.84. Angular distributions are shown for the 1.3 GeV (pink), 1.5 GeV (yellow), 1.7 GeV (blue), 1.9 GeV (green), 2.1 GeV (cyan) and 2.3 GeV (black) settings.

As g13 involved six different coherent peak settings, each separated by 200 MeV, this resulted in six bins in total covering a continuous range in E_γ . To

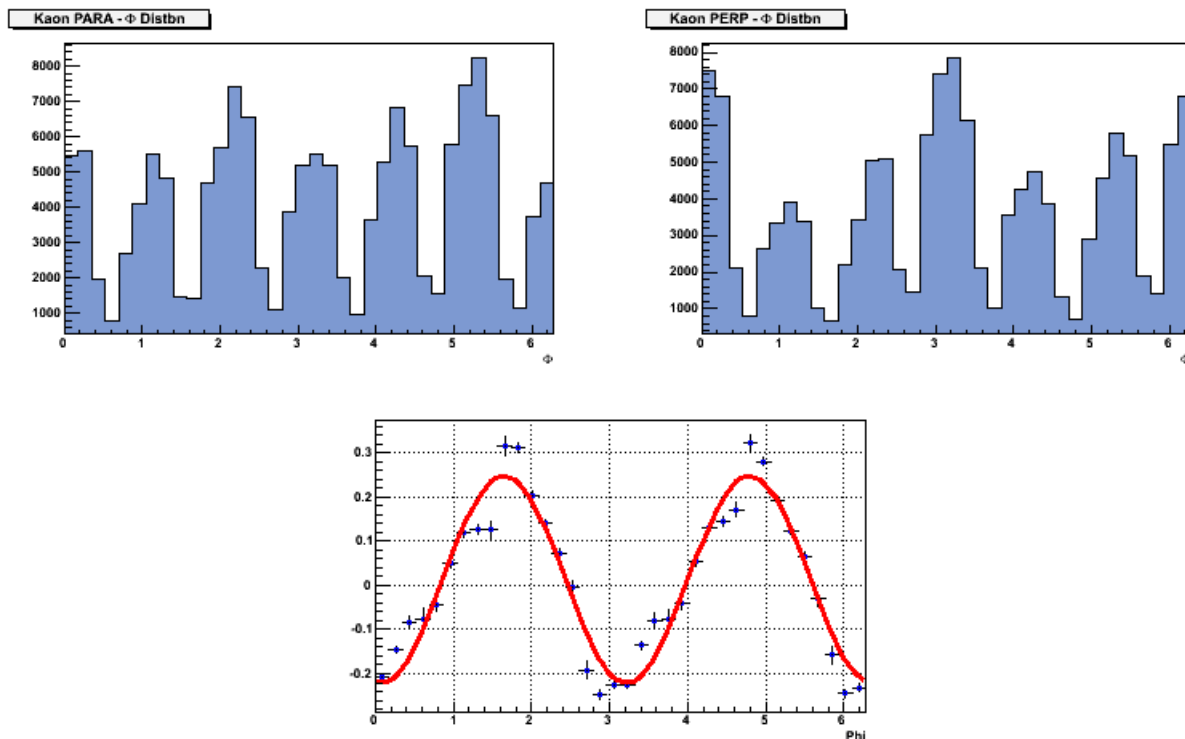


Figure 5.14: ϕ yield of kaons for the parallel polarised photon setting (top left) and the perpendicular setting (top right) integrated over the full angular range. The regions of low acceptance correspond to the locations of the torus magnet coils and are plainly evident in the distributions. The asymmetry of the two polarisation settings is shown in the bottom plot along with a $\cos 2\phi$ fit. This asymmetry technique removes any acceptance issues since the spectrometer acceptance is independent of the photon polarisation state.

complement this, eight bins were chosen for $\cos\theta_{cm}^{K^+}$ as shown in the bottom of figure 5.13, ranging from $\cos\theta_{cm}^{K^+} - 0.8$ to 0.84 . The bin size was selected so that the statistical uncertainty associated with the $\cos\theta_{cm}^{K^+}$ distribution for the coherent edge position with the lowest statistics was minimised. In order to best minimise the statistical uncertainty in the $\cos\theta_{cm}^{K^+}$ binning, non-uniform bins were used so that there should be an equal number of counts in each angular bin for the beam energy setting with the lowest number of statistics (in this case the 1.3 GeV beam setting, highlighted in pink in the right plot of figure 5.13). Altogether there were 48 kinematic bins over which the photon asymmetry was measured.

5.3.2 Extraction of Σ

Now that the asymmetry has been established in a usable form, the beam asymmetry, Σ , can be measured by applying a one dimensional fit of the functional form of equation 5.1 to the asymmetry over ϕ :

$$A(\phi) = \frac{N^{\parallel}(\phi) - N^{\perp}(\phi)}{N^{\parallel}(\phi) + N^{\perp}(\phi)} = P_{\gamma}^{lin} \Sigma \cos 2\phi \quad (5.4)$$

The asymmetry is measured for each kinematic bin in E_{γ} and $\theta_{cm}^{K^+}$. By placing a fit of the form of equation 5.1 over each distribution a photon asymmetry can then be extracted. One complication however, is that the parallel and perpendicular polarised data sets do not generally have the same number of events or mean polarisation. Therefore the two datasets have to be scaled in order to account for these differences in yield and polarisation. This gives rise to the following modified asymmetry relation:

$$A(\phi) = \frac{N^{\parallel}(\phi) - N^{\perp}(\phi)}{N^{\parallel}(\phi) + N^{\perp}(\phi)} = \frac{P^{\parallel} - P^{\perp}}{P^{\parallel} + P^{\perp}} + \frac{2P^{\parallel}P^{\perp}}{P^{\parallel} + P^{\perp}} \Sigma \cos 2\phi \quad (5.5)$$

where P^{\parallel} and P^{\perp} are the mean polarisations of the parallel and perpendicular photon polarisation settings respectively.

With the kinematic bins has been selected, the photon asymmetry, Σ , can now be extracted by fitting the function from equation 5.1 to each of the Φ -distributions on a bin-by-bin basis. In figure 5.14 (top-left and top-right) we can see the Φ -distributions for both the parallel (PARA) and perpendicular (PERP)

data sets respectively, integrated over all $\cos\theta_{cm}^{K^+}$ bins. On the bottom of figure 5.14 there is the photon asymmetry of the two polarised data sets, including error bars. This very effectively demonstrates the power of the asymmetry technique in cancelling any acceptance related effects, resulting in a very clean $\cos 2\Phi$ distribution. Mean polarisations for PARA and PERP settings for each E_γ bin were determined by using the polarisation tables described in section 4.5 and are shown in table 4.2.

The results of fitting to the kaon azimuthal distributions for one E_γ and one $\cos\theta_{cm}^{K^+}$ bin are shown in figures 5.15 and 5.16 for the 1.9 GeV setting. The photon asymmetries resulting from these fits are then plotted as a function of $\cos\theta_{cm}^{K^+}$, shown in figures 5.17 and 5.18 for the $K^+\Lambda$ and $K^+\Sigma^0$ channels respectively. In figure 5.17, we can see both the corrected and the uncorrected values for the asymmetry. The uncorrected values are those which were measured before the dilution of the asymmetry from the Σ^0 channel (described in section 5.2.3) was taken into account, and the corrected values are those once the dilution was accounted for.

5.4 Summary

A detailed analysis algorithm was created to identify the relevant reaction particles and extraction of final yields for $\gamma p(n) \longrightarrow K^+\Lambda(n)$ and $\gamma p(n) \longrightarrow K^+\Sigma^0$. Preliminary cuts based on simple TOF masses were used to skim the dataset down to a manageable size for a full analysis. In the analysis, various cuts were introduced to reduce the background and correctly identify kaons. Once the correct reactions had been identified the hyperon masses were separated using a one-dimensional Voigtian fitting procedure. The final hyperon mass plots demonstrate the success of these procedures with peaks centred on the PDG masses and overall the whole event selection routine performed very well in extracting a final hyperon yield.

By performing a 1-dimensional fit over the kaon azimuthal angle, it was possible to extract a beam asymmetry, Σ . No correction was required to the results

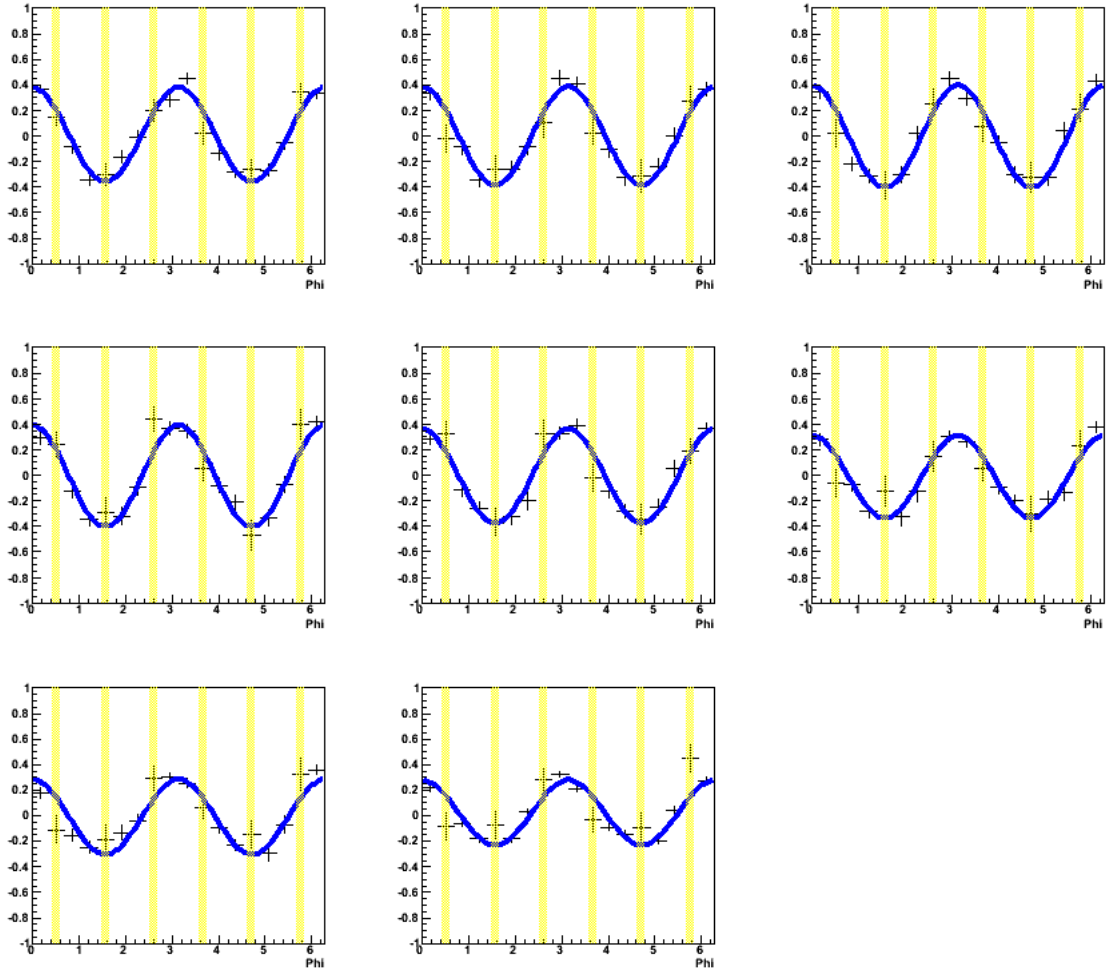


Figure 5.15: $\cos 2\phi$ fits of the asymmetry over the kaon azimuthal angle ϕ for $E_\gamma = 1.9$ GeV for the $K^+\Lambda$ channel. The histograms range from $\cos(\theta_{cm}^{K^+}) = -0.46$ in the top left, to $\cos(\theta_{cm}^{K^+}) = 0.7$ in the bottom middle. The yellow bands indicate the fiducial regions described earlier.

as the method used an asymmetry of of the parallel and perpendicularly polarised data sets from each kinematic bin. The systematic uncertainty from the polarisation is estimated as 5%.

The following chapter discusses the final results of the beam asymmetry measurements and their implications for the quasifree approximation.

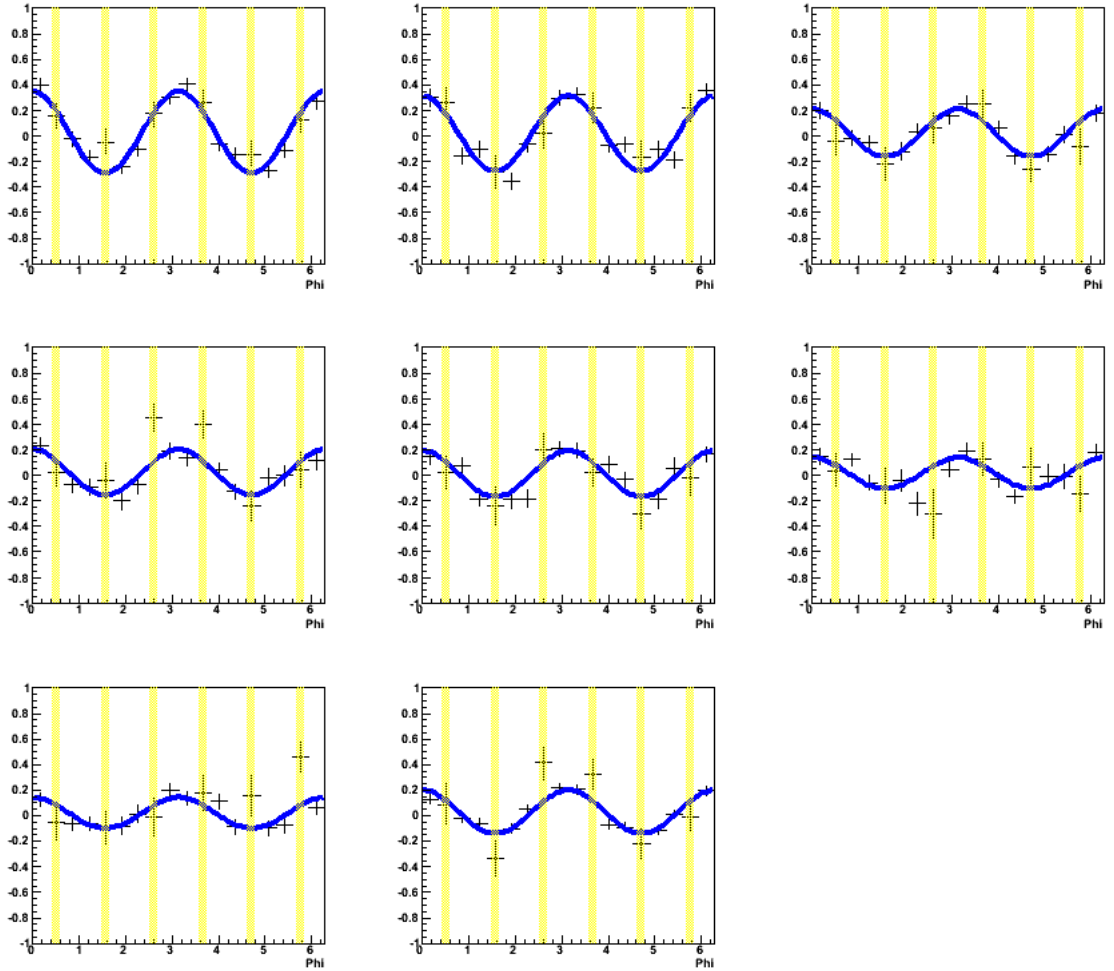


Figure 5.16: $\cos 2\phi$ fits of the asymmetry over the kaon azimuthal angle ϕ for $E_\gamma = 1.9$ GeV for the $K^+\Sigma^0$ channel. The histograms range from $\cos(\theta_{cm}^{K^+}) = -0.46$ in the top left, to $\cos(\theta_{cm}^{K^+}) = 0.7$ in the bottom middle. The yellow bands indicate the fiducial regions described earlier.

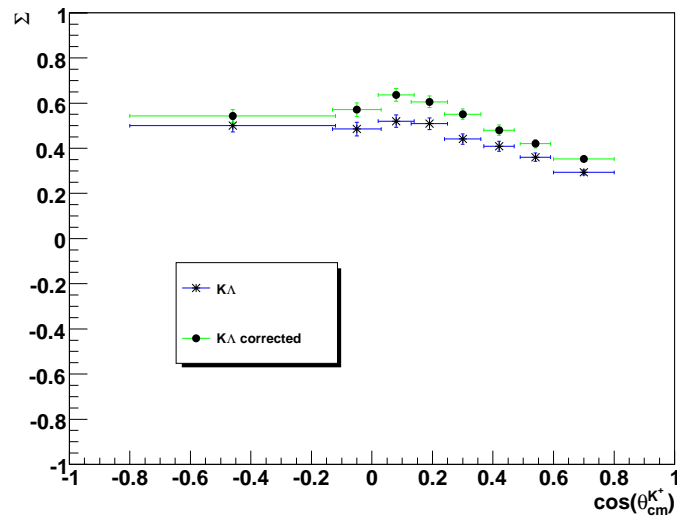


Figure 5.17: Graph of photon asymmetries at $E_\gamma = 1.9$ GeV as a function of $\cos\theta_{cm}^{K^+}$ for the $K^+\Lambda$ channel. All the error bars are statistical and no systematic errors have been included at this stage.

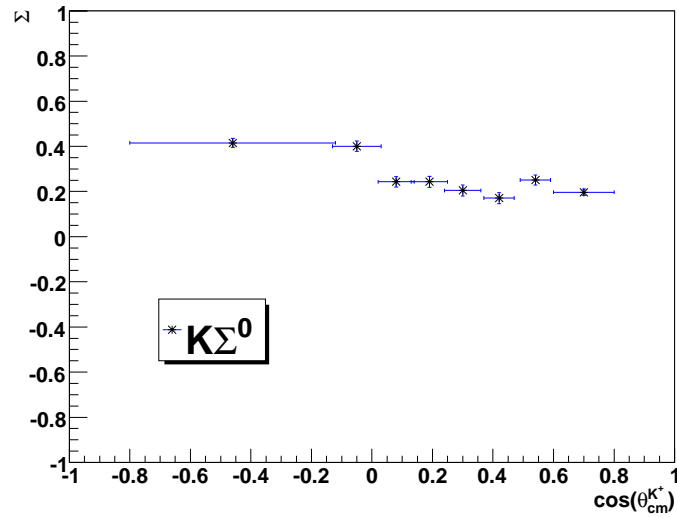


Figure 5.18: Graph of photon asymmetries at $E_\gamma = 1.9$ GeV as a function of $\cos\theta_{cm}^{K^+}$ for the $K^+\Sigma^0$ channel. All the error bars are purely statistical and no systematic errors have been considered at this stage.

Chapter 6

Results and Discussion

Having now described the processes involved in identifying the correct reaction channels and particles (Chapter 5) and to extract and measure the beam asymmetry polarisation observable (Section 5.3) focus is now on presentation and discussion of the final results. The systematic uncertainties and choice of binning that are associated with these measurements were discussed in the previous two chapters, however it should be pointed out that only error bars associated with the statistical uncertainties are shown in the plots. The beam asymmetry has an associated systematic uncertainty of $\sim 5\%$, as was discussed previously (section 4.5).

This chapter presents the final beam asymmetry measurements and they are compared to work done previously on the free proton. Kaon-MAID model calculations for the neutron are also shown to demonstrate the possibilities for the future.

6.1 Comparison with free proton

The results have been binned identically to those on the free proton for the g8b, CLAS experiment [7]. Figures 6.1 and 6.2 show $K\Lambda$ as a function of $\cos\theta_{cm}^{K^+}$ and E_γ , respectively. Also shown are the Kaon-MAID calculations for the free proton. Figures 6.3 and 6.4 show the same comparison for $K\Sigma^0$. In all cases, the vertical error bars are statistical, whilst horizontally they indicate the bin width, with the data point located at the centroid of the bin. The previous work on the free proton from the g8b experiment only reached photon energies of 2.1 GeV and the Kaon-MAID prescription only goes as far as this as well, whereas the current work reached photon energies of 2.3 GeV. An important point to be noted at this stage is that the model calculations are all for the free proton, as no reliable

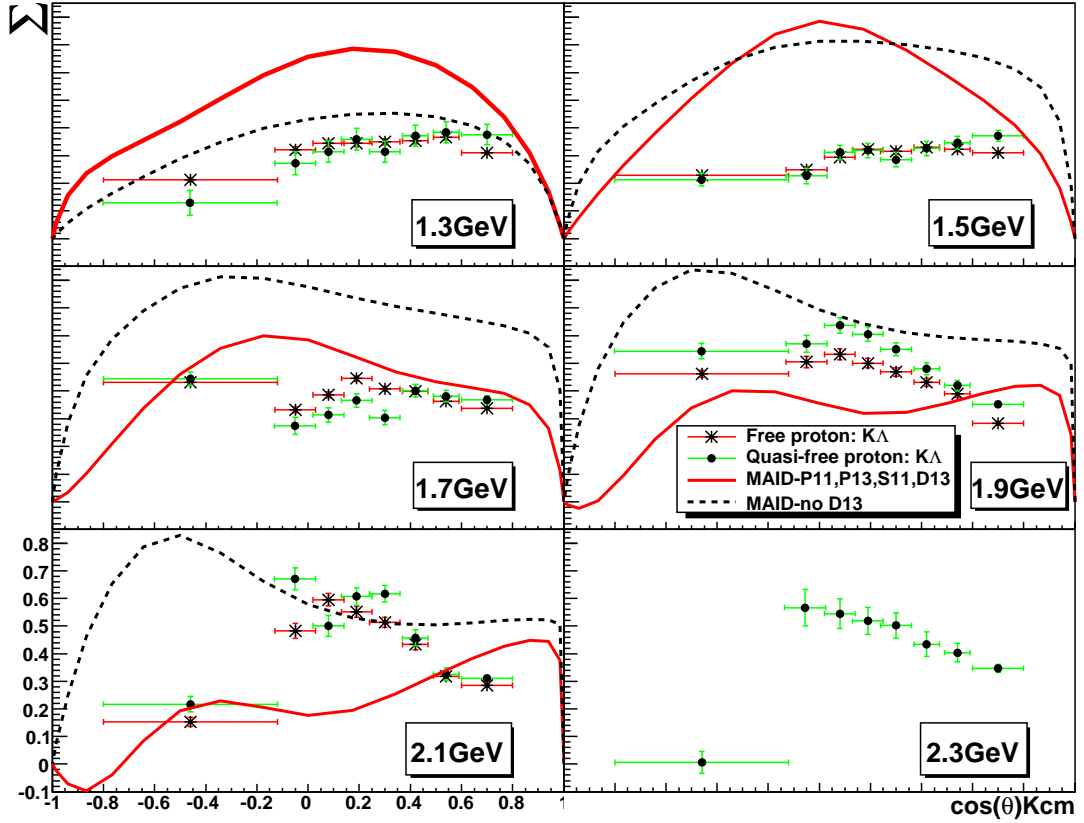


Figure 6.1: Beam asymmetries from the free (stars with red error bars) and quasifree (circles with green error bars) proton for the $K\Lambda$ channel as a function of $\cos\theta_{cm}^{K^+}$ ranging from $E_\gamma = 1.25$ GeV (top left) to 2.25 GeV (bottom right). Data are compared with model curves from the Kaon-MAID model: core resonances (dashed black line) and D_{13} included (solid red line).

model results yet exist for strangeness photoproduction on the deuteron. Given the similarity of comparisons between results from the free and the quasi-free proton already highlighted in section 2.4.2, it is not expected that when reliable model calculations become available for the process on the deuteron that they be vastly different. At photon energies near the maximum and minimum values and some backwards angles, the associated statistical error bars are larger due to there being fewer events in these kinematic ranges.

Only statistical errors are indicated on the plots. In both cases (g8b and g13) the main systematic error is in the photon polarisation (and may vary systematically by up to 5% as a function of E_γ). The results of the free and the quasifree are consistent over all energies and $\cos\theta$. Therefore, a spectator missing momentum cut that rejects those with $P_{missing} > 200$ MeV selects only quasifree events. This information is crucial for data from the neutron channels, which are also being analysed from the g13 dataset.

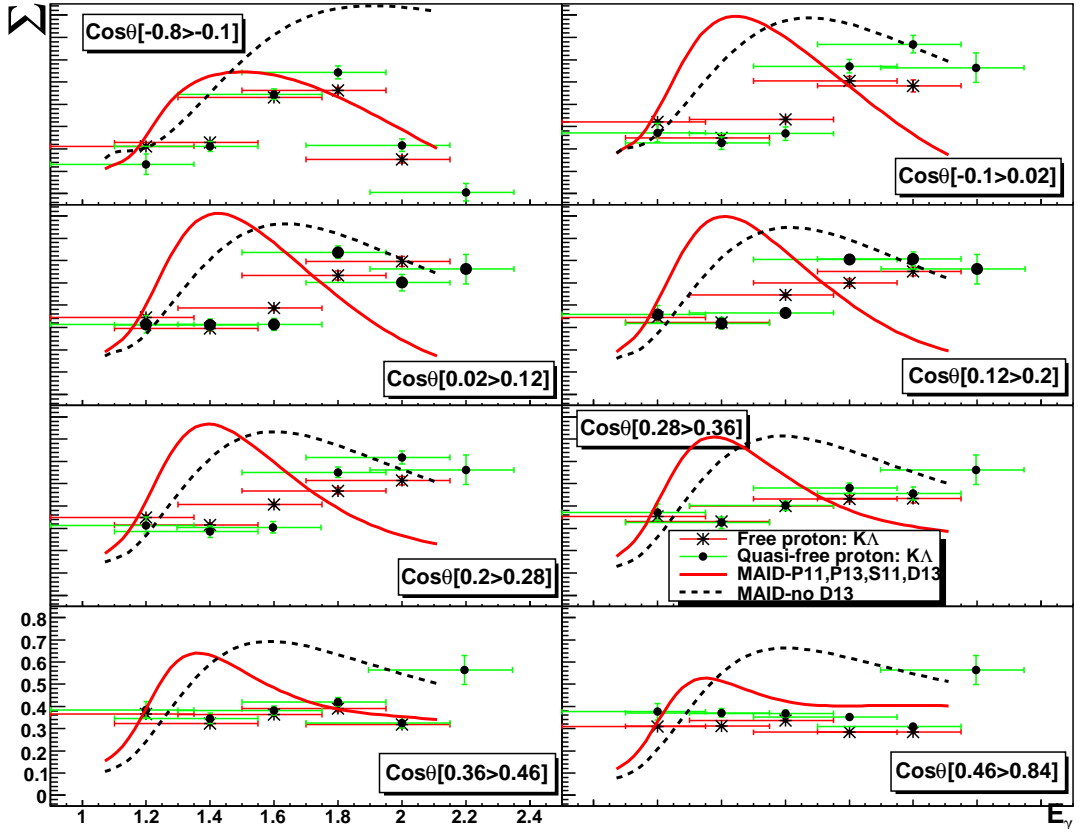


Figure 6.2: Beam asymmetries from the free (stars with red error bars) and quasifree (circles with green error bars) proton for the $K\Lambda$ channel as a function of E_γ ranging from $\cos \theta_{cm}^{K^+} = -0.46$ (top left) to 0.7 (bottom middle). Data are compared with model curves from the Kaon-MAID model: core resonances (dashed black line) and D_{13} included (solid red line).

| | 1300 | 1500 | 1700 | 1900 | 2100 |
|--|----------------|-----------|-----------------|----------|-----------|
| $-0.8 < \cos \theta_{cm}^{K^+} < -0.1$ | -0.084405 | -0.016835 | 0.013492 | 0.080469 | 0.063979 |
| $-0.1 < \cos \theta_{cm}^{K^+} < 0.02$ | -0.047842 | -0.023045 | -0.063305 | 0.065865 | 0.185783 |
| $0.02 < \cos \theta_{cm}^{K^+} < 0.12$ | -0.029733 | 0.017254 | -0.073443 | 0.103753 | -0.094384 |
| $0.12 < \cos \theta_{cm}^{K^+} < 0.2$ | 0.014059 | -0.003317 | -0.079196 | 0.104867 | 0.0558 |
| $0.2 < \cos \theta_{cm}^{K^+} < 0.28$ | -0.035873 | -0.029182 | -0.103179 | 0.082394 | 0.104131 |
| $0.28 < \cos \theta_{cm}^{K^+} < 0.36$ | 0.018246 | 0.003797 | 0.002262 | 0.04799 | 0.023826 |
| $0.36 < \cos \theta_{cm}^{K^+} < 0.46$ | <i>0.18725</i> | 0.024076 | 0.017942 | 0.029592 | 0.007506 |
| $0.46 < \cos \theta_{cm}^{K^+} < 0.84$ | 0.06609 | 0.060717 | 0.031326 | 0.068594 | 0.024522 |

Table 6.1: This table shows the beam asymmetry difference, $\Delta\Sigma$, between the quasifree and free proton ($\Delta\Sigma = \Sigma_{QFP} - \Sigma_{FP}$) measurements for the $K\Lambda$ channel. Differences for each energy bin in MeV versus $\cos \theta_{cm}^{K^+}$ can be found by reading values vertically from the table and those for each angular bin versus energy by reading horizontally. The highest and lowest differences are highlighted in red italics and bold green respectively.

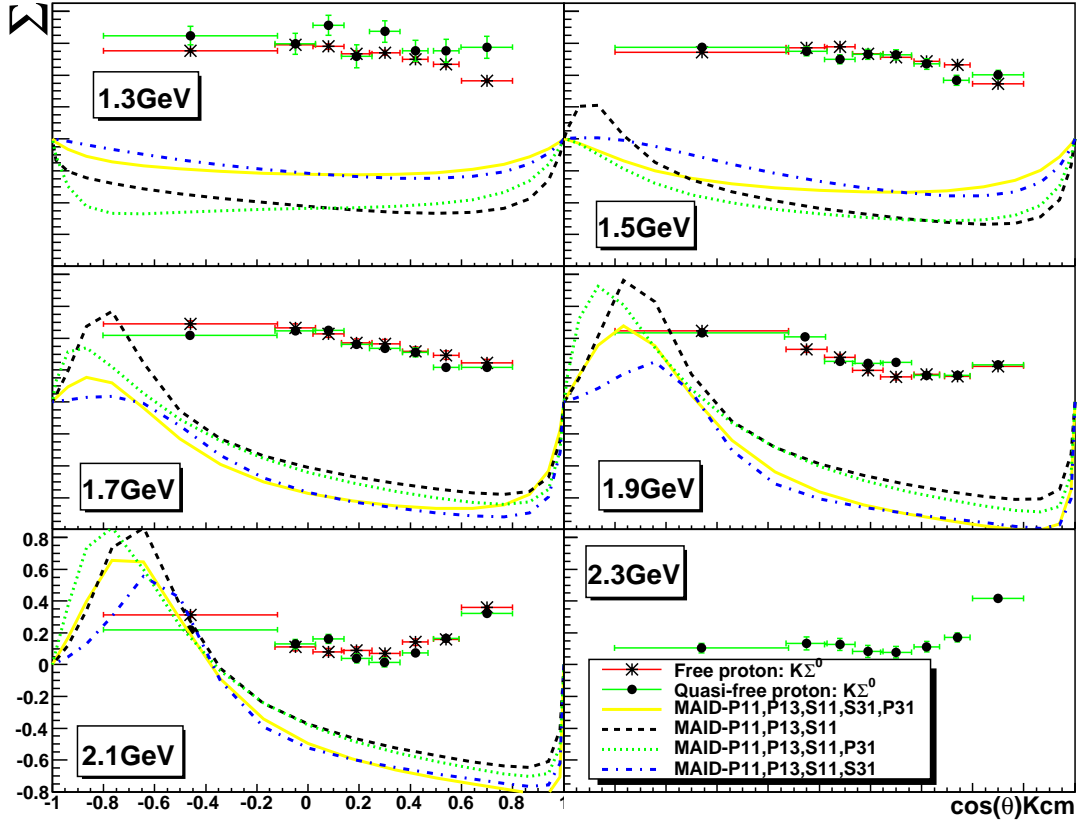


Figure 6.3: Beam asymmetries from the free (stars with red error bars) and quasifree (circles with green error bars) proton for the $K\Sigma^0$ channel as a function of $\cos \theta_{cm}^{K^+}$ ranging from $E_\gamma = 1.25$ GeV (top left) to 2.25 GeV (bottom right). Data are compared with model curves from the Kaon-MAID model: core resonances (dashed black line), S_{31} included (dot-dashed blue line), P_{31} included (dotted green line) and both S_{31} and P_{31} included (solid yellow line).

| | 1300 | 1500 | 1700 | 1900 | 2100 |
|--|-----------------|-----------|-----------|-----------|-----------------|
| $-0.8 < \cos \theta_{cm}^{K^+} < -0.1$ | 0.093994 | 0.028959 | -0.07526 | -0.01172 | -0.093941 |
| $-0.1 < \cos \theta_{cm}^{K^+} < 0.02$ | 0.006466 | -0.023013 | -0.020973 | 0.071204 | 0.018979 |
| $0.02 < \cos \theta_{cm}^{K^+} < 0.12$ | 0.133621 | -0.080731 | 0.020372 | -0.027148 | 0.0801492 |
| $0.12 < \cos \theta_{cm}^{K^+} < 0.2$ | -0.016283 | -0.003881 | -0.008476 | 0.04296 | -0.0493765 |
| $0.2 < \cos \theta_{cm}^{K^+} < 0.28$ | 0.134032 | 0.012705 | -0.03098 | 0.091119 | -0.06332389 |
| $0.28 < \cos \theta_{cm}^{K^+} < 0.36$ | 0.052168 | -0.01788 | -0.006291 | -0.00605 | -0.067534 |
| $0.36 < \cos \theta_{cm}^{K^+} < 0.46$ | 0.084714 | -0.102126 | -0.077185 | 0.004338 | 0.003684 |
| $0.46 < \cos \theta_{cm}^{K^+} < 0.84$ | <i>0.202827</i> | 0.057177 | -0.027702 | 0.007884 | -0.03821 |

Table 6.2: This table shows the beam asymmetry difference, $\Delta\Sigma$, between the quasifree and free proton ($\Delta\Sigma = \Sigma_{QFP} - \Sigma_{FP}$) measurements for the $K\Sigma$ channel. Differences for each energy bin in MeV versus $\cos \theta_{cm}^{K^+}$ can be found by reading values vertically from the table and those for each angular bin versus energy by reading horizontally. The highest and lowest differences are highlighted in red italics and bold green respectively.

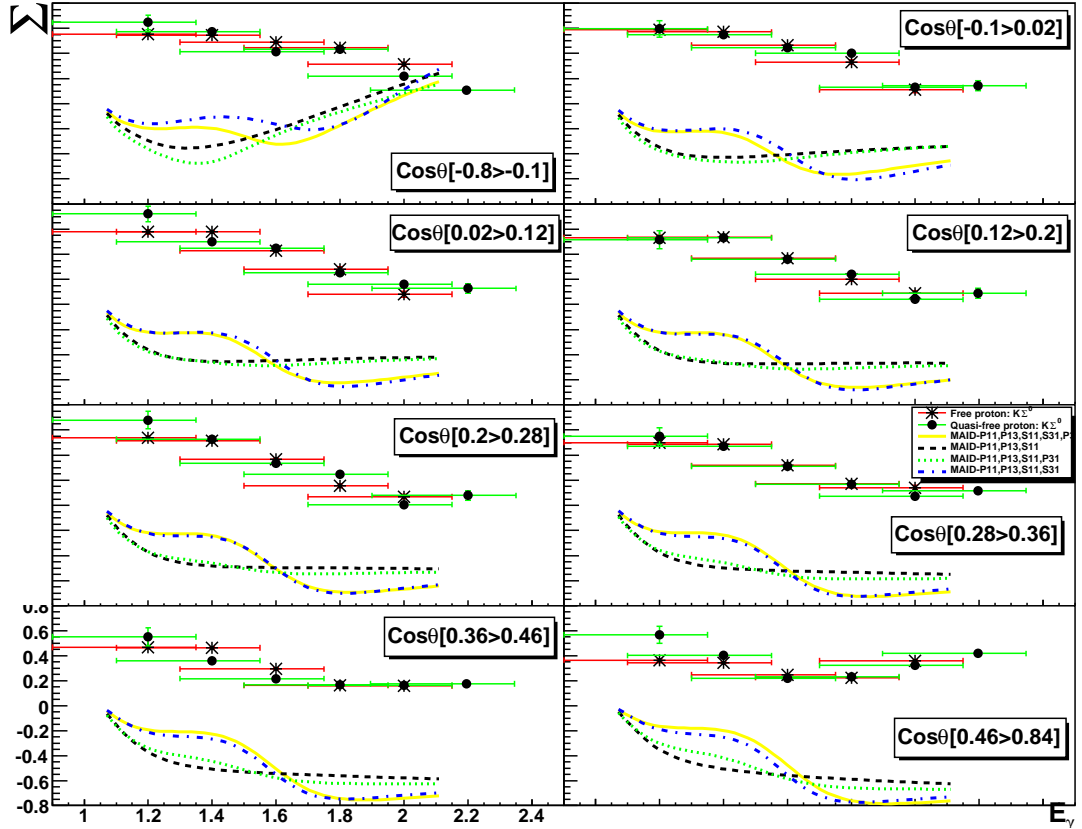


Figure 6.4: Beam asymmetries from the free (stars with red error bars) and quasifree (circles with green error bars) proton for the $K\Sigma^0$ channel as a function of E_γ ranging from $\cos\theta_{cm}^{K^+} = -0.46$ (top left) to 0.7 (bottom middle). Data are compared with model curves from the Kaon-MAID model: core resonances (dashed black line), S_{31} included (dot-dashed blue line), P_{31} included (dotted green line) and both S_{31} and P_{31} included (solid yellow line).

6.1.1 Photon asymmetry results for $K^+\Lambda$

A comparison of free proton beam asymmetry measurements to the Kaon-MAID theory curve calculations are shown in figures 6.1 and 6.2. This model utilises an isobar approach that includes the $S_{11}(1650)$, $P_{11}(1710)$ and the $P_{13}(1720)$ core resonances and can incorporate the disputed $D_{13}(1900)$ resonance as well. In the lowest (1.3 GeV) energy photon bin we find the best agreement with the MAID model calculations. By including a $D_{13}(1900)$ resonance the asymmetry calculations are shifted to higher values so the results of this analysis would seem to favour the exclusion of this resonance. In the plots shown, a solid red line depicts the Kaon-MAID calculations including a $D_{13}(1900)$ resonant state whilst the dashed black line does not include this resonance. In the 1.5 GeV energy bin both calculations yield values that are higher than the measurements made for the asymmetry in the free proton analysis. The following energy bin of 1.7 GeV looks to favour the inclusion of a $D_{13}(1900)$ resonance, and at higher energies the inclusion of this resonance is lent credence in the forward angle results. In the MAID model however, the inclusion of a $D_{13}(1900)$ resonant state is not on it's own, enough to accurately describe the apparent structures observed in the backward and mid angular ranges.

In the work by Lee, Mart, Bennhold and others highlighted previously [16] (see section 2.16), they concluded that there was a narrow kinematic window where the FSI did not affect selected polarisation observables, including the beam asymmetry. This region they stated to be close to quasifree kinematics with moderate missing momentum ($p_m < 150$ MeV/c) and photon energies below $E_\gamma < 1.4$ GeV. In the current analysis selecting $p_m < 200$ MeV/c was found to be appropriate and the beam asymmetry was found to agree between the free and quasifree cases across the entire photon energy range.

The size and direction of the difference between the beam asymmetry measurements varies in each bin. There are exceptions found however, in the 1900 MeV bin and the three most forward (highest $\cos\theta_{cm}^{K^+}$) angular bins, where the quasifree measurements consistently predict larger beam asymmetries than those from the free measurements. Possible explanations for this may be some as yet undetermined systematic effect in either of the two analyses or perhaps it is an indication of some FSI the Λ hyperon undergoes at this energy. A systematic effect would perhaps have been expected to be reproduced in other energy bins and in the $K\Sigma$ results and any evidence of FSI also in the $K\Sigma$ results however, and this does not appear to be the case. The largest deviation (+0.18725) occurs in the seventh angular bin of the 1300 MeV setting, though this is perhaps to be

expected as the statistics were much poorer (~ 3500) in these kinematical regions of low energy and extreme angle. The smallest deviation ($+0.002262$) is found in sixth angular bin of the 1700 MeV setting, again not unexpected as this kinematic region had the second highest statistics (~ 8500 counts) in this particular bin, superceded only by the 1900 MeV setting (~ 10000 counts).

Overall, the agreement between the free [7] and the quasifree proton beam asymmetry measurements was found to be very good for the $K^+\Lambda$ channel across the full kinematic range. The best agreement was found at mid-to-forward angles in most coherent peak settings. At the lowest and highest ranges of E_γ there was some small differences observed at backward angles, but at these extreme energy and angular bins the associated statistics were much poorer ($\sim 50\%$ less) than those in the mid energy and angular bins.

6.1.2 Photon asymmetry results for $K^+\Sigma^0$

The results from the free proton analysis for the $K^+\Sigma^0$ channel were also compared to the Kaon-MAID model calculations, shown in figures 6.3 and 6.4, where an isobar description based on the inclusion of the $S_{11}(1650)$, $P_{11}(1710)$, $P_{13}(1720)$, $S_{31}(1900)$ and $P_{31}(1910)$ states is used. On the whole, the models do not give a good reproduction of the results from this analysis as the model calculations are mainly negative, only turning positive at some backwards angle regions of the higher energy bins. The MAID calculations for the first two energy bins are entirely negative and so do not accurately represent the measurements from the free proton analysis. At higher energies the model reproduces the general shape of the data but generally with the opposite sign. In reproducing the general shape however, it is managing to describe the backwards peak that can be seen in the results. It failed to account for the apparent peak seen in the measurements at forward angles though.

Like the results for the $K\Lambda$ channel, the differences in the asymmetry measurements for the $K\Sigma$ channel vary both in size and sign, though this time there is no consistent over or under estimation of the free proton results. This time the largest deviation ($+0.202827$) appears in the most forward (eighth) angular bin in the 1300 MeV beam setting, which, like the $K\Lambda$ results, is a kinematical region of much less statistics (~ 1600), with the added reduction in statistics for the $K\Sigma$ channel. The smallest difference (0.003684) occurs in the 2100 MeV setting in the seventh angular bin, again like the $K\Lambda$ results this being the bin with the second highest statistics (~ 6500) in this setting.

Again the results from previous analysis made on the free proton [7] agreed

generally very well with those from the quasifree analysis across the full kinematic range. Similarly, the best agreement was at mid-to-forward angles in most coherent peak settings, while, again, at the lowest and highest ranges of E_γ there were some small differences at backwards angles. Like the results for the $K^+\Lambda$ channel these kinematic regions had much poorer ($\sim 44\%$ less) statistics than those of the mid-range angle and energy bins, but now also less overall events associated with the $K^+\Sigma^0$ channel since the ratio of $K^+\Lambda$ events to $K^+\Sigma^0$ events was expected to be about 3 : 2 from estimates from the g13 experimental proposal [17], as was mentioned in section 5.2.1.

6.2 Predictions for the neutron channel

It is not the focus of this work but figure 6.5 gives an illustration of the sensitivity we could expect for the Σ^0 channel on the neutron. This figure shows Kaon-MAID calculations for the free neutron channel with the statistical errors from $\gamma p(n) \rightarrow K^+\Sigma^0(n)$ results of this analysis shown along the zero lines. Again, only the statistical errors are indicated. The current results also include here a $\pm 5\%$ systematic error, however it is anticipated that future work will reduce this to $\sim 3\%$. In the case of the $K^+\Sigma^0$ channel, some of the predictions for the lower energy bins on the neutron are positive, unlike the proton again where the same energy bins predicted only negative beam asymmetry values. For the higher energy regions however, they neutron predictions look very similar to those from the proton, both in size and shape.

6.3 Conclusions

Given the small differences shown in this analysis between $K^+\Lambda$ and $K^+\Sigma^0$ photoproduction between the quasifree proton in deuterium and the case of the free proton, alongside the results previously highlighted in section 2.4.2 for η photoproduction, it bears out the predictions that there is no difference in the beam asymmetry results of the strangeness production process from the free proton when compared to the quasifree case in the deuteron. Also that by selecting those spectator particles with a missing momentum of less than 200 MeV/c we are selecting only quasifree events. Thus we conclude that re-scattering effects in the final state interaction of particles produced from a quasifree case are negligible and produce no measurable effect on the polarisation of the outgoing hyperon.

With this information it would now be acceptable to perform similar exper-

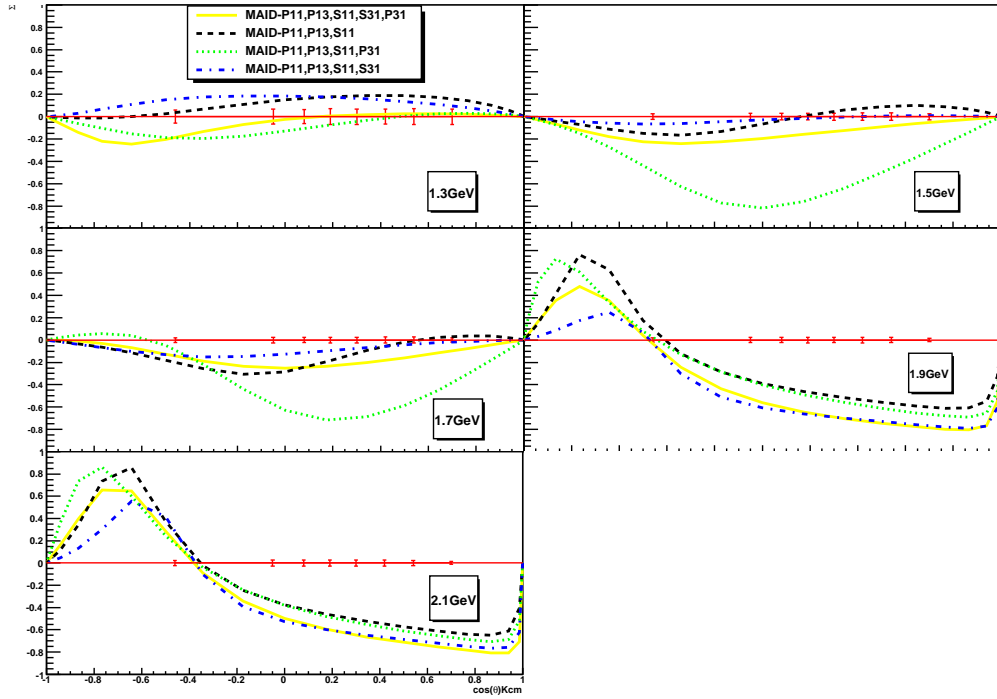


Figure 6.5: Beam asymmetry predictions from the free neutron for the reaction $\gamma n \rightarrow K^0 \Sigma^0$ as a function of $\cos \theta_{cm}^{K^+}$ ranging from $E_\gamma = 1.25$ GeV (top left) to 2.05 GeV (bottom middle). Model curves from the Kaon-MAID model: core resonances (dashed black line), S_{31} included (dot-dashed blue line), P_{31} included (dotted green line) and both S_{31} and P_{31} included (solid yellow line). Statistical error bars from comparable ($K \Sigma^0$) results are shown along the red zero line.

iments as have been done on the proton to investigate the excitation spectrum, on the bound neutron in a deuterium nucleus. Given that the quasifree approximation is valid in the case of the proton, it is reasonable to expect that this case extends to the neutron also and such experiments would therefore yield comparable results to what would be expected from a free neutron. Work has already begun in this direction, with Kaon-MAID model predictions for the “free” neutron and other analyses already underway from the g13 experiment to investigate these predictions in the quasifree case of the bound neutron in deuterium. Together with the ongoing analyses of beam asymmetry measurements from the bound neutron in deuterium, they offer a look ahead to what can be investigated and tested in the near future of the field and indicate another step forward to a complete understanding of the structure of the nucleon.

Bibliography

- [1] WM Yao et al. Review of particle physics. *Journal of Physics G: Nuclear and Particle Physics*, 33:1–1232, 2006.
- [2] S. Capstick and W. Roberts. Strange decays of nonstrange baryons. *Physical Review D*, 58(7):74011, 1998.
- [3] D. Faiman and A.W. Hendry. Harmonic-oscillator model for baryons. *Physical Review*, 173(5):1720–1729, 1968.
- [4] CP Forsyth and RE Cutkosky. A quark model of baryons with natural flavor. *Zeitschrift für Physik C Particles and Fields*, 18(3):219–227, 1983.
- [5] John W.C. McNabb. Photoproduction of hyperons off protons in the Nucleon Resonance using CLAS at Jlab. PhD thesis, Carnegie Mellon University, 2002.
- [6] JWC McNabb, RA Schumacher, L. Todor, G. Adams, E. Anciant, M. Anghinolfi, B. Asavapibhop, G. Audit, T. Auger, H. Avakian, et al. Hyperon photoproduction in the nucleon resonance region. *Physical Review C*, 69(4):42201, 2004.
- [7] C. A. Paterson. Polarization Observables in Strangeness Photoproduction with CLAS at Jefferson Lab. PhD thesis, University of Glasgow, 2008.
- [8] M. Gell-Mann and Y. Ne'eman. The eightfold way. Benjamin New York, 1964.
- [9] R. Koniuk and N. Isgur. Baryon decays in a quark model with chromodynamics. *Physical Review D*, 21(7):1868–1886, 1980.
- [10] DB Lichtenberg and PJ Keleman. Quark-Diquark Model of Baryons and SU (6). *Physical Review*, 167(5):1535–1542, 1968.

- [11] T. Mart and C. Bennhold. Evidence for a missing nucleon resonance in kaon photoproduction. *Physical Review C*, 61(1):012201, 1999.
- [12] F.J. Klein *et al.* Search for missing nucleon resonances in the photoproduction of hyperons using a polarized photon beam and a polarized target.
- [13] F. Klein P. Cole. Photoproduction of omega mesons off protons with linearly polarized photons. *Class approved analysis: E-99-013*, 1994.
- [14] J.M. Laget. Rescattering in Meson Photoproduction off Few Body Systems. *Arxiv preprint nucl-th/0507035*, 2005.
- [15] RB Wiringa, VGJ Stoks, and R Schiavilla. Accurate nucleon-nucleon potential with charge-independence breaking. *Physical Review C*, 51:38–51, 1995.
- [16] FX Lee, T. Mart, C. Bennhold, H. Haberzettl, and LE Wright. Nuclear Theory Title: Quasifree Kaon Photoproduction on Nuclei. *Journal reference: Nucl. Phys. A695*, 237:272, 2001.
- [17] Y. Ilieva A. Tkabladze D. Ireland *et al* P. Nadel-Turonski, B. L. Berman. g13 proposal, kaon production on the deuteron using polarized photons. *PR-06-103*, 2006.
- [18] RA Adelseck and B. Saghai. Kaon photoproduction: Data consistency, coupling constants, and polarization observables. *Physical Review C*, 42(1):108–127, 1990.
- [19] GF Chew, FE Low, and Y. Nambu. Relativistic dispersion relation approach to photomeson production. *Physical Review*, 106(6):1345–1355, 1957.
- [20] CG Fasano and, F. Tabakin, and B. Saghai. Spin observables at threshold for meson photoproduction. *Physical Review C*, 46(6):2430–2455, 1992.
- [21] IS Barker, A. Donnachie, and JK Storrow. Complete experiments in pseudoscalar photoproduction. *Nuclear Physics B*, 95(2), 1975.
- [22] T. Mart, C. Bennhold, and CE Hyde-Wright. Constraints on coupling constants through charged Σ photoproduction. *Physical Review C*, 51(3):1074–1077, 1995.
- [23] RA Adelseck, C. Bennhold, and LE Wright. Kaon photoproduction operator for use in nuclear physics. *Physical Review C*, 32(5):1681–1692, 1985.

- [24] R.A. Williams, C.R. Ji, and S.R. Cotanch. Hyperon electroproduction in a crossing and duality constrained model. *Physical Review C*, 46(5):1617–1635, 1992.
- [25] H. Thom. Phenomenological Analysis of $K \Lambda$ Photoproduction. *Phys Rev*, 151:1322, 1966.
- [26] T. Feuster and U. Mosel. Unitary model for meson-nucleon scattering. *Physical Review C*, 58(1):457–488, 1998.
- [27] H. Haberzettl. Gauge-invariant theory of pion photoproduction with dressed hadrons. *Physical Review C*, 56(4):2041–2058, 1997.
- [28] M.Q. Tran et al. Measurement of $\gamma p \rightarrow K^+ \Lambda$ and $\gamma p \rightarrow K^+ \Sigma^0$ at photon energies up to 2 GeV. *Phys. Lett. B*, 445:20, 1998.
- [29] B. Saghai. From known to undiscovered resonances. *Arxiv preprint nucl-th/0105001*, 2001.
- [30] Aachen-Berlin-Bonn-Hamburg-Heidelberg-Munich collaboration. Multipion and Strange-Particle Photoproduction on Protons at Energies up to 5.8 GeV. *Phys. Rev.*, 188:2060, 1969.
- [31] N. Kaiser, T. Waas, and W. Weise. SU (3) chiral dynamics with coupled channels: Eta and kaon photoproduction. *Arxiv preprint hep-ph/9607459*, 1996.
- [32] T. Sato and T.S.H. Lee. Meson-exchange model for πN scattering and $\gamma N \rightarrow \pi N$ reaction. *Physical Review C*, 54(5):2660–2684, 1996.
- [33] V. Shklyar, H. Lenske, and U. Mosel. Coupled-channel analysis of $K\Lambda$ production in the nucleon resonance region. *Phys. Rev. C*, 72(1):015210, 2005.
- [34] J. Caro Ramon, N. Kaiser, S. Wetzel, and W. Weise. Chiral SU (3) dynamics with coupled channels: inclusion of p-wave multipoles. *Nuclear Physics, Section A*, 672(1-4):249–269, 2000.
- [35] W.T. Chiang, F. Tabakin, T.S.H. Lee, and B. Saghai. Nuclear Theory Title: Coupled-channel study of $\gamma p \rightarrow K^+ \Lambda$. *Phys. Lett. B* 517, 101:108, 2001.
- [36] A.V. Sarantsev, V.A. Nikonov, A.V. Anisovich, E. Klempt, and U. Thoma. Decays of baryon resonances into $K^+ \Lambda$, $K^+ \Sigma$ and $K^0 \Sigma^+$. *The European Physical Journal A-Hadrons and Nuclei*, 25(3):441–453, 2005.

- [37] A. Usov and O. Scholten. $K\Lambda$ and $K\Sigma$ photoproduction in a coupled-channels framework. *Physical Review C*, 72(2):25205, 2005.
- [38] B. Juliá-Díaz, B. Saghai, T.S.H. Lee, and F. Tabakin. Dynamical coupled-channels approach to hadronic and electromagnetic kaon-hyperon production on the proton. *Physical Review C*, 73(5):55204, 2006.
- [39] R. Bradford, RA Schumacher, JWC McNabb, L. Todor, et al. Differential cross sections for $\gamma p \rightarrow K^+ Y$ for Λ and Σ^0 hyperons. *Phys. Rev. C*, 73:035202, 2006.
- [40] K.-H. Glander *et al.* Measurement of $\gamma p \rightarrow K^+ \Lambda$ and $\gamma p \rightarrow K^+ \Sigma^0$ at photon energies up to 2.6 GeV. *Eur. Phys. J A* 19, 251, 2004.
- [41] RGT Zegers, M. Sumihama, et al. Beam-Polarization Asymmetries for the $p(\gamma, K^+) \Lambda$ and $p(\gamma, K^+) \Sigma^0$ Reactions for $E_\gamma=1.5-2.4$ GeV. *Phys. Rev. Lett*, 91:092001, 2003.
- [42] T. Corthals, J. Ryckebusch, and T.V. Cauteren. Forward-angle $K^+ \Lambda$ photoproduction in a Regge-plus-resonance approach. *Physical Review C*, 73(4):45207, 2006.
- [43] T. Corthals, T.V. Cauteren, J. Ryckebusch, and D.G. Ireland. Regge-plus-resonance treatment of the $p(\gamma, K^+) \Sigma^0$ and $p(\gamma, K^0) \Sigma^+$ reactions at forward kaon angles. *Physical Review C*, 75(4):45204, 2007.
- [44] T. Corthals. Regge Plus Resonance Approach to Kaon Production from the Proton. PhD thesis, Universiteit Gent, 2007.
- [45] A. Lleres, O. Bartalini, V. Bellini, JP Bocquet, P. Calvat, M. Capogni, L. Casano, M. Castoldi, A. D'Angelo, J.P. Didelez, et al. Polarization observable measurements for $\gamma p \rightarrow K^+ \Lambda$ and $\gamma p \rightarrow K^+ \Sigma^0$ for energies up to 1.5 GeV. *The European Physical Journal A*, 31(1):79–93, 2007.
- [46] J. Ajaka, M. Anghinolfi, V. Bellini, G. Berrier, JP Bocquet, M. Breuer, PM Calvat, M. Capogni, LE Casano, M. Castoldi, et al. New measurement of Σ beam asymmetry for η meson photoproduction on the proton. *Physical Review Letters*, 81(9):1797–1800, 1998.
- [47] O. Bartalini, V. Bellini, J.P. Bocquet, P. Calvat, M. Capogni, L. Casano, M. Castoldi, A. D'Angelo, J.P. Didelez, R. Di Salvo, et al. Measurement of η photoproduction on the proton from threshold to 1500 MeV. *The European Physical Journal A-Hadrons and Nuclei*, 33(2):169–184, 2007.

- [48] V. Kuznetsov, O. Bartalini, V. Bellini, M. Castoldi, A. D'Angelo, JP Didelez, R. Di Salvo, A. Fantini, D. Franco, G. Gervino, et al. η photoproduction off the neutron at GRAAL: Evidence for a resonant structure at $W = 1.67$ GeV. *eprint arXiv: hep-ex/0409032*, 2004.
- [49] H. Kohri et al. Differential Cross Section and Photon-Beam Asymmetry for the $\gamma n \rightarrow K^+ \Sigma$ - Reaction at $E_\gamma = 1.5$ -2.4 GeV. *Phys. Rev. Lett*, 97:082003, 2006.
- [50] Joseph James Melone. Measurement of the photon asymmetry for the reaction $\gamma p \rightarrow K^+ \Lambda^0$ at CLAS from 1.6 to 2.0 GeV. PhD thesis.
- [51] Christopher I.O. Gordon. Rho photoproduction using linearly polarized photons with the CLAS detector. PhD thesis, Glasgow University, 2004.
- [52] J.D. Kellie *et al.* Photoproduction of vector mesons and hyperons with a beam of linearly-polarized photons. *g8 update*, 2001.
- [53] R.A. Arndt, R.L. Workman, Z. Li, and L.D. Roper. Partial-wave analysis of pion photoproduction. *Physical Review C*, 42(5):1853–1863, 1990.
- [54] W.T. Chiang and F. Tabakin. Completeness rules for spin observables in pseudoscalar meson photoproduction. *Physical Review C*, 55(4):2054–2066, 1997.
- [55] INFN-LNF P. Levi Sandri. <http://nuclear.gla.ac.uk/kl/eurotag/presentations/workshop2008/workshoppresentations/graal.pdf>. Recent results from GrAAL and future developments.
- [56] C. Bennhold et al. Quasifree kaon photoproduction on nuclei. *Nucl. Phys. A*, 639:209c, 1998.
- [57] H. Haberzettl. Gauge-invariant theory of pion photoproduction with dressed hadrons. *Phys. Rev. C*, 56:2041–2058, 1997.
- [58] H. Haberzettl, C. Bennhold, T. Mart, and T. Feuster. Gauge-invariant tree-level photoproduction amplitudes with form factors. *Phys. Rev. C*, 58:R40–R44, 1998.
- [59] H. Haberzettl. Preserving the gauge invariance of meson production currents in the presence of explicit final-state interactions. *nucl-th/0003058*, 2000.

- [60] S. S. Kamalov, J. A. Oller, E. Oset, and M. J. Vicente-Vacas. Meson exchange currents in kaon scattering on the lightest nuclei. *Phys. Rev. C*, nucl-th/9907119:2985, 1997.
- [61] E. D. Cooper, B. K. Jennings, and J. Mares. Hyperon-nucleus scattering in dirac phenomenology. *Nucl. Phys. A*, 580([http://dx.doi.org/10.1016/0375-9474\(94\)00559-6](http://dx.doi.org/10.1016/0375-9474(94)00559-6)):419–428, 1994.
- [62] E. D. Cooper, B. K. Jennings, and J. Mares. Hyperon-nucleus interaction at intermediate energies. *Nucl. Phys. A*, 585([http://dx.doi.org/10.1016/0375-9474\(94\)90906-7](http://dx.doi.org/10.1016/0375-9474(94)90906-7)):157–163, 1995.
- [63] J. Mares, B. K. Jennings, and E. D. Cooper. Dirac phenomenology and hyperon-nucleus interactions. *Prog. Theor. Phys. (Suppl.)*, 117(<http://ptp.ipap.jp/link?PTPS/117/415>):415–433, 1995.
- [64] L. J. Abu-Raddad and J. Piekarewicz. Quasifree kaon photoproduction from nuclei in a relativistic approach. *Phys. Rev. C*, 61(10.1103/PhysRevC.61.014604):014604, 1999.
- [65] R. K. Bradford et al. First measurement of beam-recoil observables C_x and C_z in hyperon photoproduction. *Physical Review C (Nuclear Physics)*, 75(3):035205, 2007.
- [66] J.P Connelly. g8 proposal, photoproduction of the rho meson from the proton with linearly polarized photons. 1994.
- [67] Christoph W. Leeman *et al.* The Continuous Electron Beam Accelerator Facility: CEBAF at the Jefferson Laboratory. Technical report, Jefferson Laboratory, 2001.
- [68] U. Timm. Coherent bremsstrahlung of electrons in crystals. *Fortschritte der Physik*, 17(12), 1969.
- [69] JD Kellie, PJM Clive, GL Yang, R. Beck, BC Evans, C. Gordon, C. Hall, JW Harris, RT Jones, D. Laundry, et al. The selection and performance of diamond radiators used in coherent bremsstrahlung experiments. *Nuclear Inst. and Methods in Physics Research, A*, 545(1-2):164–180, 2005.
- [70] F. Rambo, J. Ahrens, H.J. Arends, R. Beck, G. Galler, JD Kellie, H.P. Krahn, A. Kraus, U. Ludwig, J. Peise, et al. Enhancement of the linear polarization of coherent bremsstrahlung by collimation of the photon beam. *Physical Review C*, 58(1):489–501, 1998.

- [71] The science of quark confinement and gluonic excitations, gluex/hall d design report, version 5. Technical report, Jefferson Laboratory, 2002.
- [72] W.J Briscoe *et al.* NSF Major Research Instrumentation, NSF Award 9724489. Technical report.
- [73] DI Sober, H. Crannell, A. Longhi, SK Matthews, JT O'Brien, BL Berman, WJ Briscoe, P.L. Cole, JP Connelly, WR Dodge, et al. The bremsstrahlung tagged photon beam in Hall B at JLab. *Nuclear Inst. and Methods in Physics Research, A*, 440(2):263–284, 2000.
- [74] BA Mecking, G. Adams, S. Ahmad, E. Anciant, M. Anghinolfi, B. Asavapibhop, G. Asryan, G. Audit, T. Auger, H. Avakian, et al. The CEBAF large acceptance spectrometer (CLAS). *Nuclear Inst. and Methods in Physics Research, A*, 503(3):513–553, 2003.
- [75] M. Amarian, G. Asryan, K. Beard, W. Brooks, V. Burkert, T. Carstens, A. Coleman, R. Demirchyan, Y. Efremenko, H. Egiyan, et al. The CLAS forward electromagnetic calorimeter. *Nuclear Inst. and Methods in Physics Research, A*, 460(2-3):239–265, 2001.
- [76] G. Adams, V. Burkert, R. Carl, T. Carstens, V. Frolov, L. Houghtlin, G. Jacobs, M. Kossov, M. Klusman, B. Kross, et al. The CLAS cherenkov detector. *Nuclear Inst. and Methods in Physics Research, A*, 465(2-3):414–427, 2001.
- [77] MD Mestayer, DS Carman, B. Asavapibhop, FJ Barbosa, P. Bonneau, SB Christo, GE Dodge, T. Dooling, WS Duncan, SA Dytman, et al. The CLAS drift chamber system. *Nuclear Inst. and Methods in Physics Research, A*, 449(1-2):81–111, 2000.
- [78] M. Anghinolfi, M. Battaglieri, P. Corvisiero, R. De Vita, E. Golovach, A. Longhi, V. Mokeev, G. Ricco, M. Ripani, V. Sapunenko, et al. Response to cosmic rays of the large-angle electromagnetic shower calorimeter of the CLAS detector. *Nuclear Inst. and Methods in Physics Research, A*, 447(3):424–431, 2000.
- [79] T. P. Smith *et al.* CLAS-NOTE 1995-003. Technical report, 1995.
- [80] D. Lawrence *et al.* Clas drift chamber calibration: Software and procedures. *CLAS-NOTE 99-018*, 1999.

- [81] ES Smith, T. Carstens, J. Distelbrink, M. Eckhause, H. Egiyan, L. Elouadrhiri, J. Ficenec, M. Guidal, AD Hancock, FW Hersman, et al. The time-of-flight system for CLAS. *Nuclear Instruments and Methods in Physics Research A*, 432:265–298, 1999.
- [82] M. Guillo *et al.* Ec time calibration procedure for photon runs in clas. *CLAS-NOTE 01-014*, 2001.
- [83] D. C. Doughty *et al.* A VXIbus based trigger for the CLAS detector at CEBAF. *Nucl. Sci. IEEE Transactions*, 39: 241, 1992.
- [84] Jefferson lab online data acquisition. Technical report, <http://coda.jlab.org>.
- [85] V. Blobel. The BOS system, Dynamic memory management, Universität Hamburg. 1994.
- [86] D. Cords *et al.* Clas event format with bos. *CLAS-NOTE 94-012*, 1994.
- [87] J. Manak *et al.* Data processing procedures. *CLAS-NOTE 99-016*, 1999.
- [88] M. Ito. Mysql database for the monitoring of pass0/1 cooking of photon data. CLAS-NOTE 2004-003.
- [89] G. Gavalian. C interface to mysql for monitoring and storing clas data analyses results. CLAS-NOTE 2002-011.
- [90] E. Anciant *et al.* Clas-note 1999-004. Technical report, 1999.
- [91] A. Natter. <http://www.pit.physik.uni.tuebingen.de/grabmayr/software/bremsanalytic.html>.
- [92] E. Pasyuk. Clas-note 2007-016. Technical report, 2007. Technical Report.

“Utram bibis? Aquam an undam?”

John Fowles, *The Magus*.

“Si tacuisses, philosophus mansisses.”

Boethius', *The Consolation of Philosophy*.